

Tectonics

Supporting Information for

**Differential exhumation of the Eastern Cordillera in the Central Andes:
Evidence for south-verging backthrusting (Abancay Deflection, Peru)**

Benjamin Gérard^{1*}, Xavier Robert¹, Laurence Audin¹, Pierre G. Valla^{1,2}, Matthias Bernet¹,
Cécile Gautheron³

¹ *Univ. Grenoble Alpes, IRD, ISTERRE, CNRS, 38000 Grenoble, France*

² *Institut of Geological Sciences, University of Bern, Baltzerstrasse 3, 3012 Bern, Switzerland*

³ *Université Paris-Saclay, CNRS, GEOPS, 91405, Orsay, France*

** Now at GET, Université de Toulouse, CNRS, IRD, UPS, (Toulouse), France.*

Contents of this file

- Text S1: Present-day geothermal gradient computation for the Abancay Deflection
- Text S2: Neighborhood Algorithm (NA) inversions with Pecube
- Text S3: Limitation for fault geometry at the surface with Pecube
- Text S4: Topography / relief inversed with Pecube – non convergent parameters
- Text S5: Pecube outcomes imposing a warmer geothermal gradient (30°C/km)
- Figure S1: AFT single-grain data (a) and radial plots (b) for sample AB-17-05
- Figure S2: AFT single-grain data (a) and radial plots (b) for sample AB-17-06
- Figure S3: AFT single-grain data (a) and radial plots (b) for sample AB-17-07
- Figure S4: AFT single-grain data (a) and radial plots (b) for sample AB-17-08
- Figure S5: AFT single-grain data (a) and radial plots (b) for sample AB-17-11
- Figure S6: AFT single-grain data (a) and radial plots (b) for sample AB-17-13
- Figure S7: AFT single-grain data (a) and radial plots (b) for sample AB-17-15
- Figure S8: AFT single-grain data (a) and radial plots (b) for sample AB-17-18
- Figure S9: AFT single-grain data (a) and radial plots (b) for sample AB-17-19
- Figure S10: AFT single-grain data (a) and radial plots (b) for sample AB-17-22
- Figure S11: AFT single-grain data (a) and radial plots (b) for sample AB-17-23
- Figure S12: AFT single-grain data (a) and radial plots (b) for sample AB-17-25
- Figure S13: AFT single-grain data (a) and radial plots (b) for sample AB-17-26
- Figure S14: AFT single-grain data (a) and radial plots (b) for sample AB-17-29
- Figure S15: AFT single-grain data (a) and radial plots (b) for sample AB-17-31
- Figure S16: AFT single-grain data (a) and radial plots (b) for sample AB-17-32
- Figure S17: AFT single-grain data (a) and radial plots (b) for sample AB-17-33
- Figure S18: AFT single-grain data (a) and radial plots (b) for sample AB-17-36
- Figure S19: AFT single-grain data (a) and radial plots (b) for sample AB-17-37
- Figure S20: AFT single-grain data (a) and radial plots (b) for sample AB-17-38

- Figure S21: AFT single-grain data (a) and radial plots (b) for sample AB-17-39
- Figure S22: AFT single-grain data (a) and radial plots (b) for sample AB-17-40
- Figure S23: AFT single-grain data (a) and radial plots (b) for sample AB-17-41
- Figure S24: AFT single-grain data (a) and radial plots (b) for sample AB-17-42
- Figure S25: AFT single-grain data (a) and radial plots (b) for sample AB-17-44
- Figure S26: AFT single-grain data (a) and radial plots (b) for sample AB-17-51
- Figure S27: AFT single-grain data (a) and radial plots (b) for sample AB-17-55
- Figure S28: QTQt inversion results for the Ocobamba high-altitudinal profile
- Figure S29: QTQt inversion results for the AB-17-13 sample
- Figure S30: QTQt inversion results for the AB-17-15 sample
- Figure S31: QTQt inversion results for the AB-17-18 sample
- Figure S32: QTQt inversion results for the AB-17-19 sample
- Figure S33: QTQt inversion results for the Lucma high-altitudinal profile
- Figure S34: QTQt inversion results for the Limatambo high-altitudinal profile
- Figure S35: QTQt inversion results for the Abancay high-altitudinal profile
- Figure S36: QTQt inversion results for the Incahuasi high-altitudinal profile
- Figure S37: Observed vs. predicted thermochronological ages (AFT & AHe) modeled with QTQt
- Figure S38: Parameters implemented and/or explored in Pecube through time
- Figure S39: Pecube inversion results for landscape evolution parameters through time for the Altiplano block
- Figure S40: Pecube inversion results for landscape evolution parameters through time for the Eastern Cordillera block
- Figure S41: Observed data vs. predicted ones from Pecube for the Altiplano crustal block
- Figure S42: Observed data vs. predicted ones from Pecube for the Eastern Cordillera crustal block
- Figure S43: Exhumation rates derived from AER, QTQt and Pecube
- Figure S44: Sample locations within the Abancay Deflection
- Figure S45: 3D Pecube inversion results for the Altiplano crustal block imposing a geothermal gradient of 30°C/km
- Figure S46: 3D Pecube inversion results for the Eastern Cordillera crustal block imposing a geothermal gradient of 30°C/km
- Table S1: QTQt parameters for thermochronological data modeling
- Table S2: Apatite (U-Th-Sm)/He data – Computed values for Pecube modeling
- Table S3. Thermal and rheological parameters for Pecube modeling
- Table S4: Explored parameters and ranges for thermochronological data inversion (Pecube modeling)

Additional Supporting Information (Files uploaded separately)

- Movie S1: Tectono-morphic evolution of the southern Abancay Deflection (Altiplano block) since 50 Ma (Topography, relief)
- Movie S2: Tectono-morphic evolution of the southern Abancay Deflection (Altiplano block) since 50 Ma (Exhumation rates)
- Movie S3: Tectono-morphic evolution of the southern Abancay Deflection (Altiplano block) since 50 Ma (AHe surface ages)
- Movie S4: Tectono-morphic evolution of the southern Abancay Deflection (Altiplano block) since 50 Ma (AFT surface ages)

- Movie S5: Tectono-morphic evolution of the northern Abancay Deflection (Eastern Cordillera block) since 50 Ma (Exhumation rates)
- Movie S6: Tectono-morphic evolution of the northern Abancay Deflection (Eastern Cordillera block) since 50 Ma (Topography, relief)
- Movie S7: Tectono-morphic evolution of the northern Abancay Deflection (Eastern Cordillera block) since 50 Ma (AHe surface ages)
- Movie S8: Tectono-morphic evolution of the northern Abancay Deflection (Eastern Cordillera block) since 50 Ma (AFT surface ages)

Introduction

This document includes extra-information regarding thermochronological ages (AHe & AFT) computation and details about the 2D and 3D modeling (2D time-temperature modeling outputs (QTQt; Gallagher, 2012) and 3D thermo-kinematic modeling results (Pecube; Braun, 2003; Braun et al., 2012)). We collected 33 samples into crystalline bedrock through five high-altitudinal profiles (Ocobamba, Lucma, Incahuasi, Abancay and Limatambo) and 4 individual samples over the Abancay Deflection (Figure S44). The field trip took place between April and June 2016. The AHe (Table S2) and AFT (Figures S1-S27) analyses were performed respectively at GEOPS laboratory (Université Paris Saclay, France) and ISTERRE laboratory (University Grenoble Alpes, France). Computed age uncertainties are available in the data tables (main article text). Additionally, we provide 8 videos (Movies S1-S8) presenting the tectono-morphic evolution (topography, exhumation rates and surface thermochronological ages evolution) of the southern and northern Abancay Deflection according to the best-fitting Pecube modeling outcomes (discussion in the main article text). For each modeled crustal blocks, we provide graphics exhibiting observed data vs. predicted ones for validation of Pecube 3D modeling (Figures S41-S42). Modeling outcomes are all compared to age-elevation relationships and QTQt modeling (Table S1 and Figures S28-S37) to derive the exhumation histories of studied areas (Figure S43).

Text S1. Present-day geothermal gradient computation for the Abancay Deflection

Using the simplified heat equation from Braun et al. (2006), we estimated the geothermal gradient for the Abancay Deflection.

List of parameters:

T_{surface} : Temperature at the surface (K; °C)

T_{bottom} : Temperature at the base of the crust (K; °C)

z_c : Crustal depth (km)

κ : Thermal diffusivity (km²/Ma)

H : Heat production for the crust (K/Ma)

ρ : Density of the crust (kg/m³)

c : Specific heat capacity (J/kg/K)

Processed values for these parameters are displayed in the Table S3.

We firstly computed the thermal conductivity (k ; Equation 1) and the heat production rate (A ; Equation 2):

$$k = \kappa \times \rho \times c \quad (1)$$

$$A = (H \times \rho \times c) \times 10^6 \quad (2)$$

k : Thermal conductivity (W/m/K)

A: Heat production rate ($\mu\text{W}/\text{m}^3$)

We then obtained the heat flow (q_0 ; Equation 3; mW/m^2).

$$q_0 = \left(\left(\frac{(T_{\text{bottom}} - T_{\text{surface}}) \times k}{z \times 10^3} \right) + \left(A \times (z \times 10^3) \right) \right) \times 10^3 \quad (3)$$

From this computed heat flow, we computed a temperature at z km-depth (T_z ; Equation 4; $^{\circ}\text{C}$):

$$T_z = T_{\text{surface}} + \left(\frac{q_0 \times z \times 10^3}{k} \right) - \left(\left(\frac{A}{2 \times k} \right) \times (z \times 10^3)^2 \right) \quad (4)$$

We finally approximate the geothermal gradient (G ; $^{\circ}\text{C}/\text{km}$) performing the following average (Equation 5):

$$G = \frac{(T_z - T_{\text{surface}})}{z} \quad (5)$$

For example using these values:

$T_{\text{surface}} = 298,15 \text{ K } (25^{\circ}\text{C})$

$T_{\text{bottom}} = 833,15 \text{ K } (560^{\circ}\text{C})$

$z = 56 \text{ km}$

$\kappa = 40 \text{ km}^2/\text{Ma} \rightarrow 1.26 \times 10^{-6} \text{ m}^2/\text{s}$

$H = 279,15 \text{ K}/\text{Ma} \rightarrow 2.04 \times 10^{-13} \text{ }^{\circ}\text{C}/\text{s}$

$\rho = 2750 \text{ kg}/\text{m}^3$

$c = 800 \text{ J}/\text{kg}/\text{K}$

$$k = 1.26 \times 10^{-6} \times 2750 \times 800 = 2.79 \text{ W}/\text{m}/\text{K}$$

$$A = (2.04 \times 10^{-13} \times 2750 \times 800) \times 10^6 = 0.45 \mu\text{W}/\text{m}^3$$

$$A = 4.48 \times 10^{-7} \text{ W}/\text{m}^3$$

$$q_0 = \left(\left(\frac{(560 - 25) \times 2.79}{56 \times 1000} \right) + (4.48 \times 10^{-7} \times (56 \times 1000)) \right) \times 1000 = 51.74 \text{ mW}/\text{m}^2$$

$$q_0 = 5.17 \times 10^{-2} \text{ W}/\text{m}^2$$

$$T_5 = 25 + \left(\frac{5.17 \times 10^{-2} \times 5 \times 1000}{2.79} \right) - \left(\left(\frac{4.48 \times 10^{-7}}{2 \times 2.79} \right) \times (5 \times 1000)^2 \right) = 115.76^{\circ}\text{C}$$

$$G = \frac{(115.76 - 25)}{5} = \mathbf{18^{\circ}\text{C}/\text{km}}$$

Text S2. Neighborhood Algorithm (NA) inversions with Pecube

We used Pecube in inverse mode to quantitatively constrain parameter values (tectono-morphic scenarios; Figures S38 and Tables S3-S4) that best reproduce the input thermochronological data. Pecube uses the implemented Neighborhood Algorithm (NA; Sambridge, 1999a;b), which explores the parameter space by progressive misfit minimization and permits to rapidly converge toward a best-fitting tectono-morphic scenario. The Misfit function (Equations 6 and 7) measures the difference between

observed and predicted data, with three different parts: the thermochronological ages (M1; Equation 6), the fission track-length distributions (Kuiper test for comparison between observed and predicted track-length distributions) and the thermal history (M2: Equation 7):

$$M1 = \sqrt{\frac{\sum_{i=0}^{N1} \frac{(A_o^i - A_p^i)^2 / dA_i^2}{N1}}{N1}} \quad (6)$$

With A_o , the observed thermochronological ages, dA , the analytical error, A_p , the predicted ages from Pecube and $N1$ the total number of implemented ages.

$$M2 = \sqrt{\frac{\sum_{i=0}^{N2} \frac{(T_o^i - T_p^i)^2 / dT_i^2}{N2}}{N2}} \quad (7)$$

For the thermal histories, T_o is the implemented temperature derived from QTQt, dT is the error of these temperatures (95% reliability; QTQt; Gallagher, 2012), T_p is the predicted temperature by Pecube and $N2$ is the total number of steps defining the thermal history. More details regarding the misfit functions are available in the Pecube user guide on GitHub following this link: <https://github.com/jeanbraun/Pecube>.

Text S3. Limitation for fault geometry at the surface with Pecube

Implementation of complex fault systems cannot be modeled with Pecube because of geometrical and fault-velocity computational issues. Although the Apurimac fault system trace at the surface is curved (x/y axis; Figure 2), we approximate it in Pecube by a straight and oblique fault separating the Altiplano from the Eastern Cordillera. The geometry of the fault at depth (z axis) is explored with PECUBE and discussed in the manuscript.

Text S4. Topography / relief inversed with Pecube – non convergent parameters

The relief amplification factor did not converge during PECUBE inverse modeling and cannot be quantified for the Altiplano and the Eastern Cordillera (Figures S39 and S40). We notwithstanding further explored this parameter through forward modeling to assess to what extent it is needed for our thermochronological data. Trial-and-error approach using PECUBE forward models suggests an increase in topographic relief between 10 and 0 Ma to reproduce accurately the observed thermochronological data (although this parameter is not a first order control on the exhumation history). Since the relief-amplification factor can be interpreted as a proxy for incision, we linked this needed relief increase to the large-scale capture of the Abancay Deflection system by the Urubamba and Apurimac drainage network (Gérard et al. in press) and subsequent incision since ~10 Ma. From our thermochronological record and literature data interpretation (van Heiningen et al., 2005; Gérard et al., in press), we further propose that the capture of the Abancay Deflection likely occurred during the late Miocene/early Pliocene around ~5 Ma and that associated erosion started slightly after.

Text S5. Pecube outcomes imposing a warmer geothermal gradient (30°C/km)

To test the robustness of our computed geothermal gradient for the Abancay Deflection (~20°C/km), which is crucial for exhumation computation, we performed the same inversion as presented in the manuscript for both the Altiplano and the Eastern Cordillera model with identical parameters except for the geotherm, imposing a warmer geothermal gradient of 30°C/km as compiled and accepted for the Bolivian Eastern Cordillera (Barnes et al., 2008).

For the Altiplano block model, we explored exhumation rates for the entire crustal block between 40 Ma to present-day for values ranging from -10 to 10 km/m.y (subsidence vs. exhumation). This parameter nicely converge to 0.45 ± 0.10 km/m.y. (Figure S45a). Processing this best-fitting rate into forward modeling we observed that, counter intuitively, even if the geothermal gradient is warmer, the area needs twice exhumation rather than if a colder geothermal gradient is used (0.2 ± 0.1 km/m.y. with a gradient of $18^\circ\text{C}/\text{km}$). Ages and T-t paths are less reproducible and predicted thermochronological ages are, in most of the cases, younger than the observed data (Figure S45b and c). Consequently, the $\sim 20^\circ\text{C}/\text{km}$ geotherm seems to be the most suitable gradient for this part of the Altiplano.

For the Eastern Cordillera block model, we explored exhumation rates for the entire crustal block between 50 Ma to present-day for values ranging from 0 to 5 km/m.y. At the same time, we inverted the timing for the Apurimac fault system activation (between 0 and 14 Ma) and the fault velocity (0 to 10 km/m.y.). These three parameters nicely converge to values of 0.2 ± 0.1 km/m.y. (Figure S46a), 7 ± 1 Ma and 1.4 ± 0.4 km/m.y. respectively (Figure S46b). Exhumation rate for the entire crustal block with this warmer geotherm is identical with the one obtained with the $18^\circ\text{C}/\text{km}$ gradient. The timing for faulting initiation is quite similar too (7 ± 1 Ma vs. 5 ± 2 Ma). The fault velocity is, however, divided by ~ 2 (1.4 ± 0.4 km/m.y. ($30^\circ\text{C}/\text{km}$) vs. 2.9 ± 0.6 ($18^\circ\text{C}/\text{km}$)), which is quite logical as the geothermal gradient is multiplied by ~ 2 . Whatever the geothermal gradient imposed, tectonic is needed through the Apurimac fault system to reproduce the thermochronological ages (Figure S46c and d). The data reproducibility is, nevertheless, lower with the warmer geotherm and predicted ages are older than observed ones (Figure S46c), especially for the AHe system. The $\sim 20^\circ\text{C}/\text{km}$ geotherm, in that case, seems to be the most suitable gradient for this part of the Eastern Cordillera.

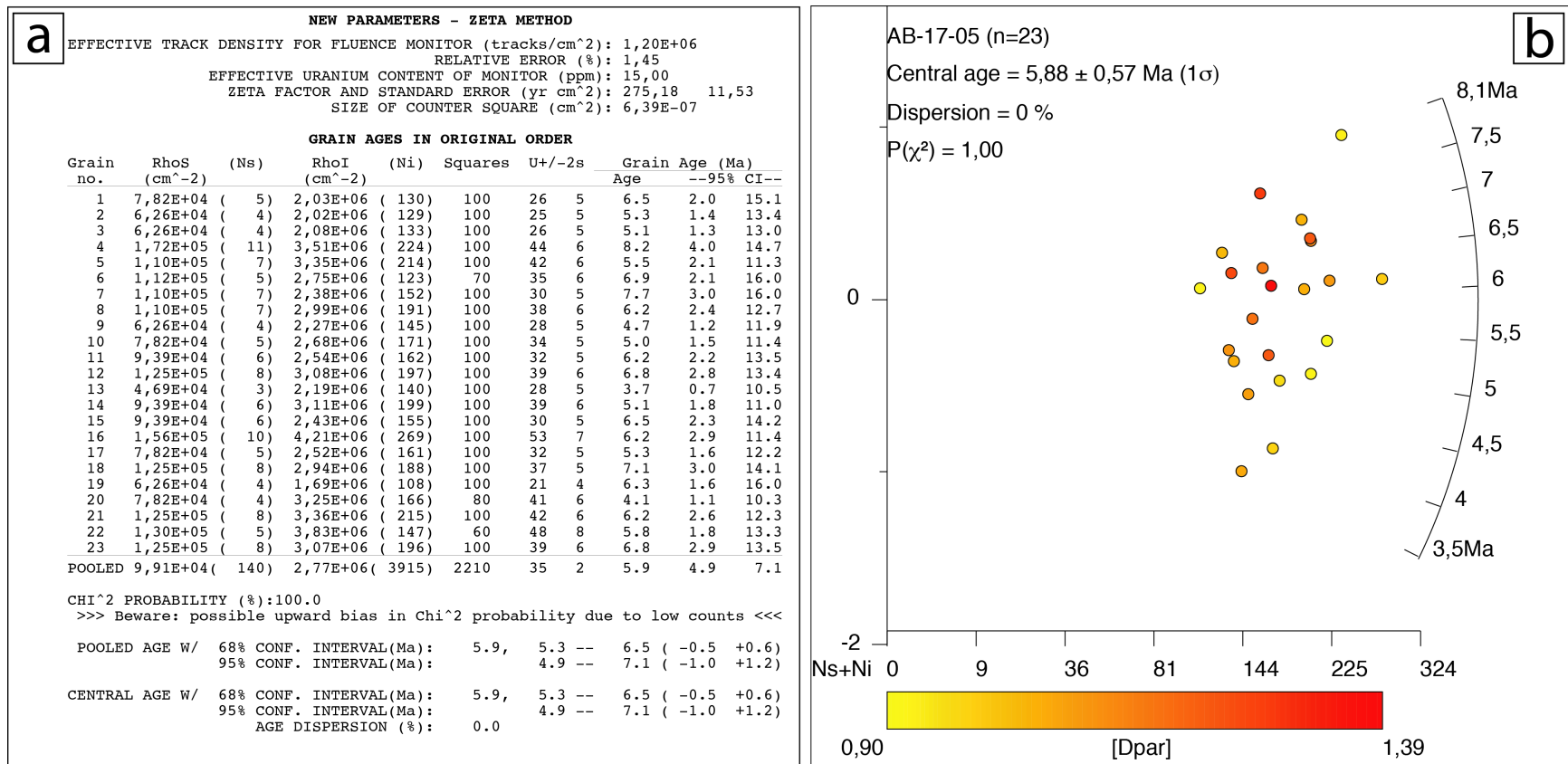


Figure S1. AFT single-grain data (a) and radial plots (b) for sample AB-17-05. See Figure S44 for location.

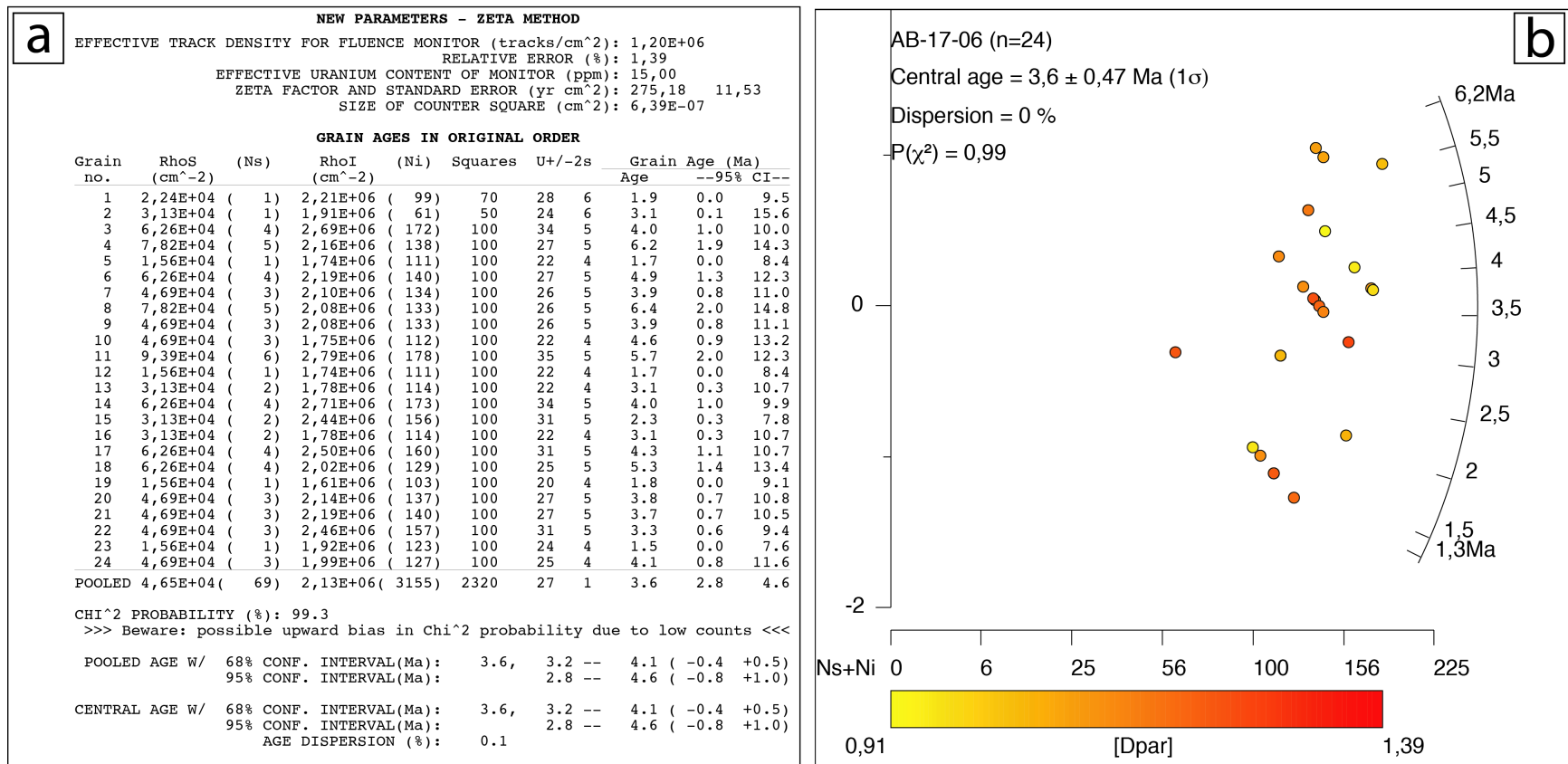


Figure S2. AFT single-grain data (a) and radial plots (b) for sample AB-17-06. See Figure S44 for location.

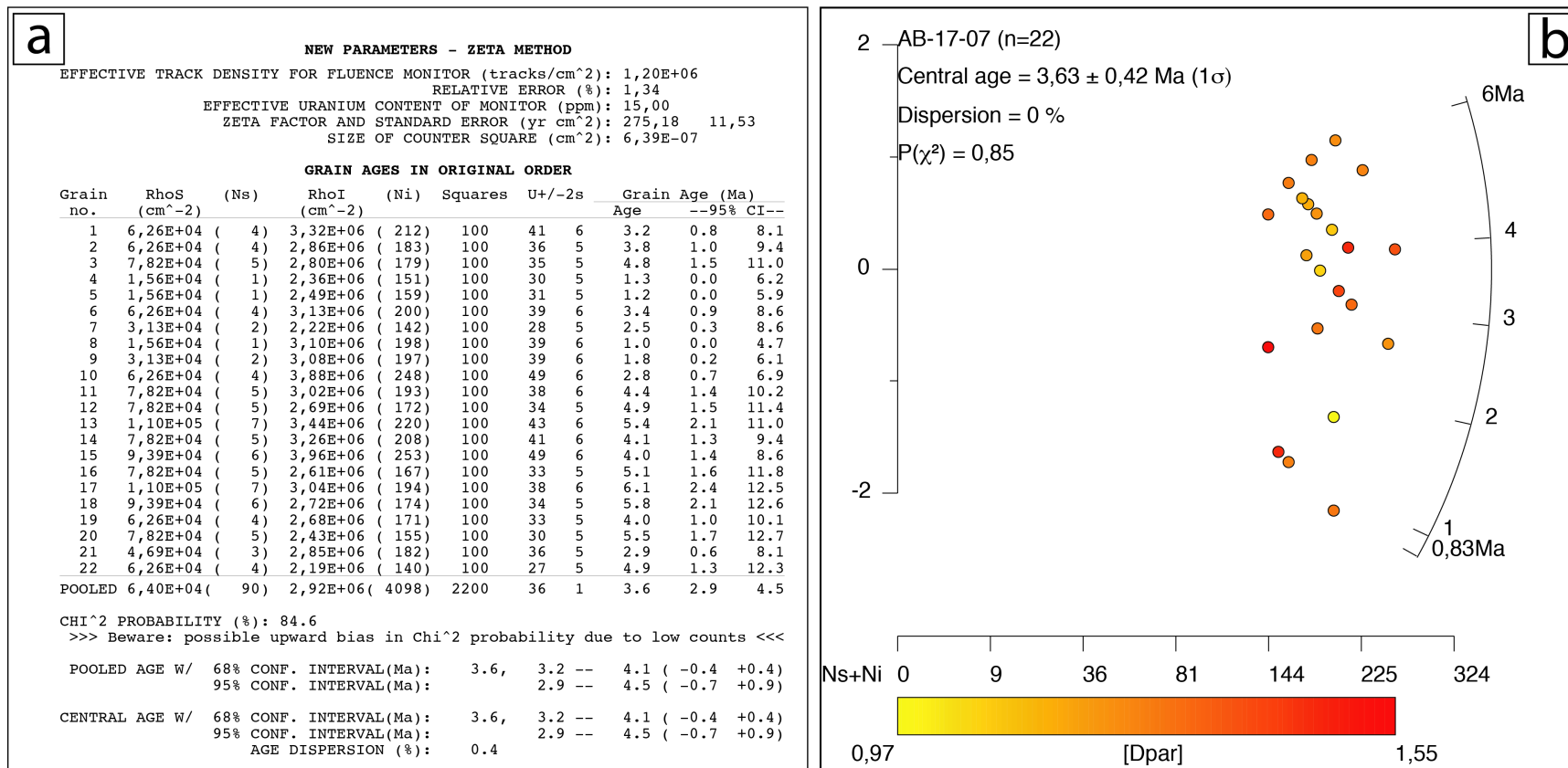


Figure S3. AFT single-grain data (a) and radial plots (b) for sample AB-17-07. See Figure S44 for location.

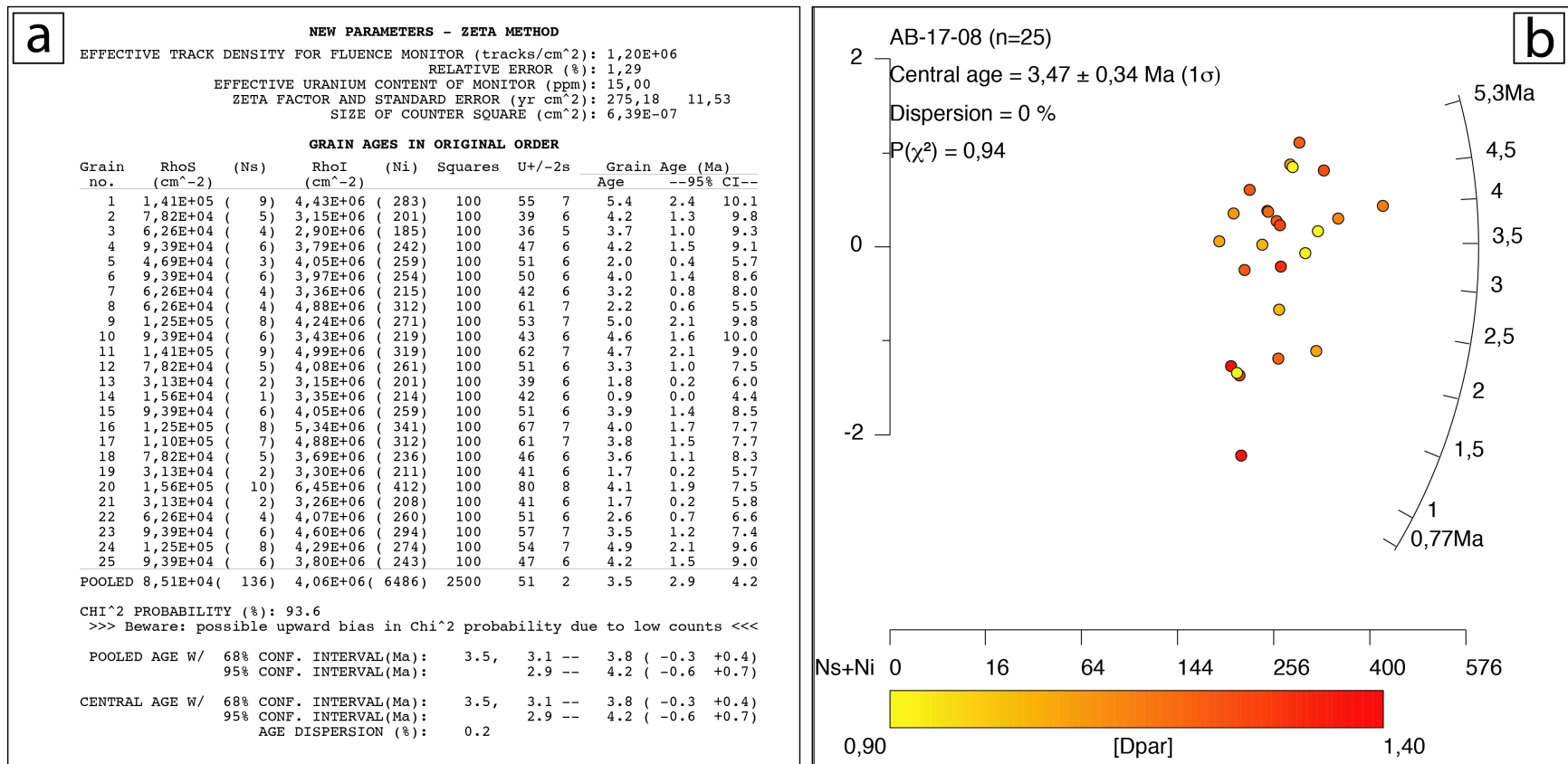


Figure S4. AFT single-grain data (a) and radial plots (b) for sample AB-17-08. See Figure S44 for location.

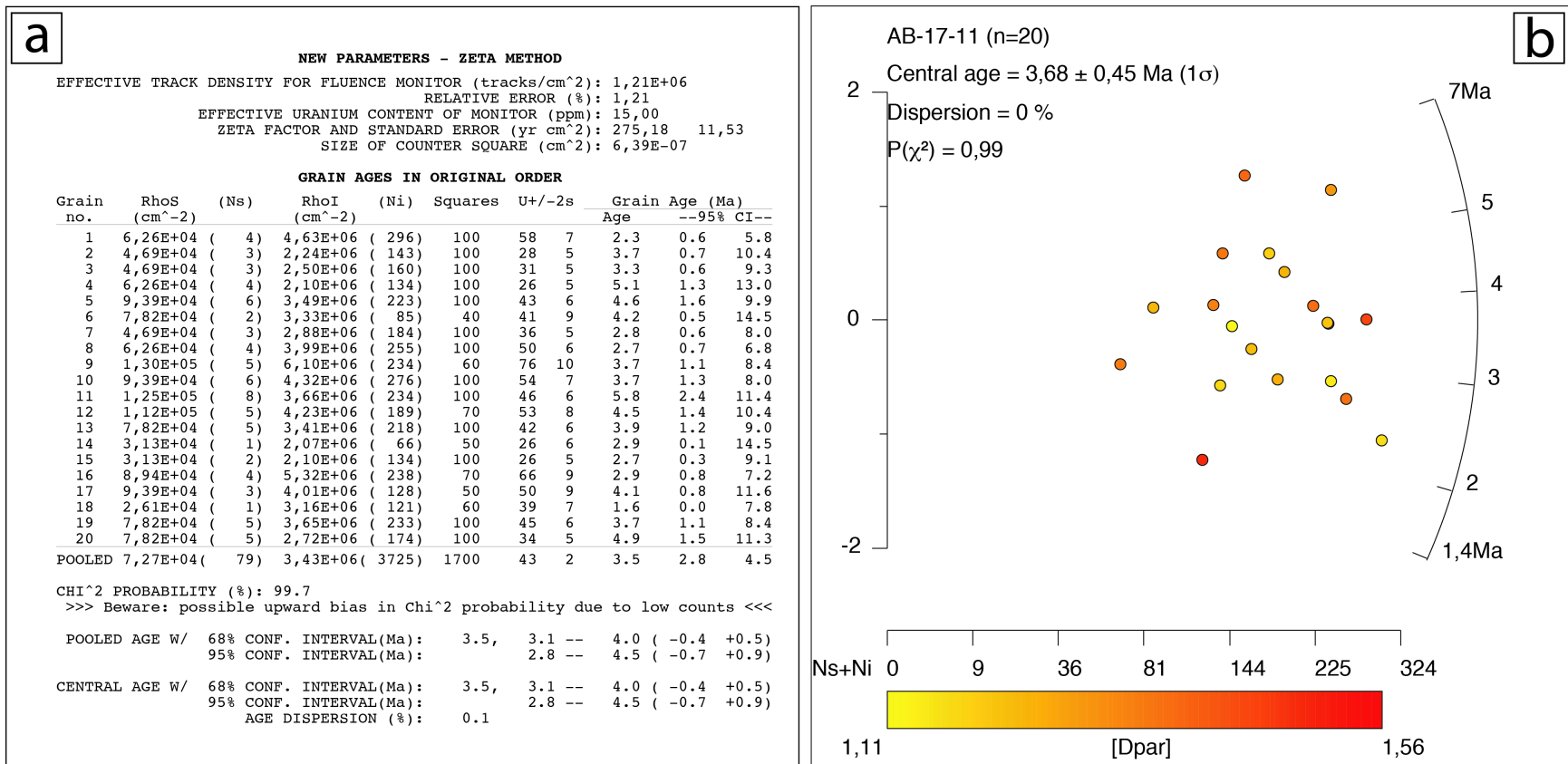


Figure S5. AFT single-grain data (a) and radial plots (b) for sample AB-17-11. See Figure S44 for location.

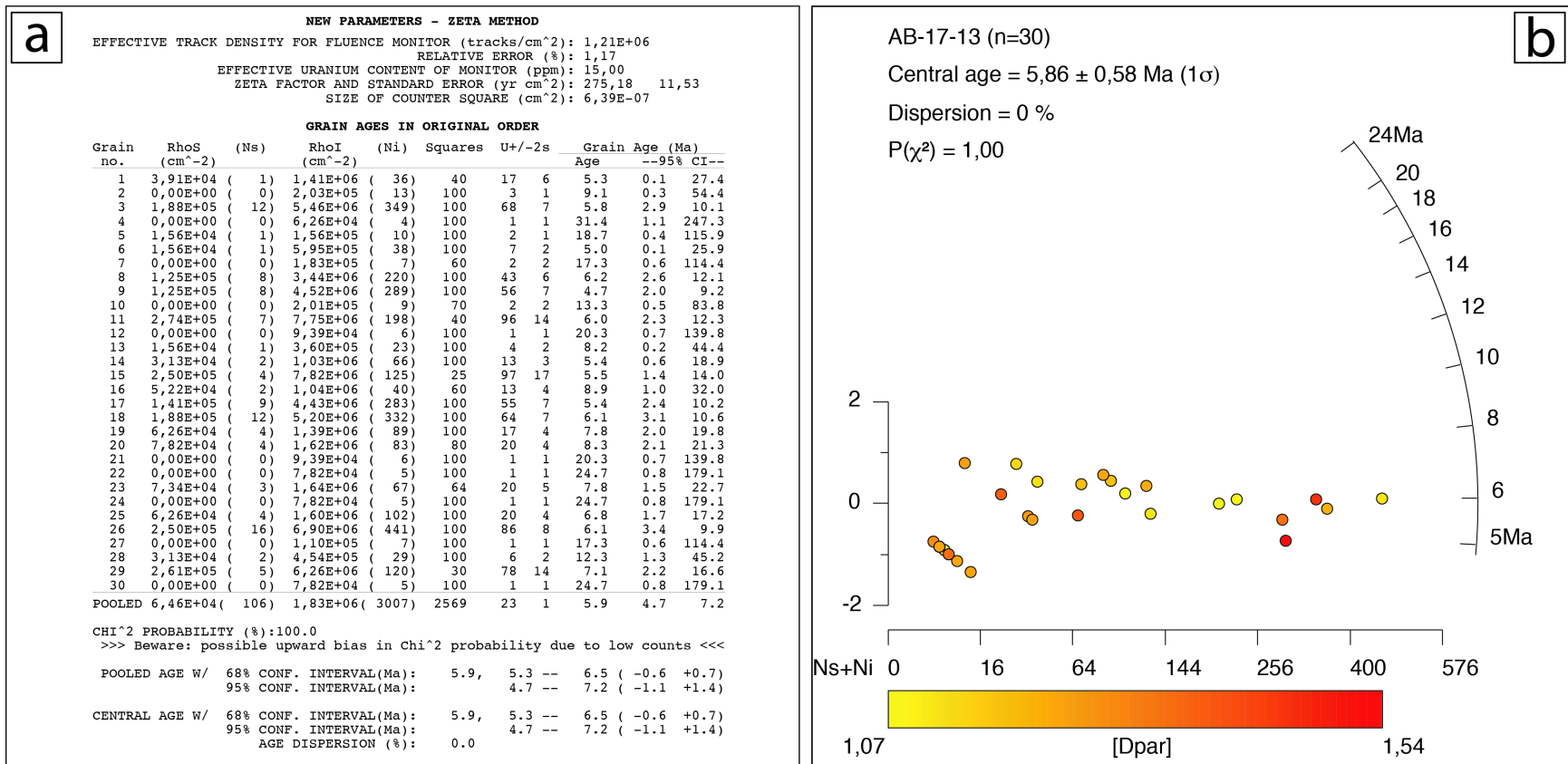


Figure S6. AFT single-grain data (a) and radial plots (b) for sample AB-17-13. See Figure S44 for location.

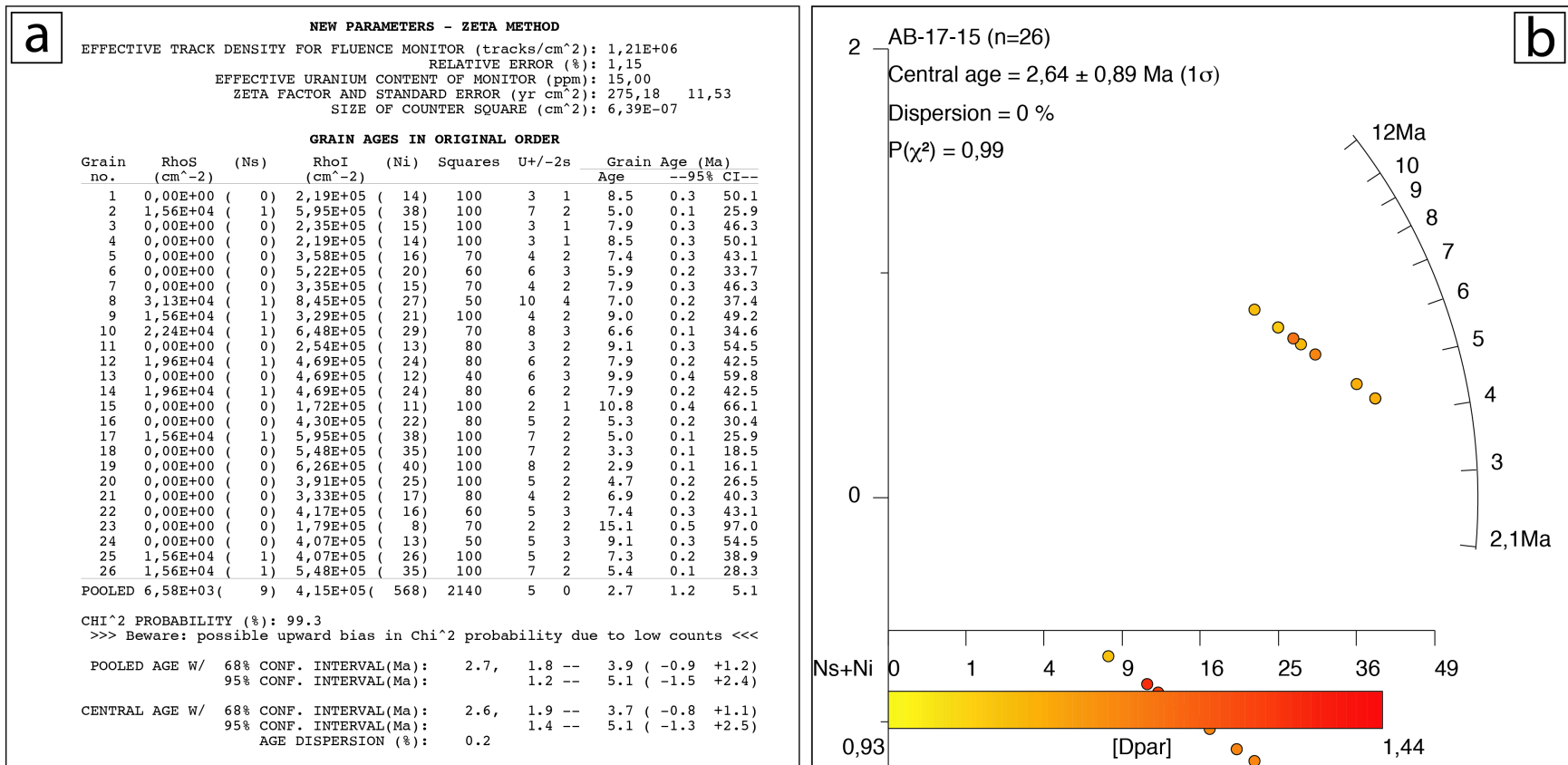


Figure S7. AFT single-grain data (a) and radial plots (b) for sample AB-17-15. See Figure S44 for location.

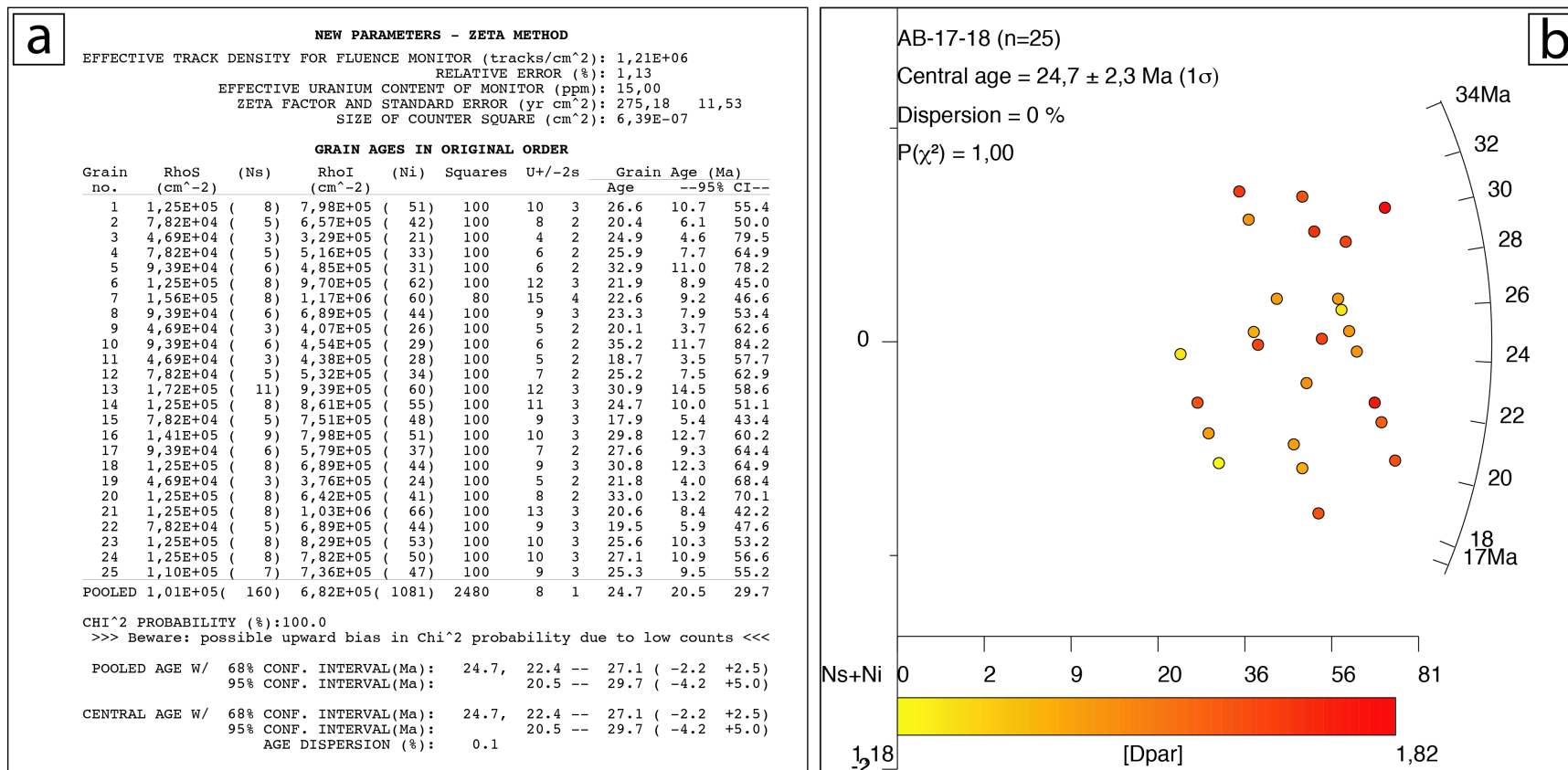


Figure S8. AFT single-grain data (a) and radial plots (b) for sample AB-17-18. See Figure S44 for location.

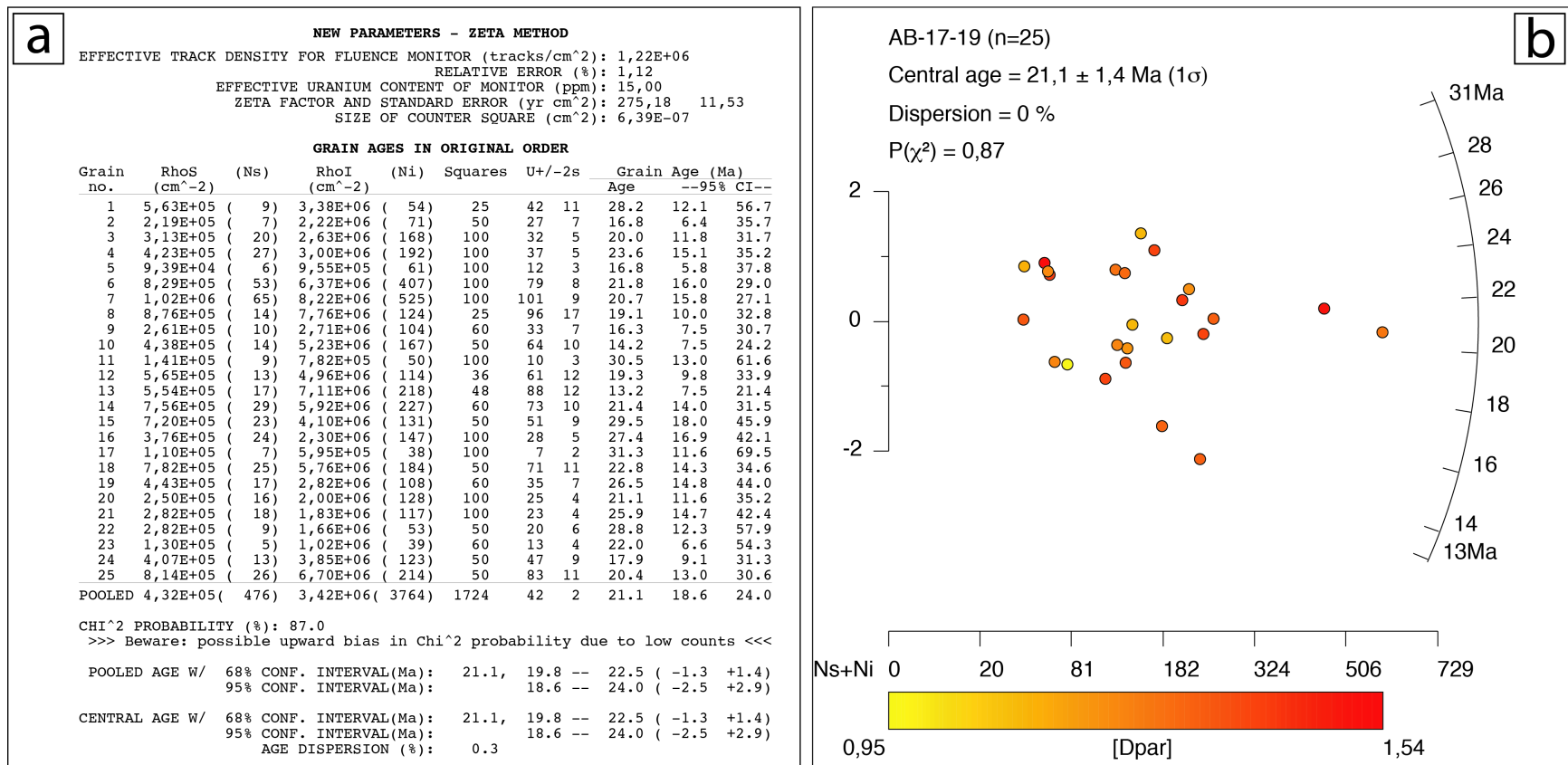


Figure S9. AFT single-grain data (a) and radial plots (b) for sample AB-17-19. See Figure S44 for location.

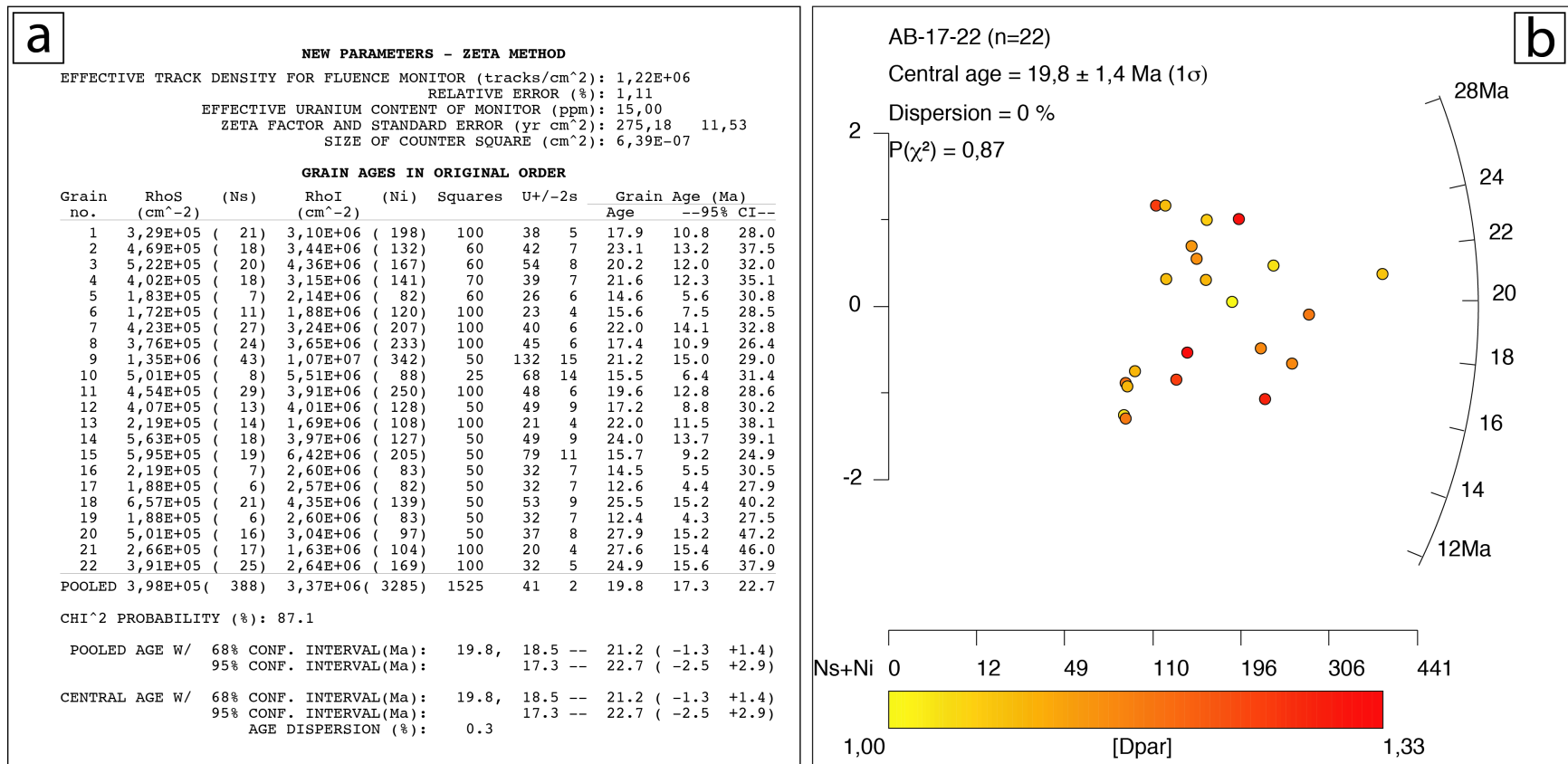


Figure S10. AFT single-grain data (a) and radial plots (b) for sample AB-17-22. See Figure S44 for location.

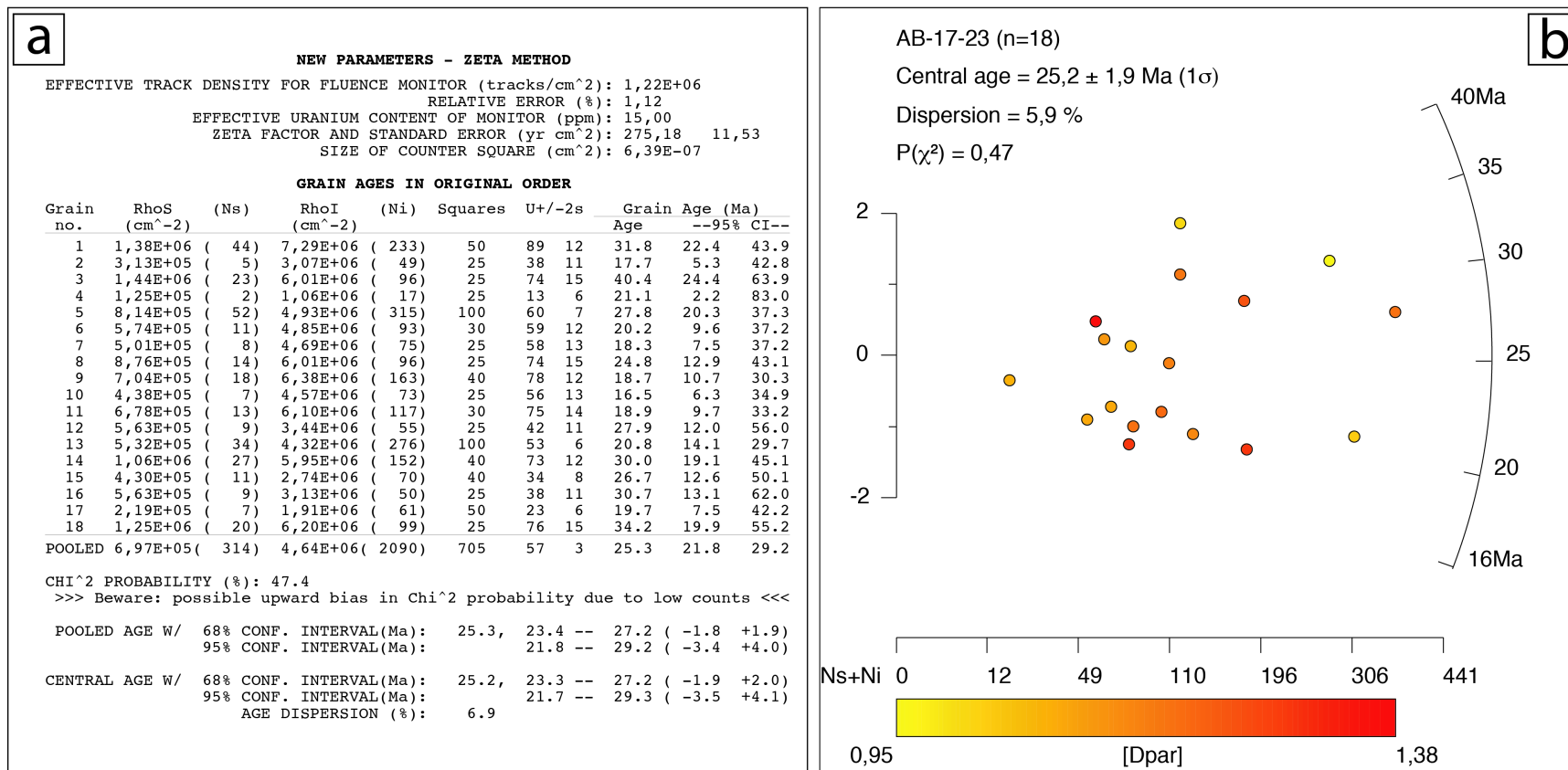


Figure S11. AFT single-grain data (a) and radial plots (b) for sample AB-17-23. See Figure S44 for location.

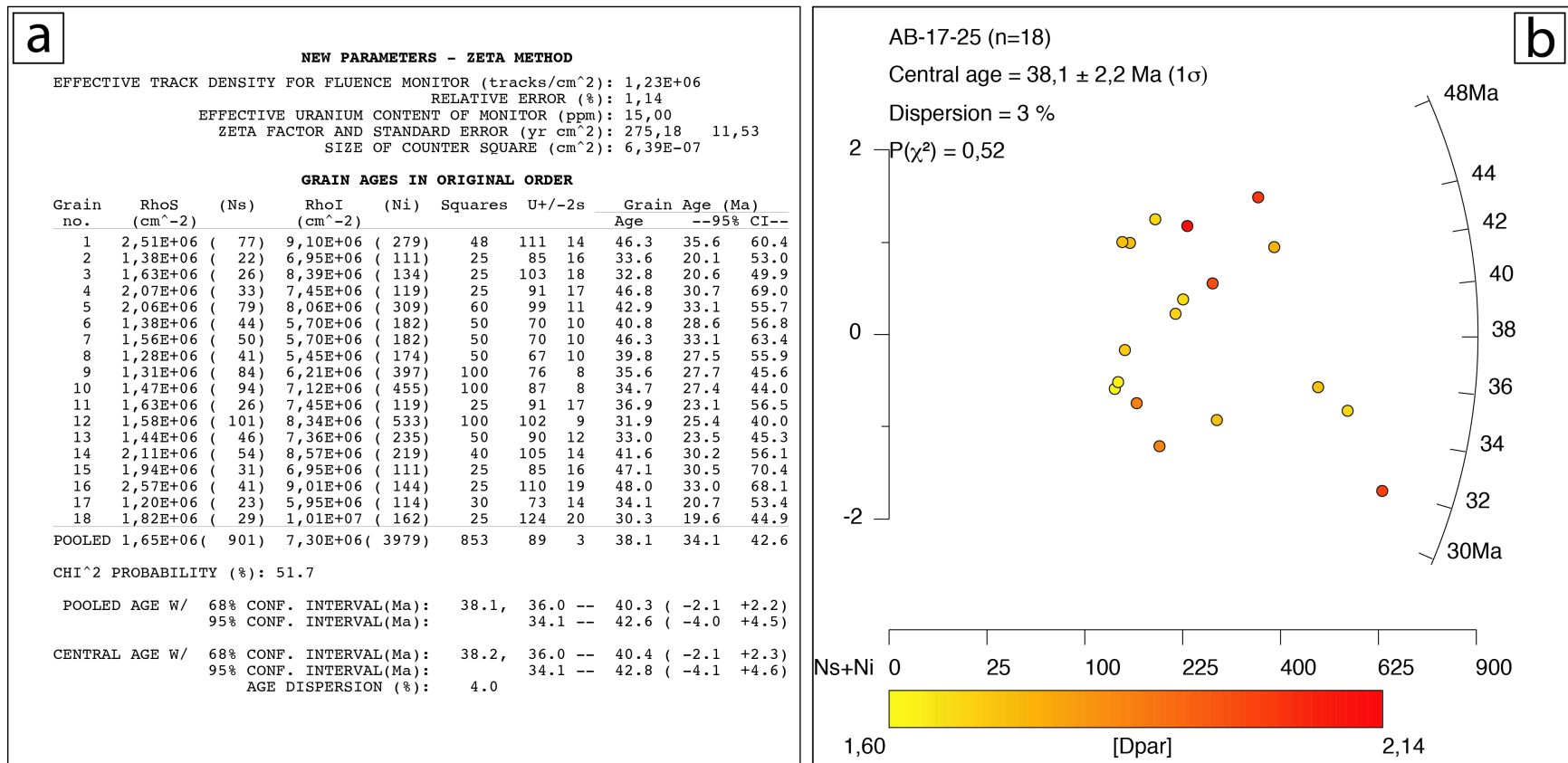


Figure S12. AFT single-grain data (a) and radial plots (b) for sample AB-17-25. See Figure S44 for location.

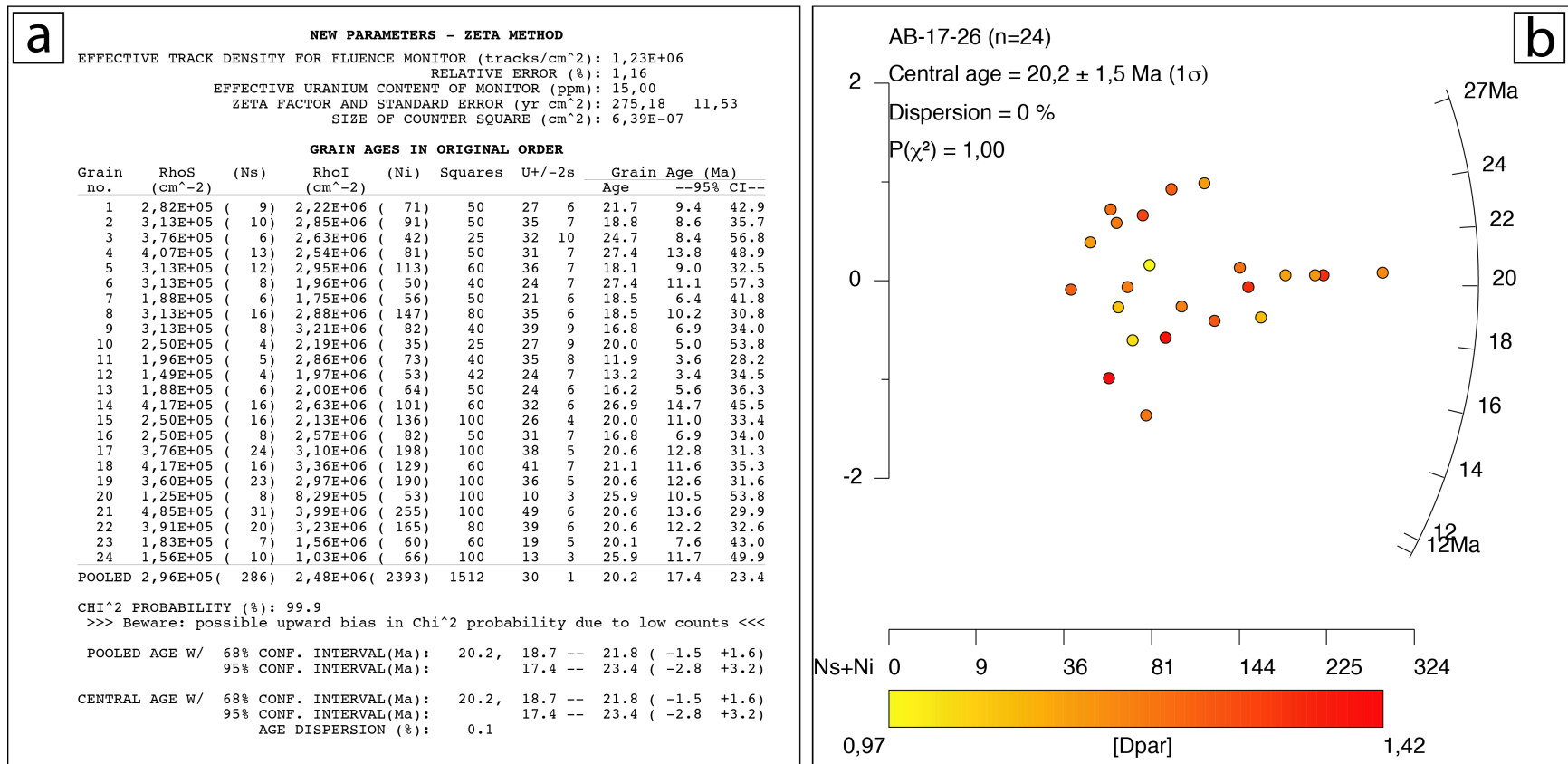


Figure S13. AFT single-grain data (a) and radial plots (b) for sample AB-17-26. See Figure S44 for location.

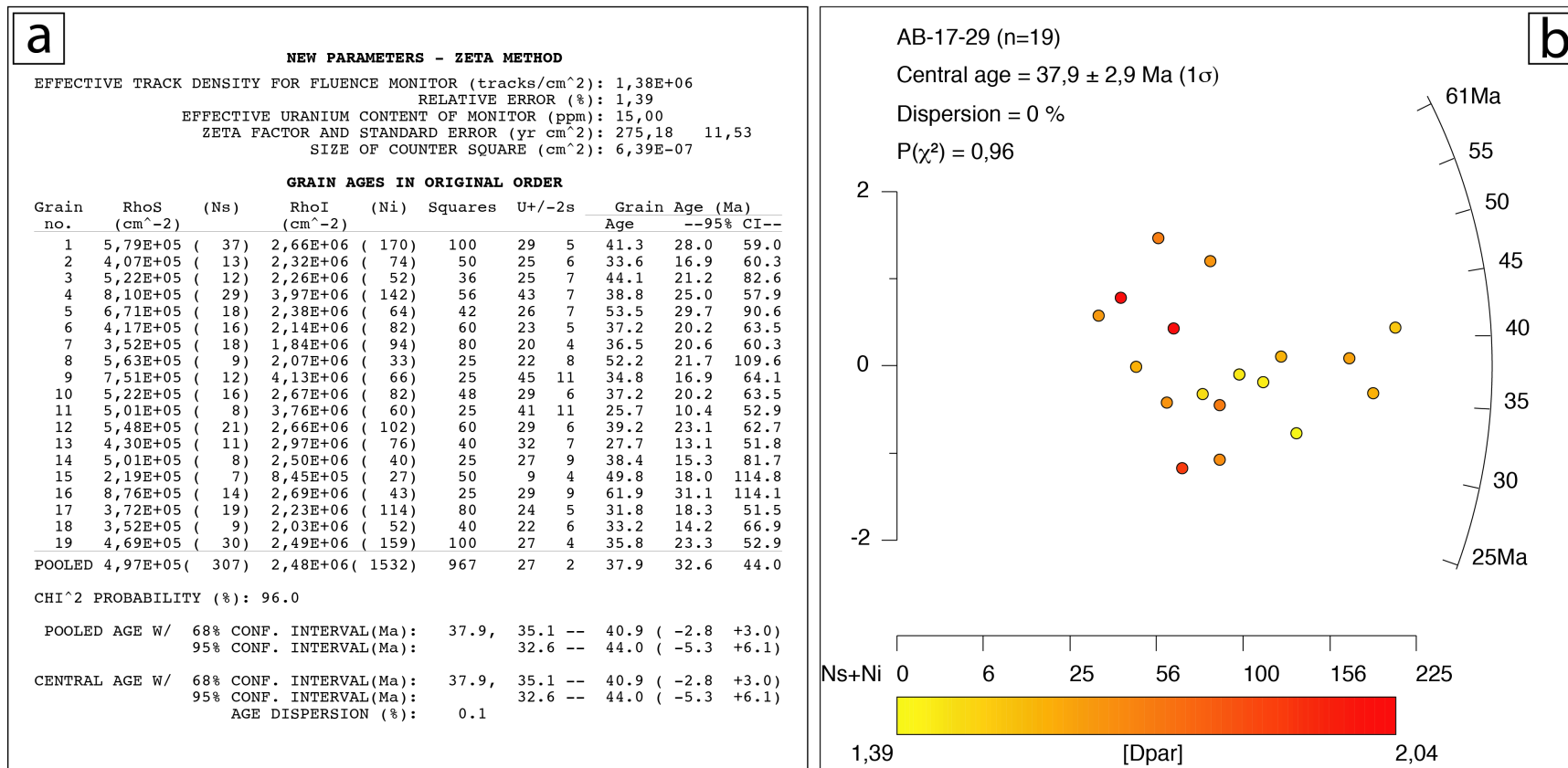


Figure S14. AFT single-grain data (a) and radial plots (b) for sample AB-17-29. See Figure S44 for location.

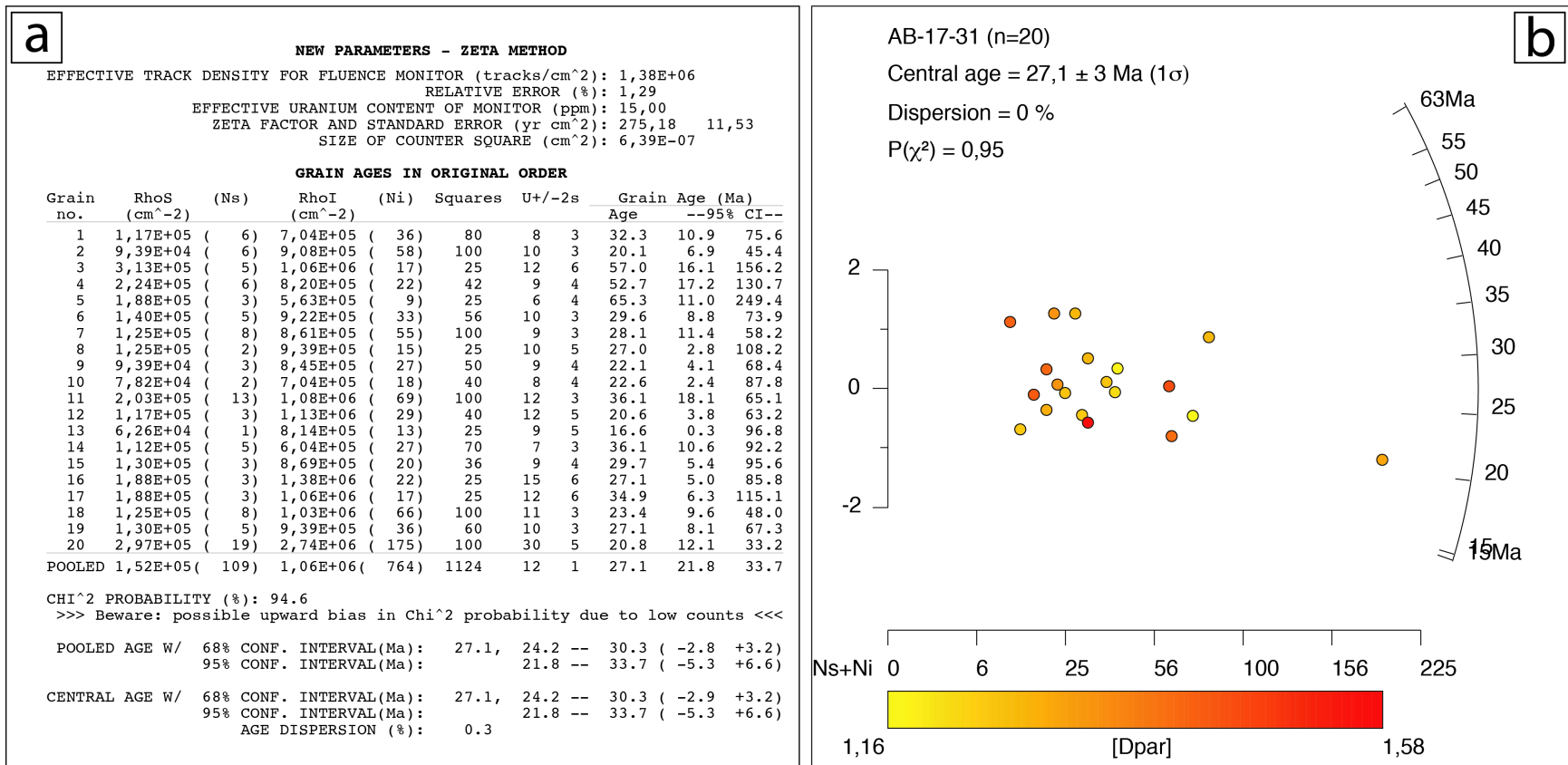


Figure S15. AFT single-grain data (a) and radial plots (b) for sample AB-17-31. See Figure S44 for location.

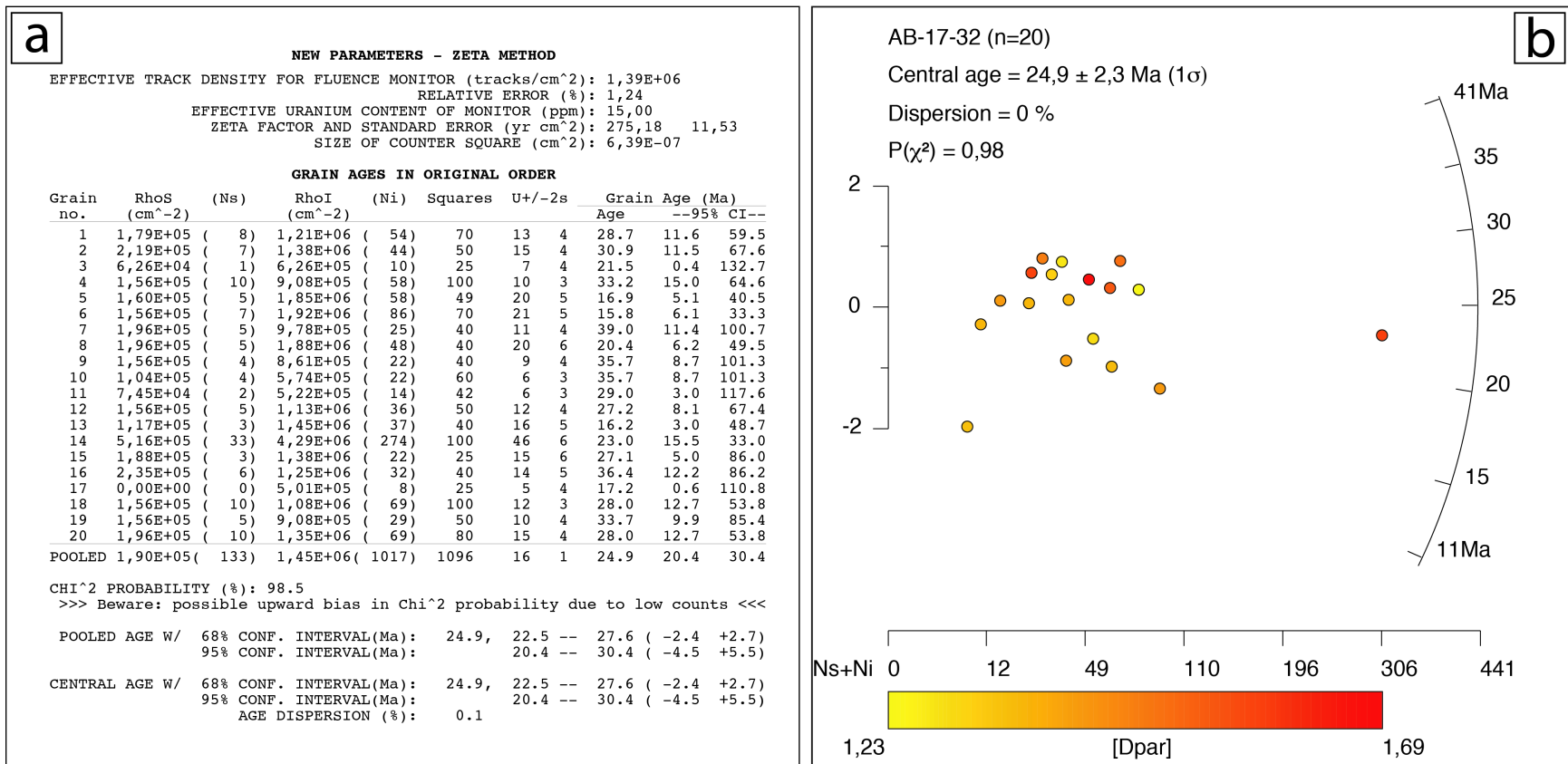


Figure S16. AFT single-grain data (a) and radial plots (b) for sample AB-17-32. See Figure S44 for location.

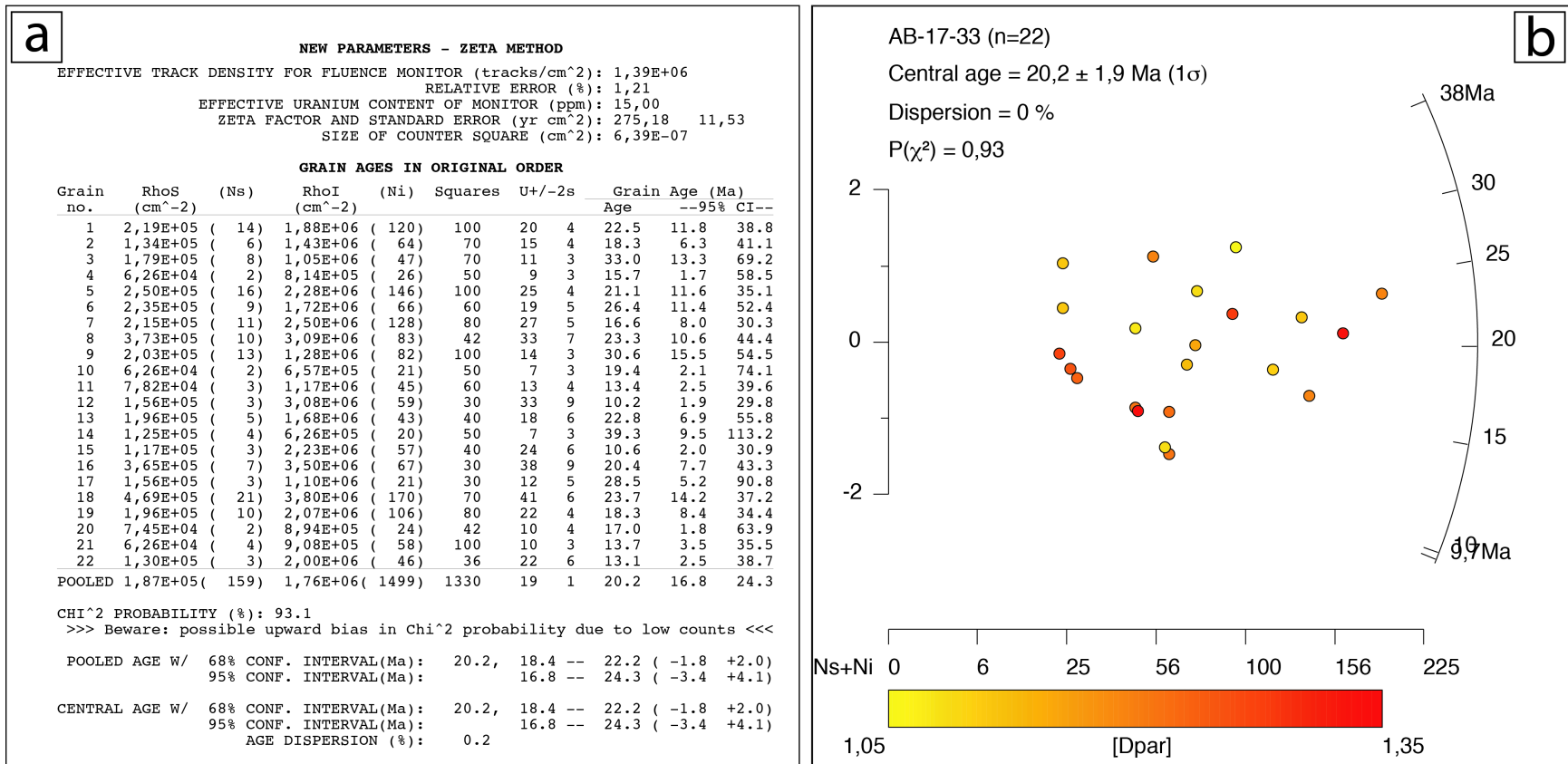


Figure S17. AFT single-grain data (a) and radial plots (b) for sample AB-17-33. See Figure S44 for location.

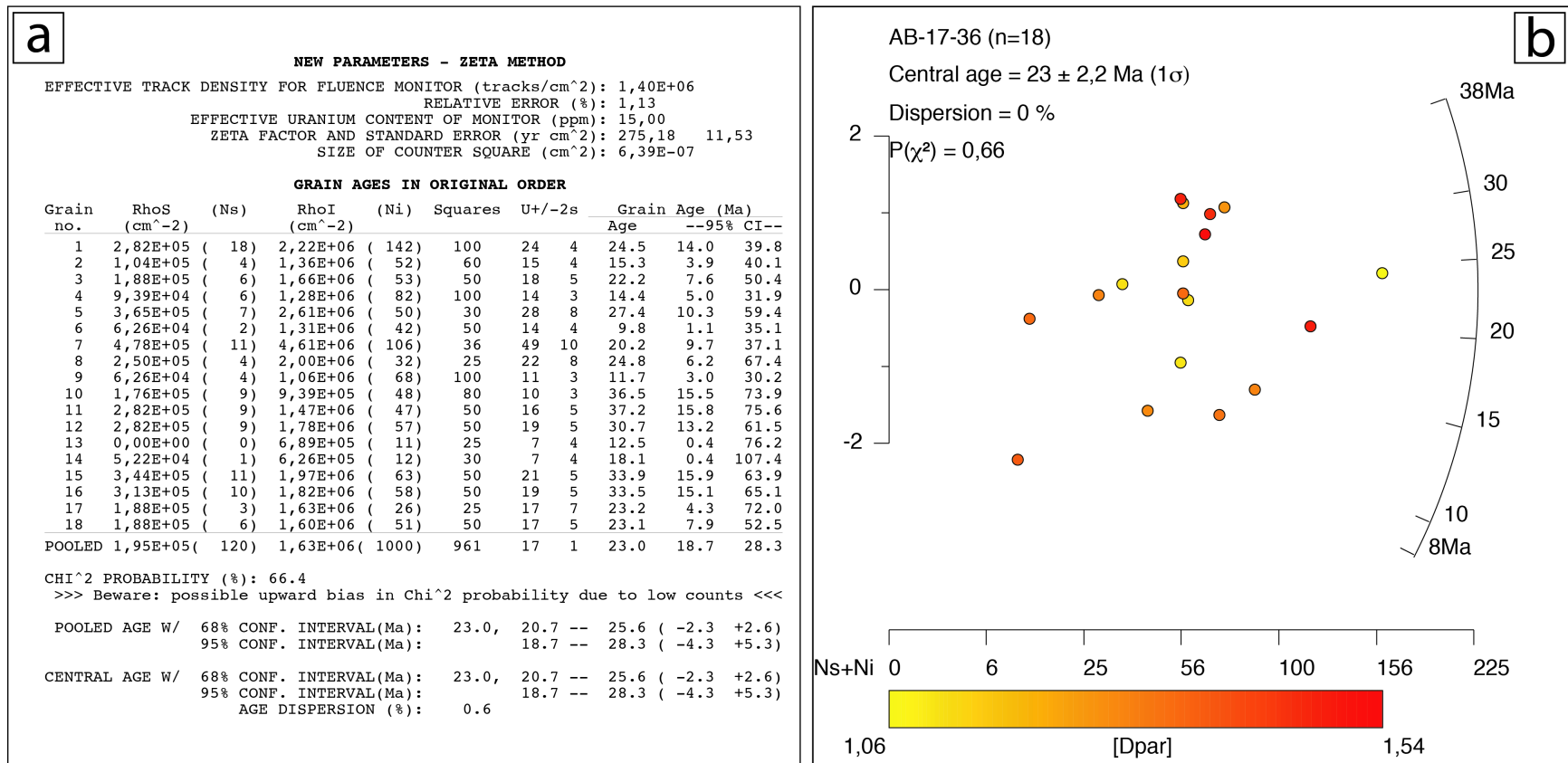


Figure S18. AFT single-grain data (a) and radial plots (b) for sample AB-17-36. See Figure S44 for location.

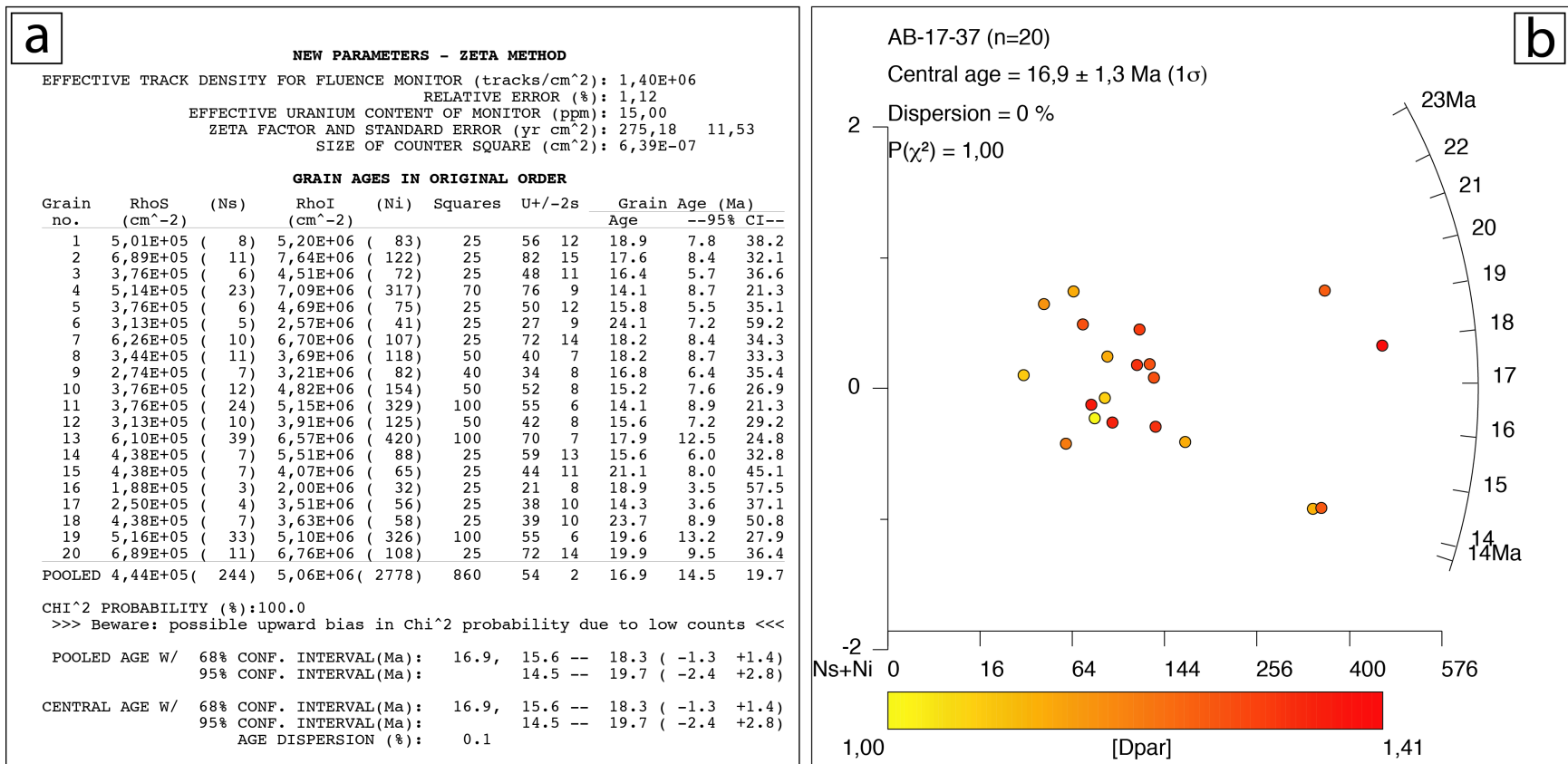


Figure S19. AFT single-grain data (a) and radial plots (b) for sample AB-17-37. See Figure S44 for location.

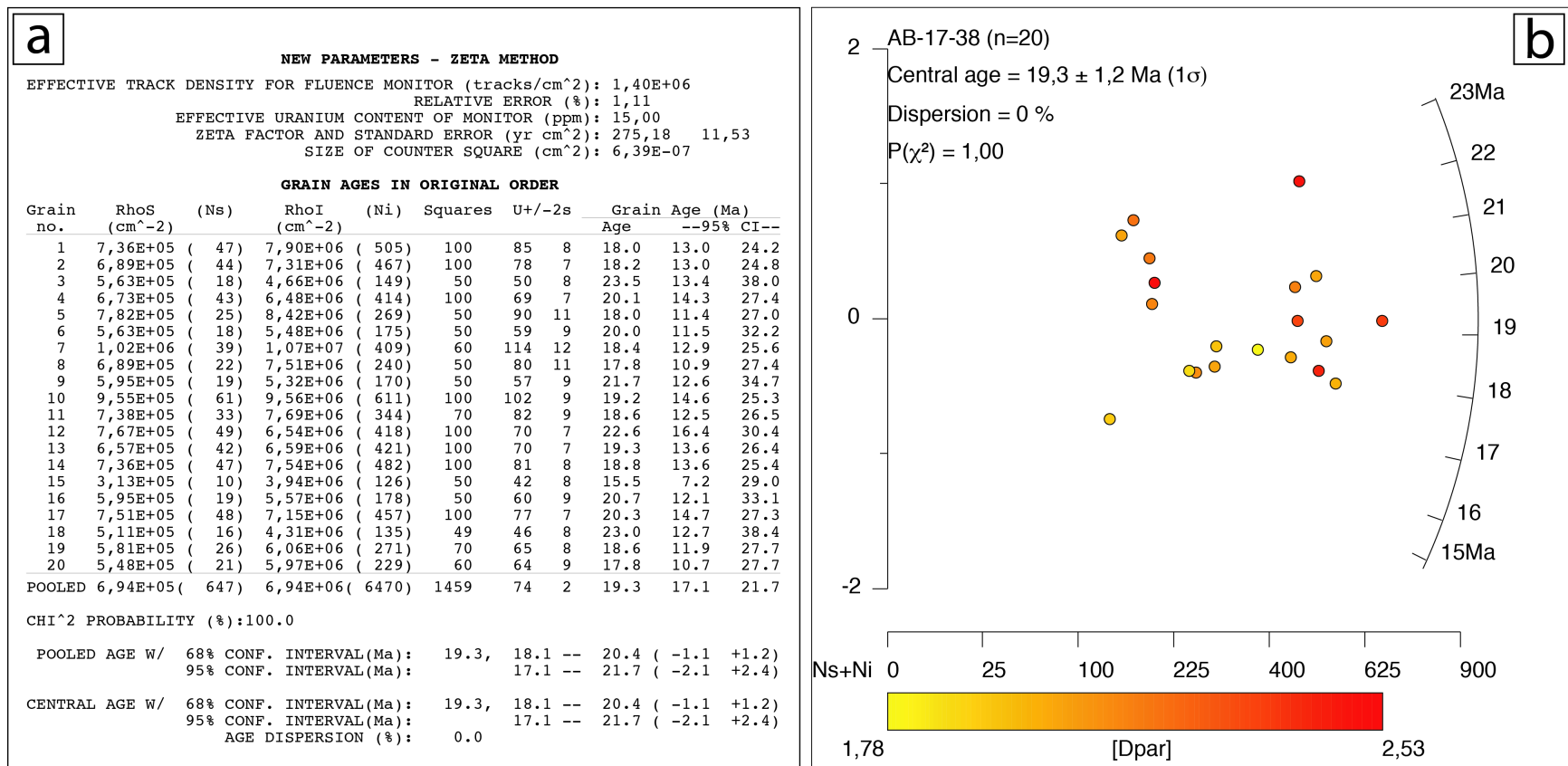


Figure S20. AFT single-grain data (a) and radial plots (b) for sample AB-17-38. See Figure S44 for location.

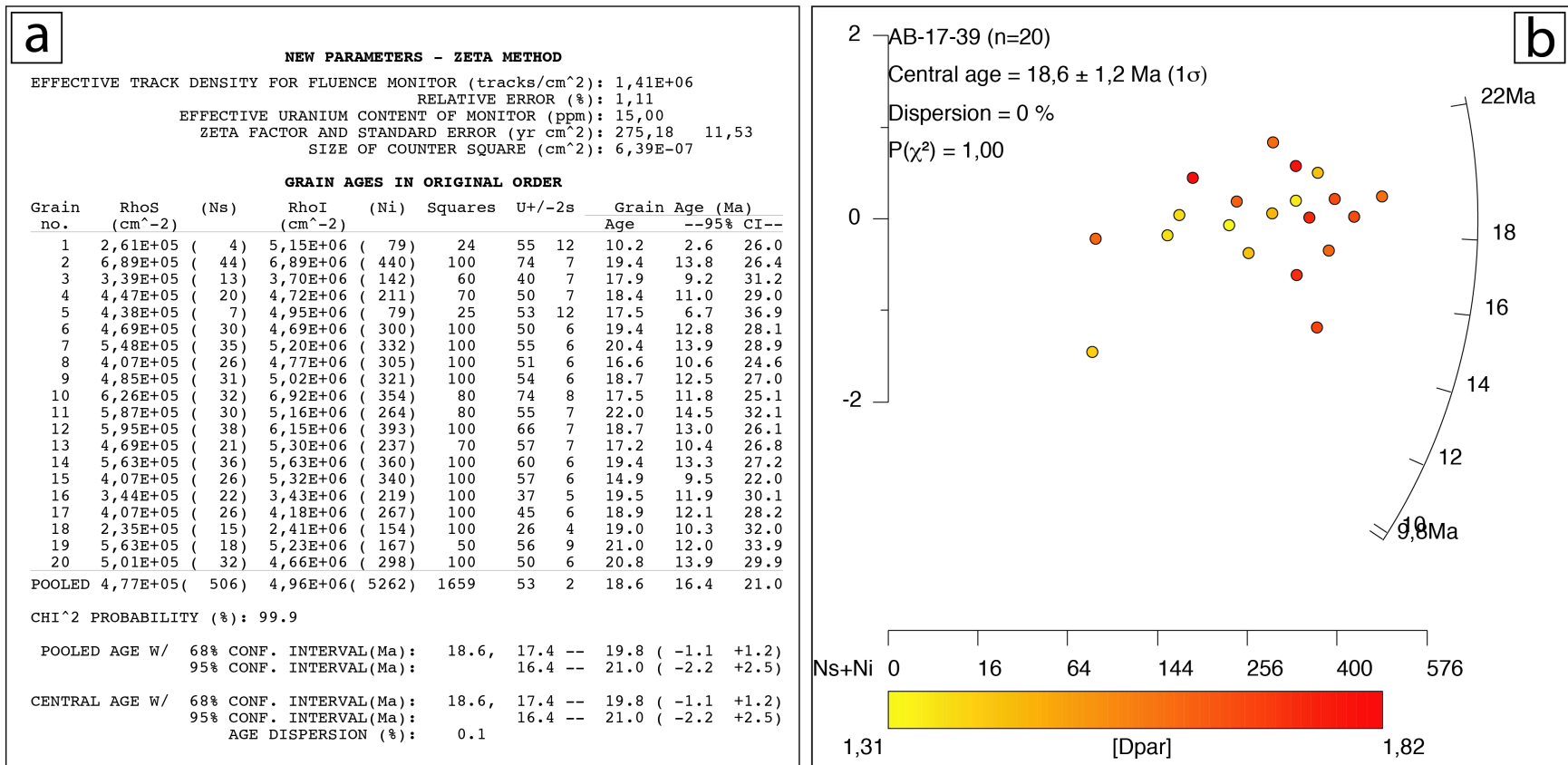


Figure S21. AFT single-grain data (a) and radial plots (b) for sample AB-17-39. See Figure S44 for location.

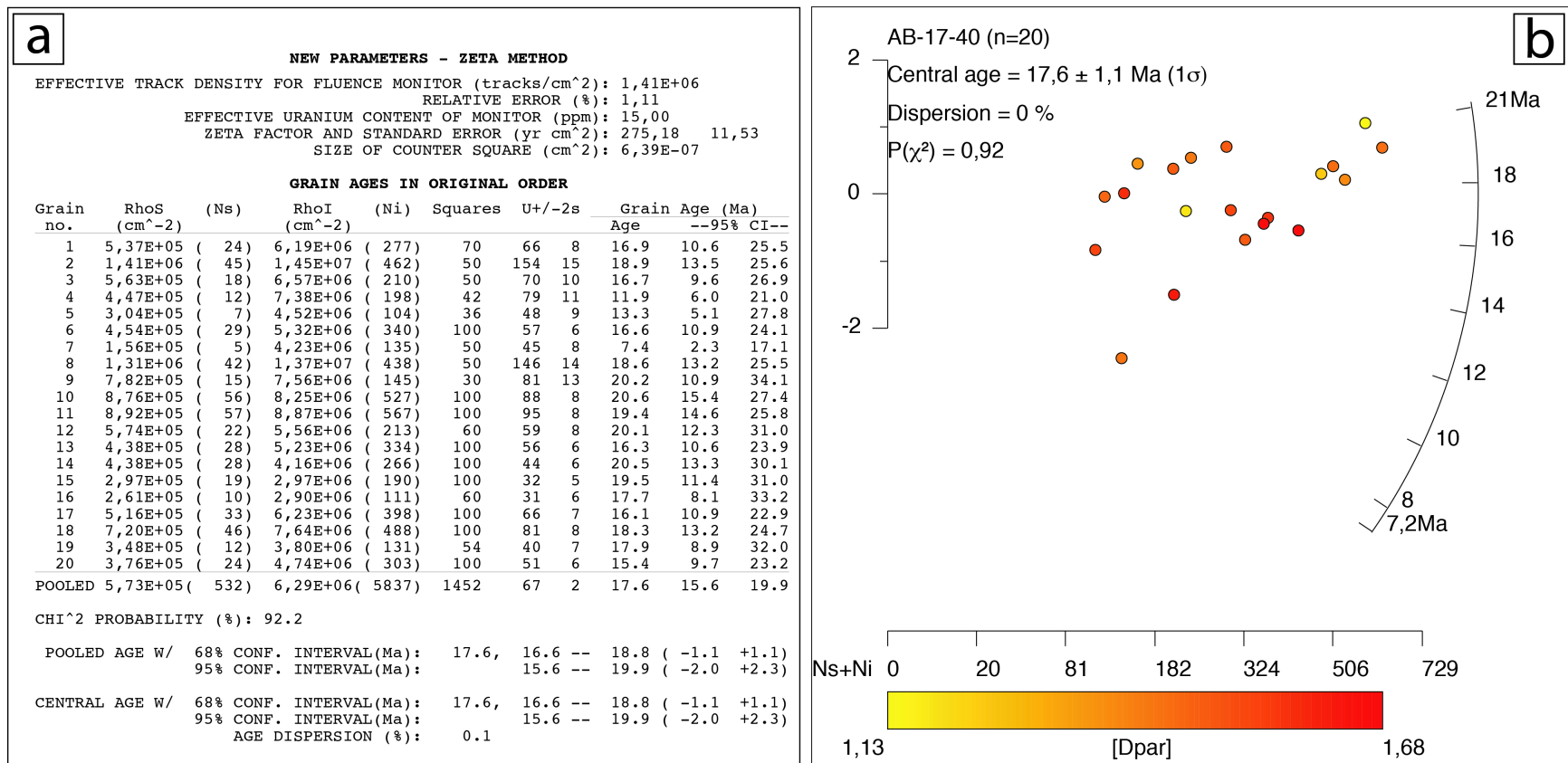


Figure S22. AFT single-grain data (a) and radial plots (b) for sample AB-17-40. See Figure S44 for location.

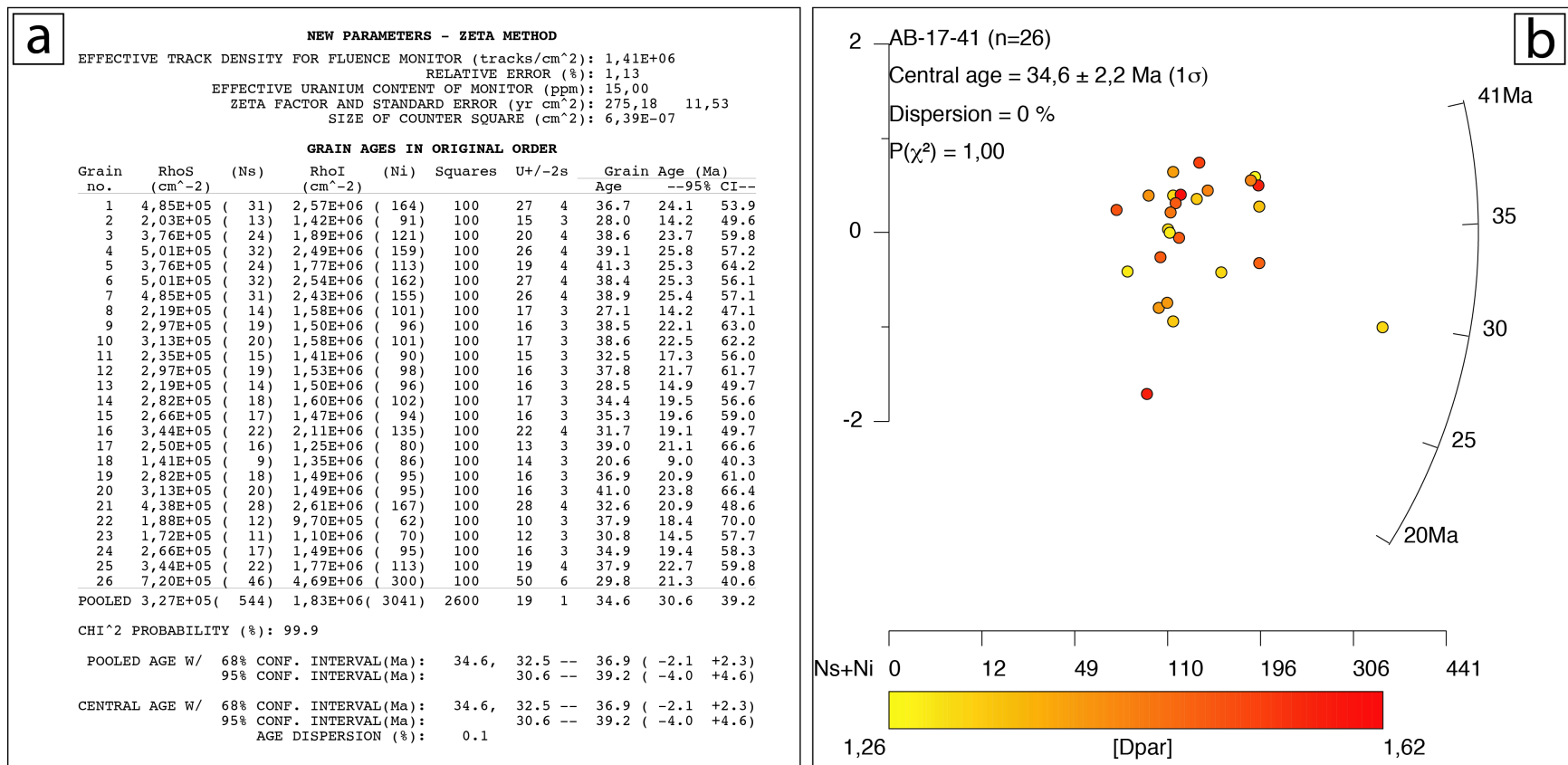


Figure S23. AFT single-grain data (a) and radial plots (b) for sample AB-17-41. See Figure S44 for location.

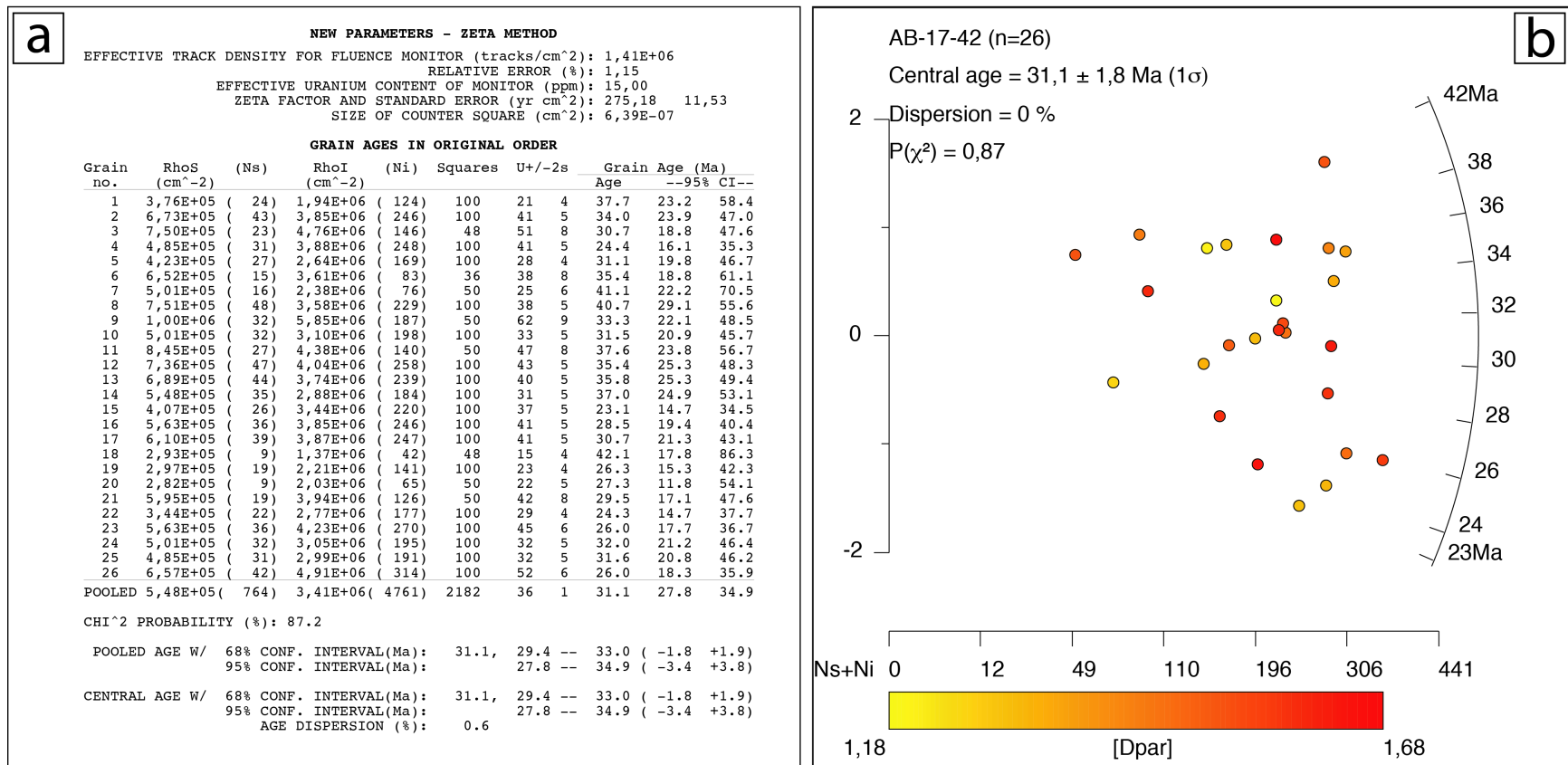


Figure S24. AFT single-grain data (a) and radial plots (b) for sample AB-17-42. See Figure S44 for location.

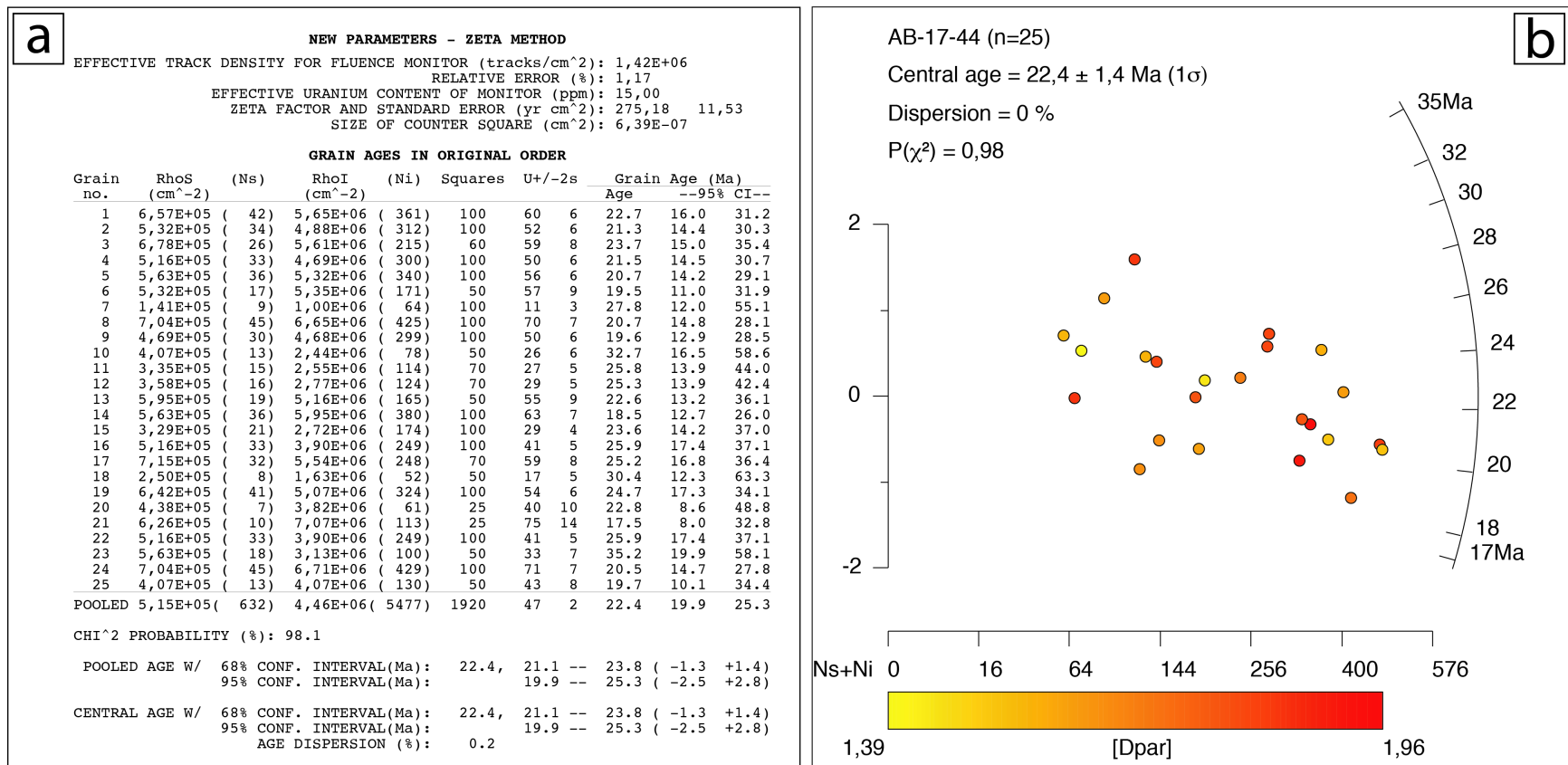


Figure S25. AFT single-grain data (a) and radial plots (b) for sample AB-17-44. See Figure S44 for location.

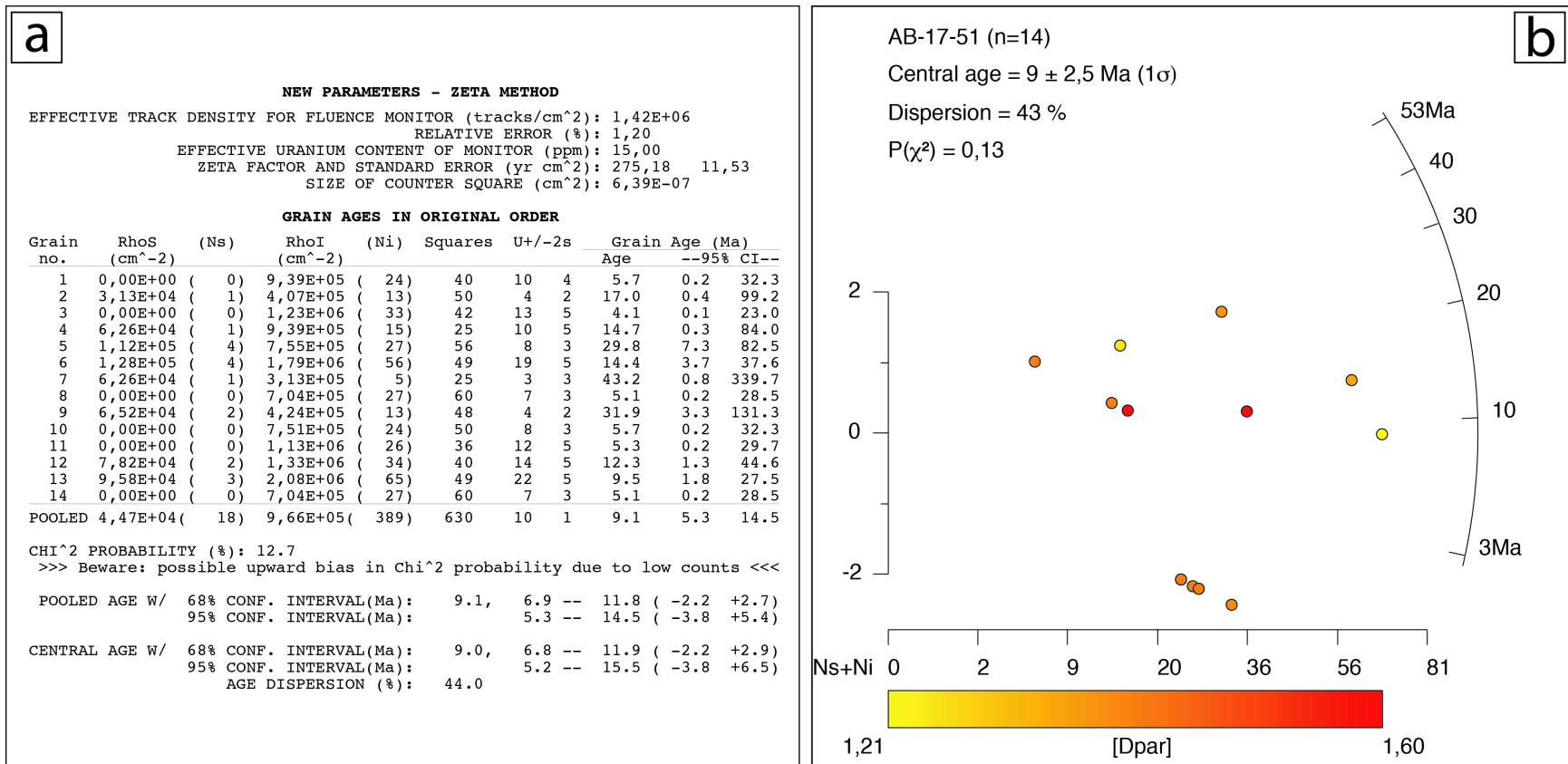


Figure S26. AFT single-grain data (a) and radial plots (b) for sample AB-17-51. See Figure S44 for location.

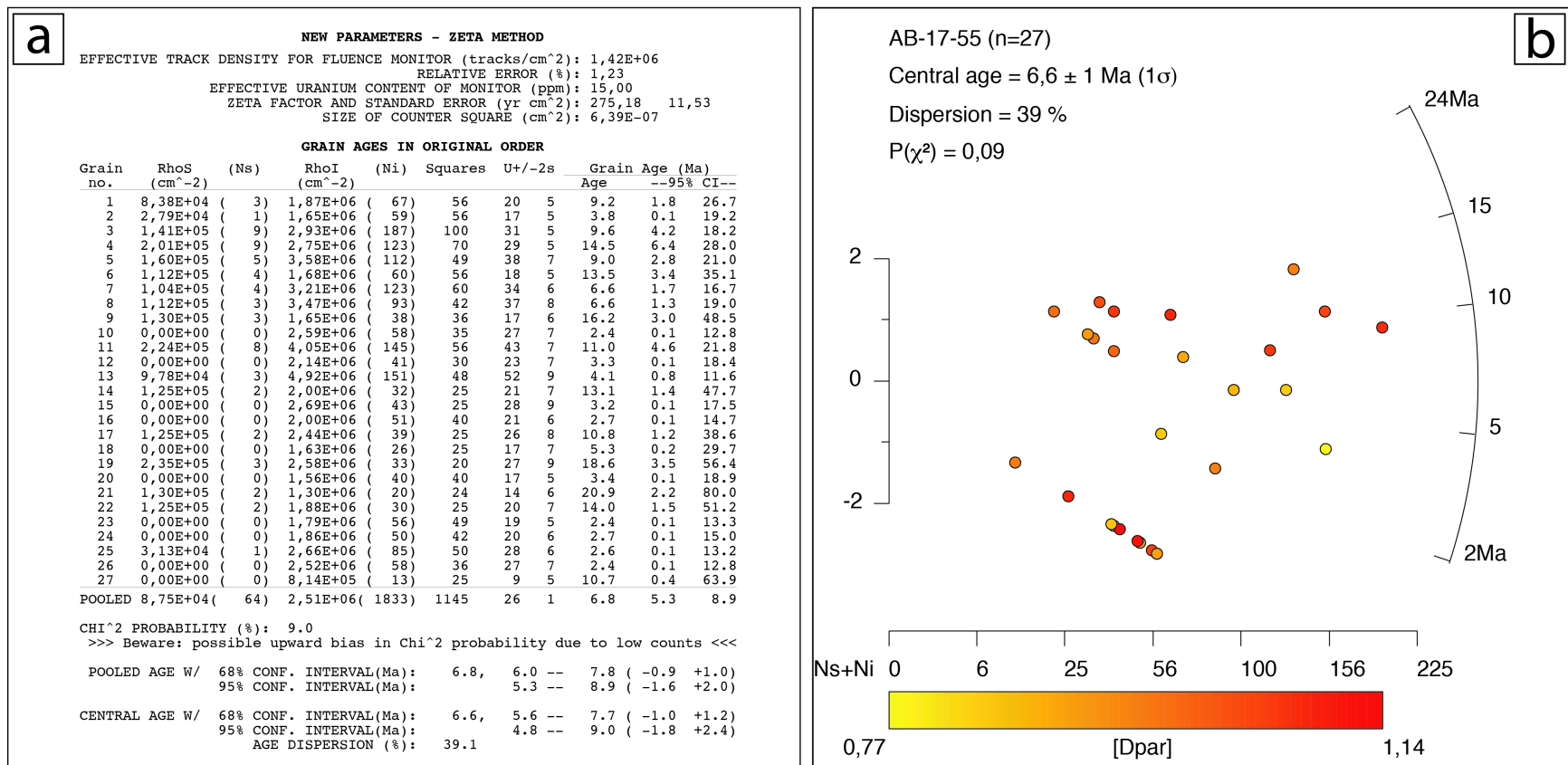


Figure S27. AFT single-grain data (a) and radial plots (b) for sample AB-17-55. See Figure S44 for location.

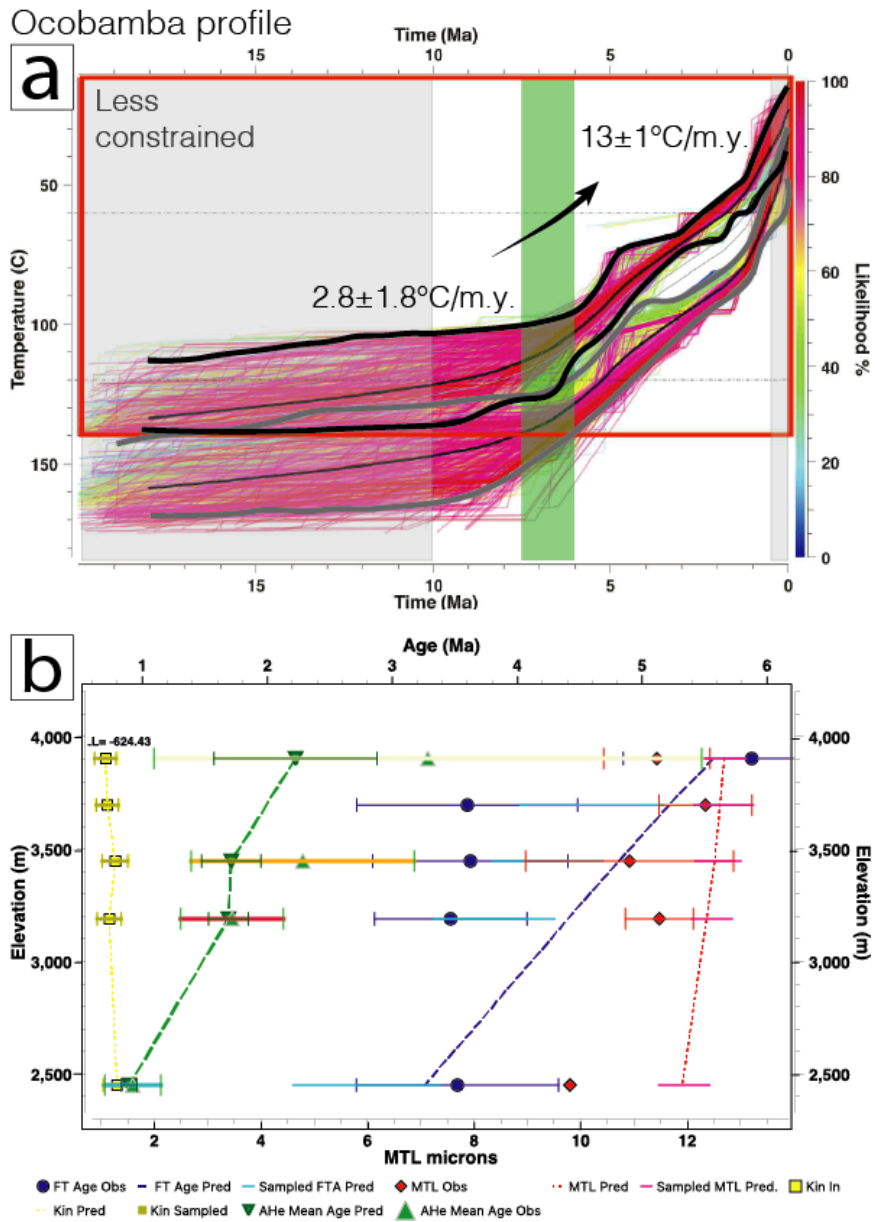


Figure S28. QTQt inversion results for the Ocobamba high-altitudinal profile. a) Time-temperature paths obtained by inversion of AHe and AFT thermochronology data from the Ocobamba age-elevation profile using QTQt (AB-17-05 to AB-17-11). The red square shows the explored time and temperature range for inversion. The colored lines show the T-t paths for the top and the bottom samples with their respective likelihood (see color scale on right). The solid black and grey lines show the expected model and its 95% reliable interval for the thermal histories of the top and bottom samples, respectively. The grey lines in between represent the expected cooling paths for the intermediate samples. The green vertical band indicates the well-constrained acceleration of cooling at ~6.5 Ma. Cooling rates derived from QTQt are indicated on the graph. b) Graph of observed vs. predicted data. Fit of best-fit model predictions to the data. FT: Fission Track; MTL: Mean Track Length; AHe: Apatite Helium; Obs: Observed; Pred: Predicted.

AB-17-13

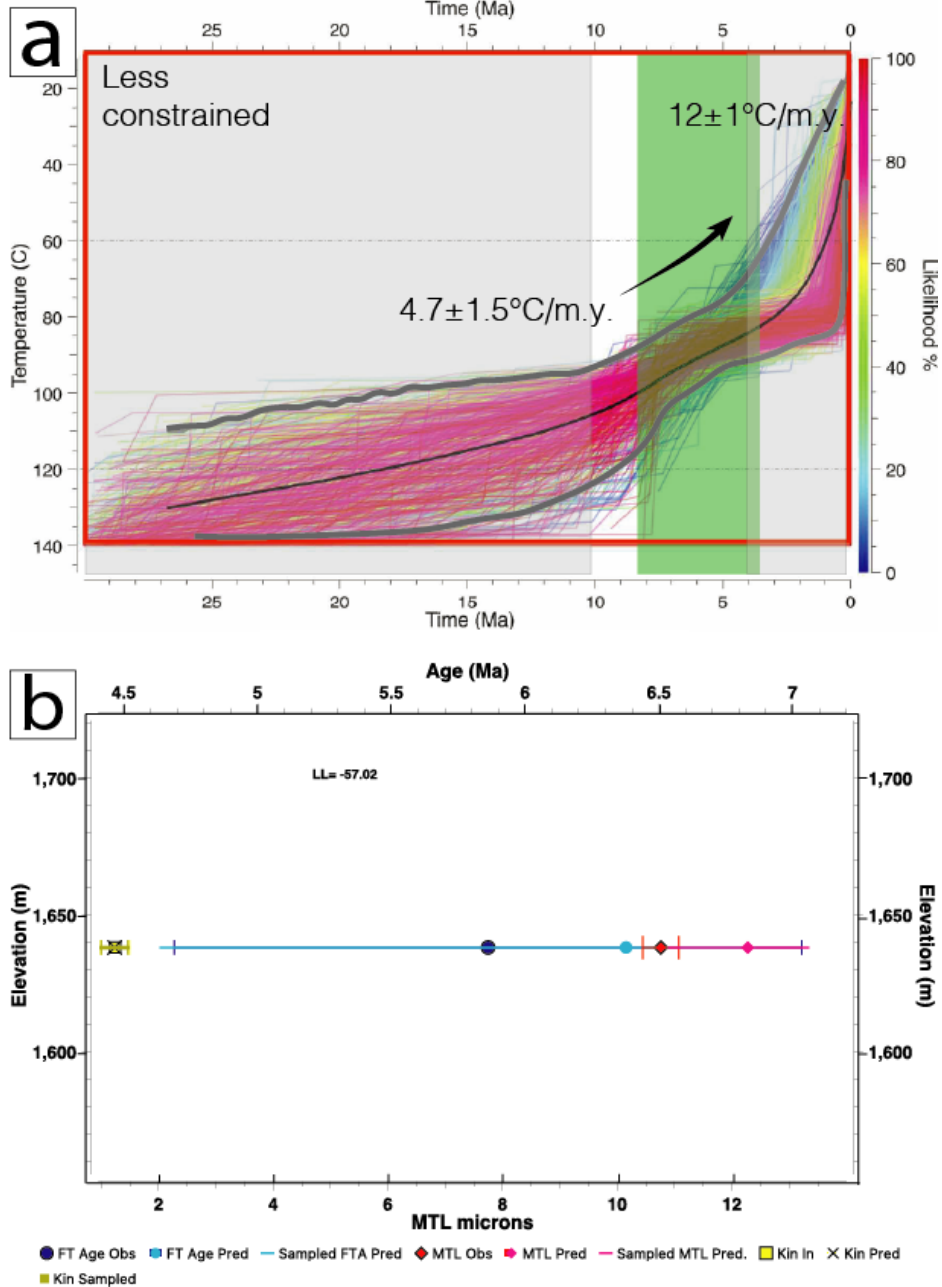


Figure S29. QTQt inversion results for the AB-17-13 sample. a) Time-temperature paths obtained by inversion of AFT data from the AB-17-13 sample using QTQt. The red square shows the explored time and temperature range for inversion. The colored lines show the T-t paths for the unique sample with its respective likelihood (see color scale on right). The solid grey lines show the expected model and its 95% reliable interval for the thermal histories of the sample. The green vertical band indicates the well-constrained acceleration of cooling at ~6 Ma. Cooling rates derived from QTQt are indicated on the graph. The apparent ~3–2 Ma cooling acceleration is a model bias and is not constrained by the data. b) Graph of observed vs. predicted data. Fit of best-fit model predictions to the data. FT: Fission Track; MTL: Mean Track Length; Obs: Observed; Pred: Predicted.

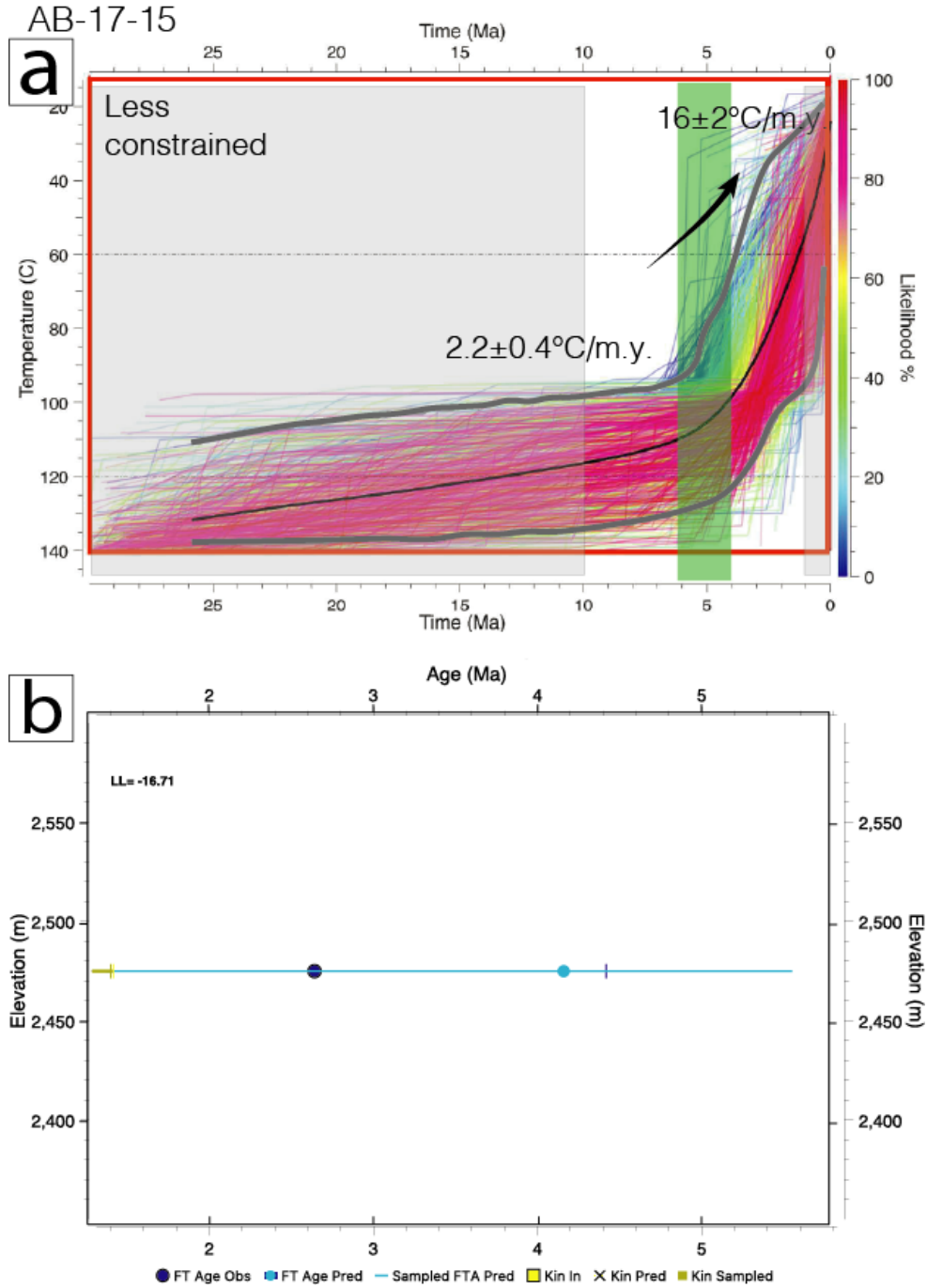


Figure S30. QTQt inversion results for the AB-17-15 sample. a) Time-temperature paths obtained by inversion of AFT data from the AB-17-15 sample using QTQt. The red square shows the explored time and temperature range for inversion. The colored lines show the T-t paths for the unique sample with its respective likelihood (see color scale on right). The solid grey lines show the expected model and its 95% reliable interval for the thermal histories of the sample. The green vertical band indicates the well-constrained acceleration of cooling at ~5 Ma. Cooling rates derived from QTQt are indicated on the graph. b) Graph of observed vs. predicted data. Fit of best-fit model predictions to the data. FT: Fission Track; Obs: Observed; Pred: Predicted.

AB-17-18

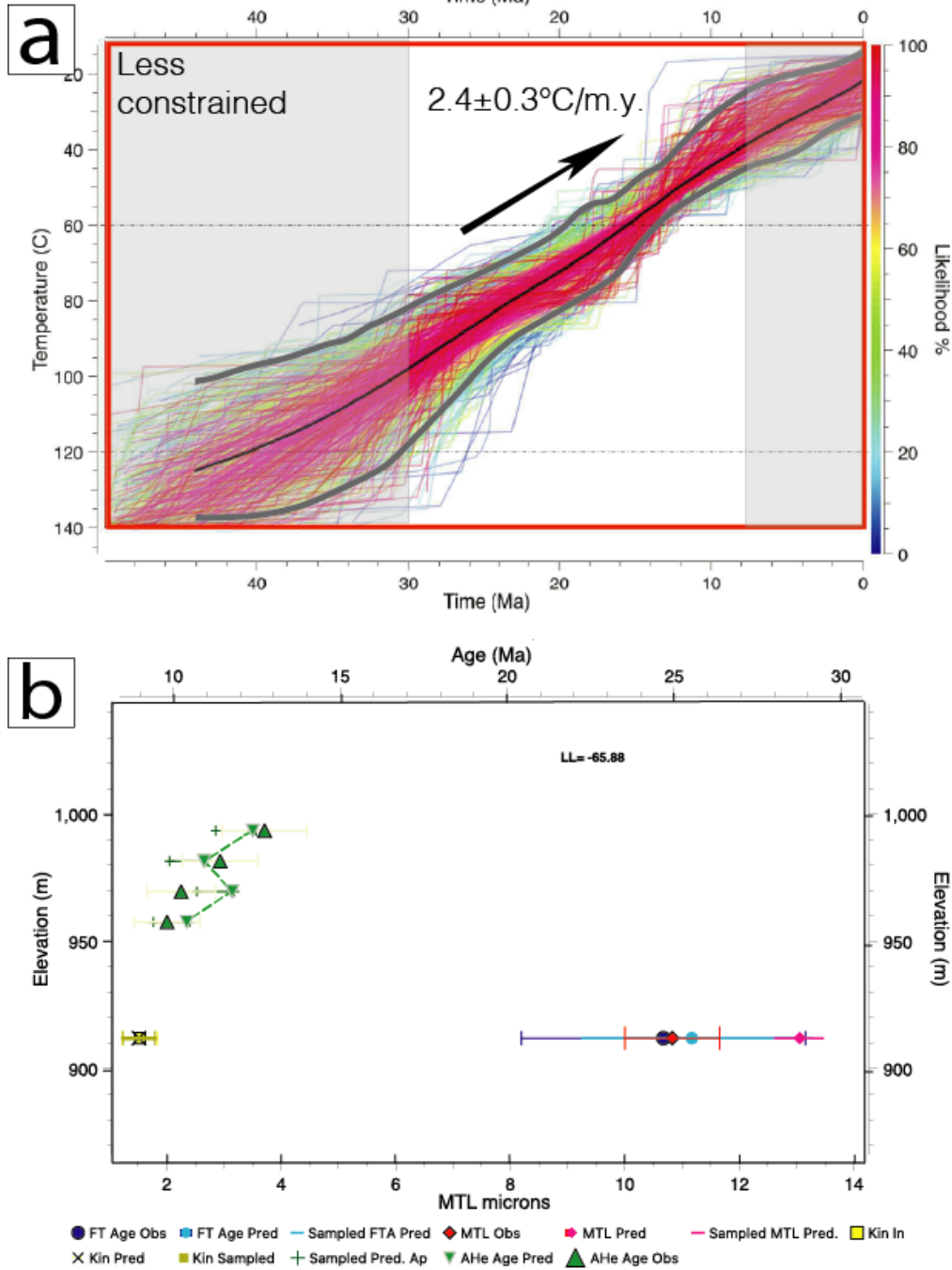


Figure S31. QTQt inversion results for the AB-17-18 sample. a) Time-temperature paths obtained by inversion of AHe and AFT data from the AB-17-18 sample using QTQt. The red square shows the explored time and temperature range for inversion. The colored lines show the T-t paths for the unique sample with its respective likelihood (see color scale on right). The solid grey lines show the expected model and its 95% reliable interval for the thermal histories of the sample. Cooling rate derived from QTQt is indicated on the graph. b) Graph of observed vs. predicted data. Fit of best-fit model predictions to the data. FT: Fission Track; MTL: Mean Track Length; AHe: Apatite Helium; Obs: Observed; Pred: Predicted.

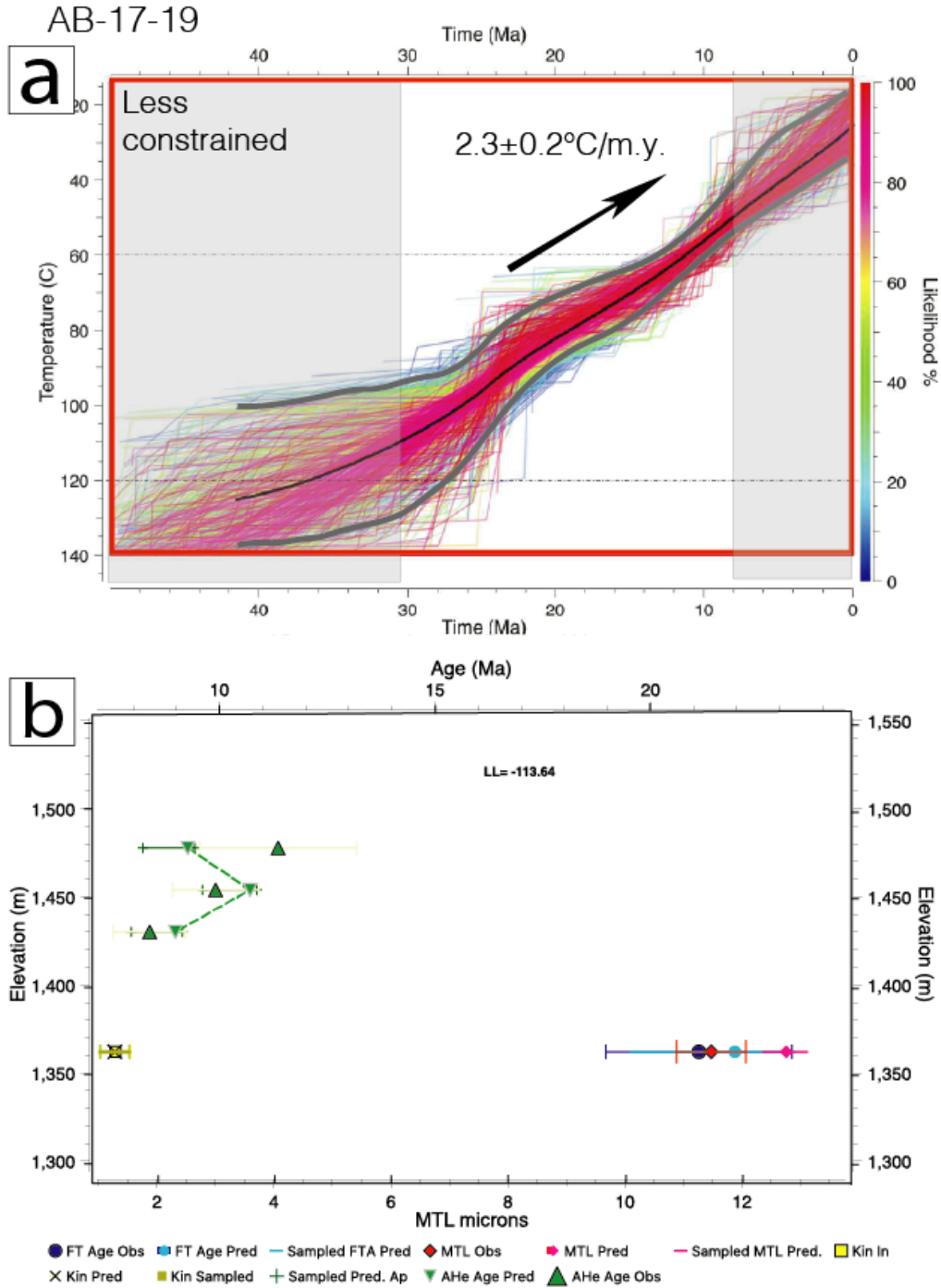


Figure S32. QTQt inversion results for the AB-17-19 sample. a) Time-temperature paths obtained by inversion of AHe and AFT data from the AB-17-19 sample using QTQt. The red square shows the explored time and temperature range for inversion. The colored lines show the T-t paths for the unique sample with its respective likelihood (see color scale on right). The solid grey lines show the expected model and its 95% reliable interval for the thermal histories of the sample. Cooling rate derived from QTQt is indicated on the graph. b) Graph of observed vs. predicted data. Fit of best-fit model predictions to the data. FT: Fission Track; MTL: Mean Track Length; AHe: Apatite Helium; Obs: Observed; Pred: Predicted.

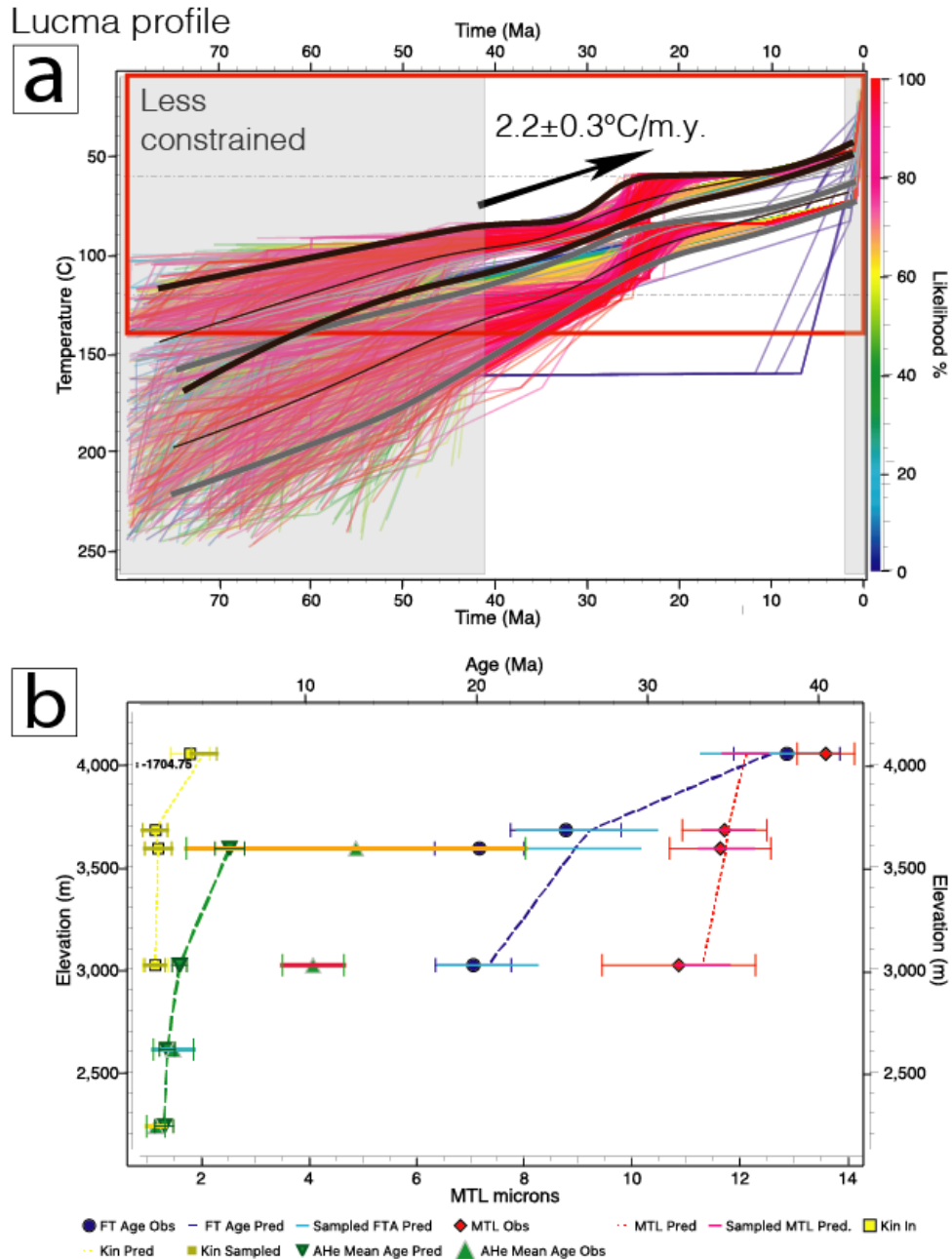


Figure S33. QTQt inversion results for the Lucma high-altitudinal profile. a) Time-temperature paths obtained by inversion of AHe and AFT thermochronology data from the Lucma age-elevation profile using QTQt (AB-17-21 to AB-17-28). The red square shows the explored time and temperature range for inversion. The colored lines show the T-t paths for the top and the bottom samples with their respective likelihood (see color scale on right). The solid black and grey lines show the expected model and its 95% reliable interval for the thermal histories of the top and bottom samples, respectively. The grey lines in between represent the expected cooling paths for the intermediate samples. Cooling rate derived from QTQt is indicated on the graph. b) Graph of observed vs. predicted data. Fit of best-fit model predictions to the data. FT: Fission Track; MTL: Mean Track Length; AHe: Apatite Helium; Obs: Observed; Pred: Predicted.

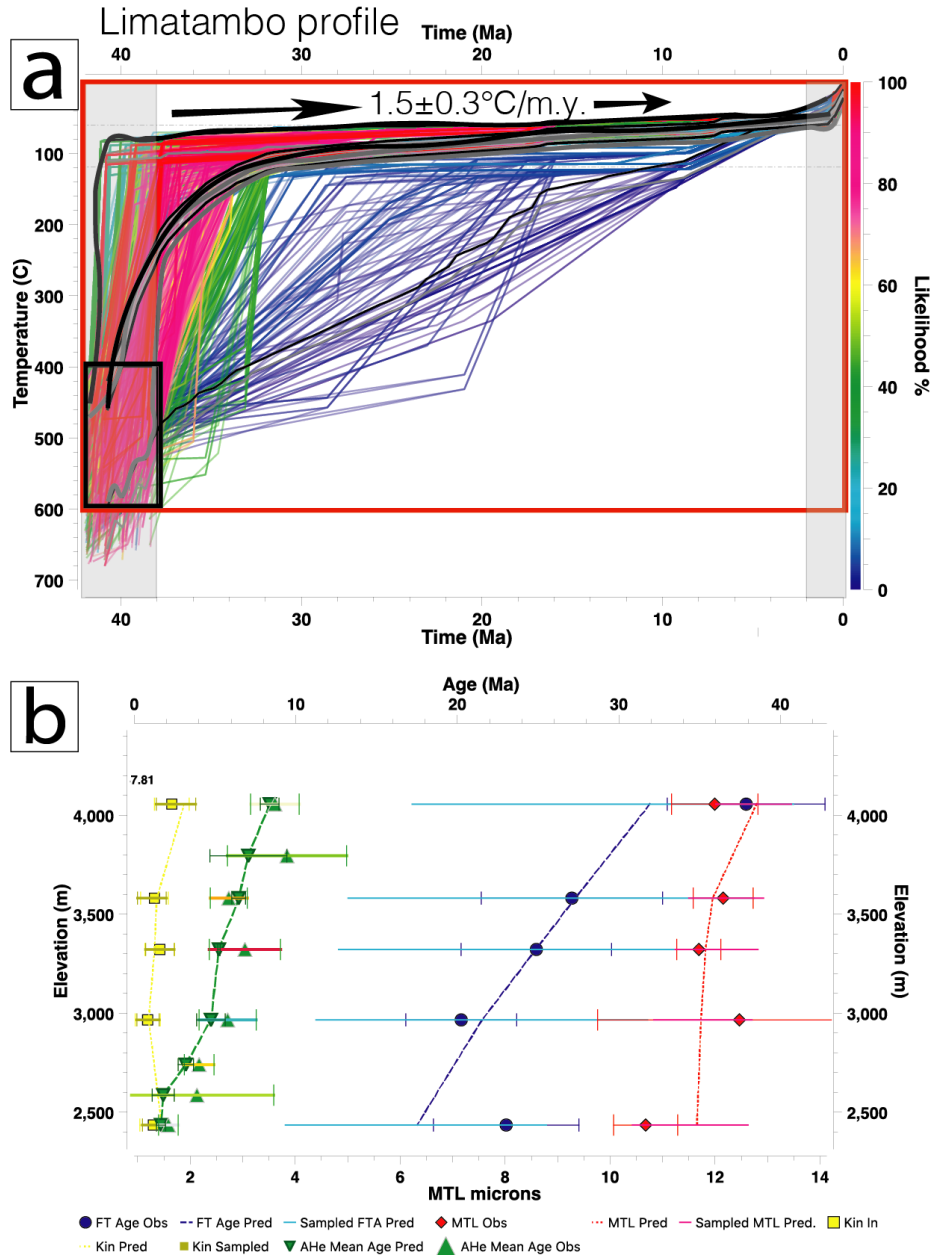


Figure S34. QTQt inversion results for the Limatambo high-altitudinal profile. a) Time-temperature paths obtained by inversion of AHe and AFT thermochronology data from the Limatambo age-elevation profile using QTQt (AB-17-29 to AB-17-36). The red square shows the explored time and temperature range for inversion. The black square corresponds to the pluton emplacement age and temperature constraints (Table S1). The colored lines show the T-t paths for the top and the bottom samples with their respective likelihood (see color scale on right). The solid black and grey lines show the expected model and its 95% reliable interval for the thermal histories of the top and bottom samples, respectively. The grey lines in between represent the expected cooling paths for the intermediate samples. Cooling rate derived from QTQt is indicated on the graph. b) Graph of observed vs. predicted data. Fit of best-fit model predictions to the data. FT: Fission Track; MTL: Mean Track Length; AHe: Apatite Helium; Obs: Observed; Pred: Predicted.

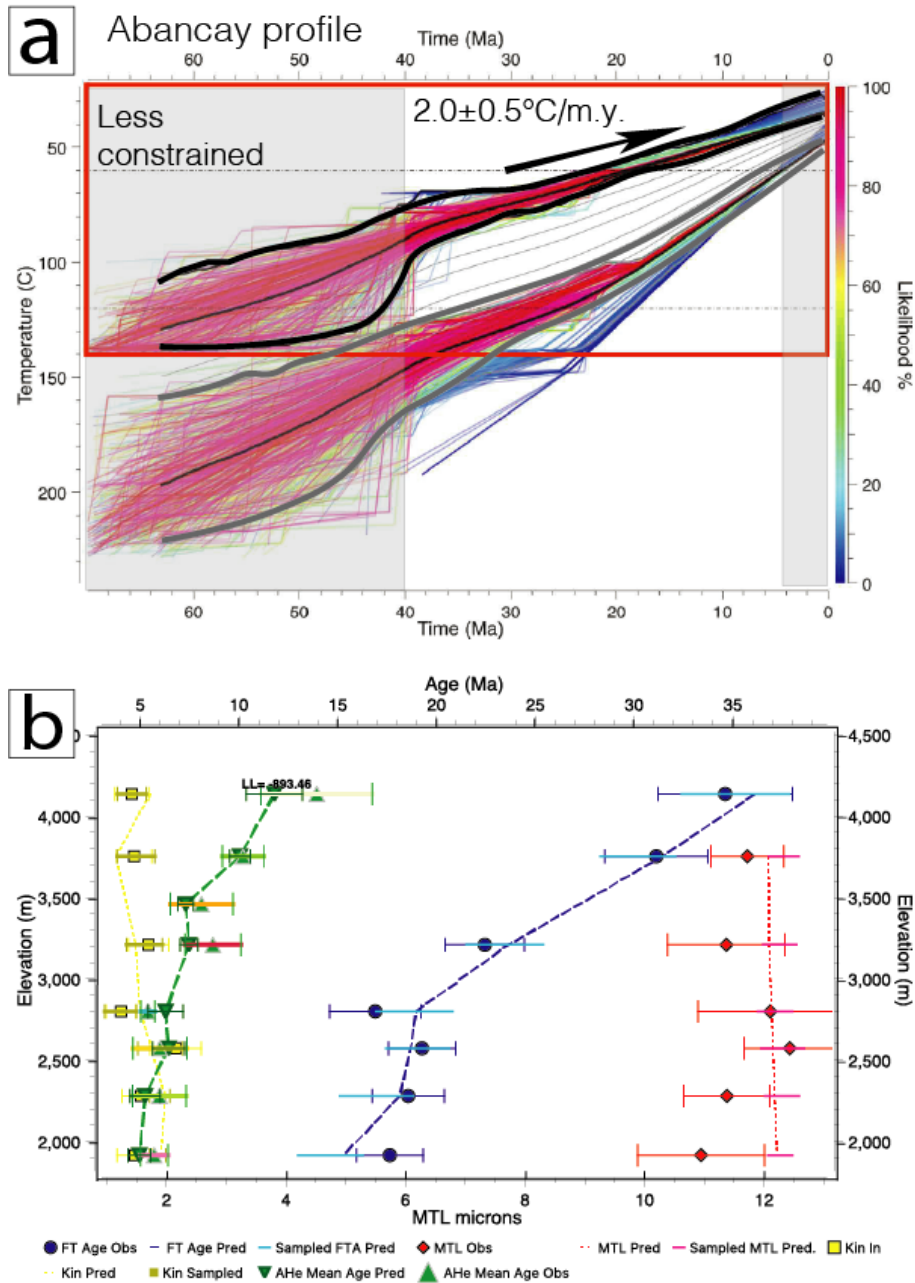


Figure S35. QTQt inversion results for the Abancay high-altitudinal profile. a) Time-temperature paths obtained by inversion of AHe and AFT thermochronology data from the Abancay age-elevation profile using QTQt (AB-17-37 to AB-17-44). The red square shows the explored time and temperature range for inversion. The colored lines show the T-t paths for the top and the bottom samples with their respective likelihood (see color scale on right). The solid black and grey lines show the expected model and its 95% reliable interval for the thermal histories of the top and bottom samples, respectively. The grey lines in between represent the expected cooling paths for the intermediate samples. Cooling rate derived from QTQt is indicated on the graph. b) Graph of observed vs. predicted data. Fit of best-fit model predictions to the data. FT: Fission Track; MTL: Mean Track Length; AHe: Apatite Helium; Obs: Observed; Pred: Predicted.

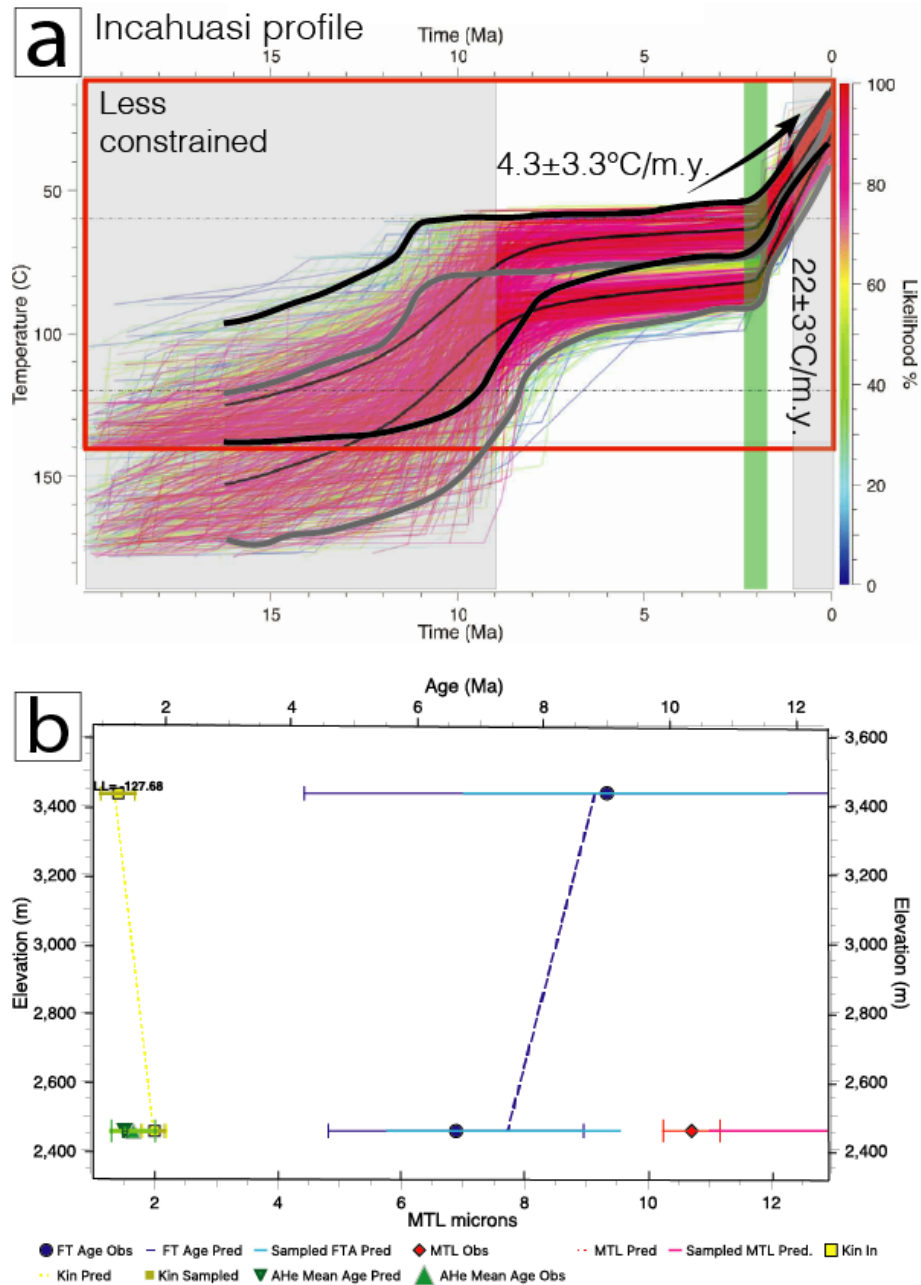


Figure S36. QTQt inversion results for the Incahuasi high-altitudinal profile. a) Time-temperature paths obtained by inversion of AHe and AFT thermochronology data from the Incahuasi age-elevation profile using QTQt (AB-17-51 and AB-17-55). The red square shows the explored time and temperature range for inversion. The colored lines show the T-t paths for the top and the bottom samples with their respective likelihood (see color scale on right). The solid black and grey lines show the expected model and its 95% reliable interval for the thermal histories of the top and bottom samples, respectively. The green vertical band indicates the well-constrained acceleration of cooling at ~2 Ma. Cooling rates derived from QTQt are indicated on the graph. b) Graph of observed vs. predicted data. Fit of best-fit model predictions to the data. FT: Fission Track; MTL: Mean Track Length; AHe: Apatite Helium; Obs: Observed; Pred: Predicted.

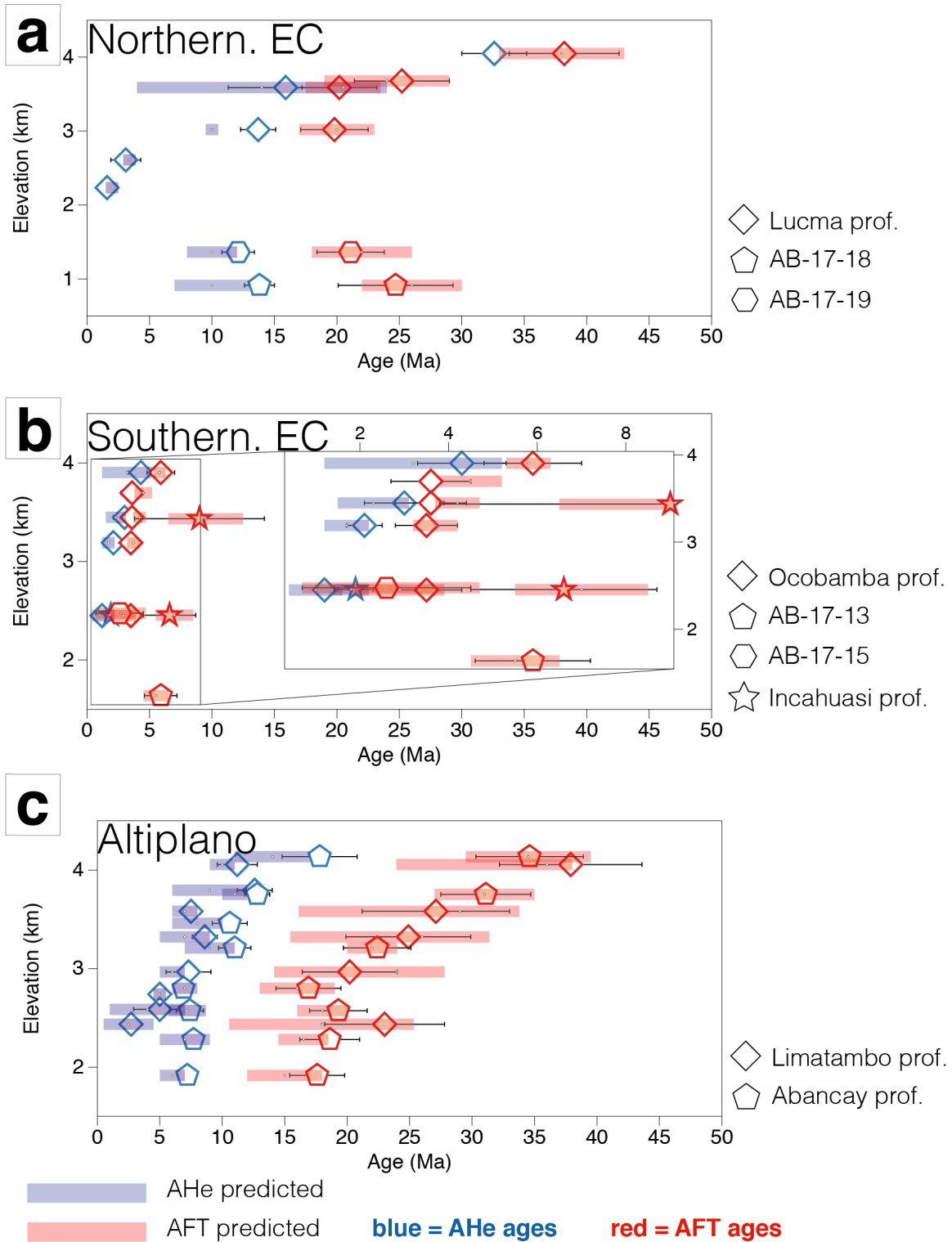


Figure S37. Observed vs. predicted thermochronological ages (AFT & AHe) modeled with QTQt. Panels a, b and c refer to the data associated to the northern Eastern Cordillera, the southern Eastern Cordillera and the Altiplano respectively (see Figure 4 for the location).

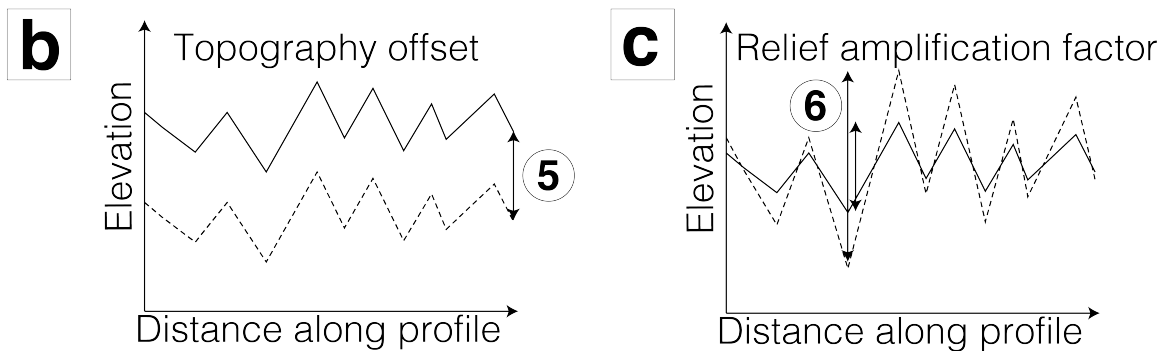
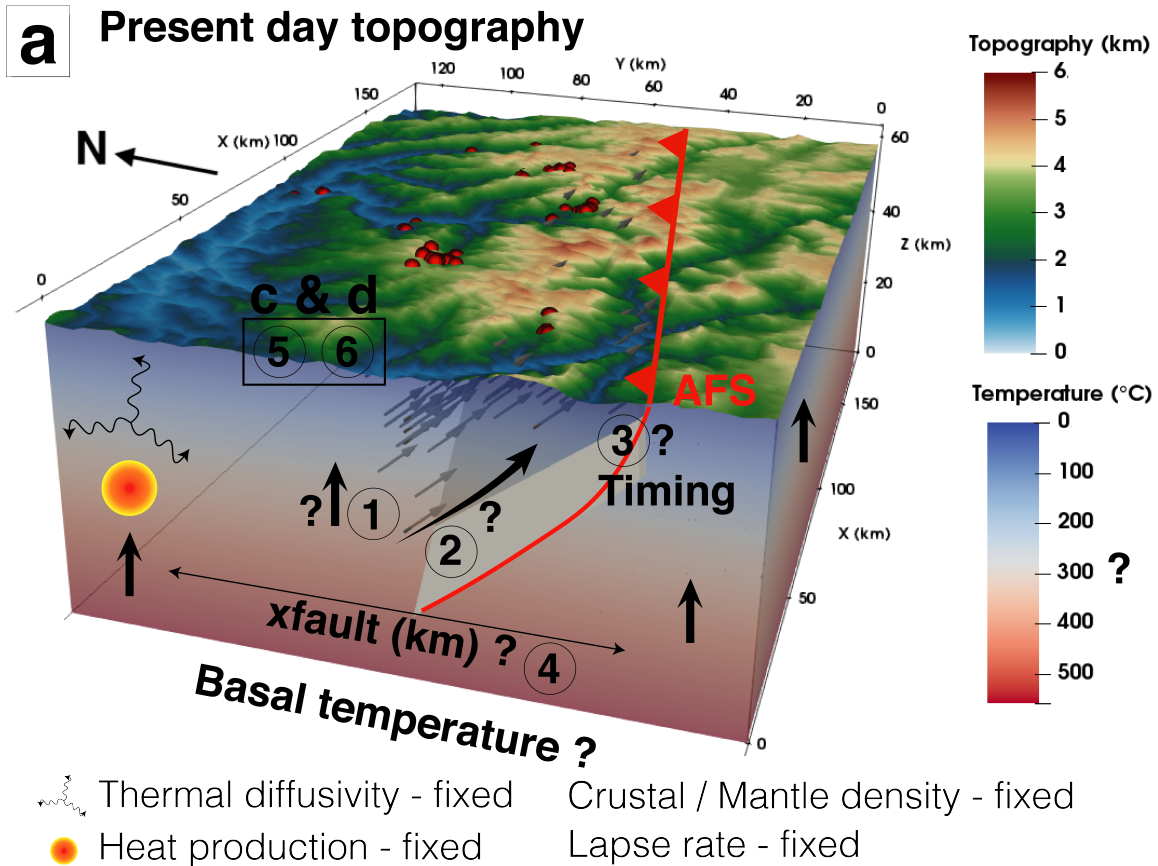
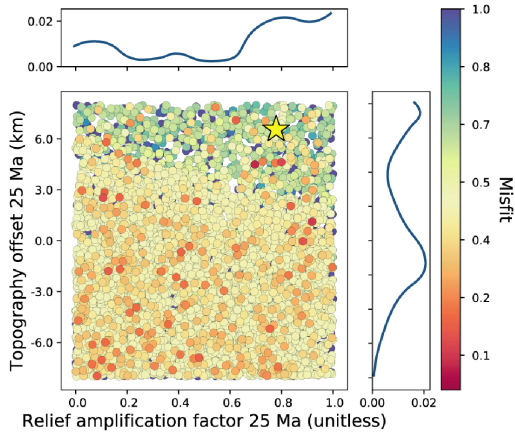
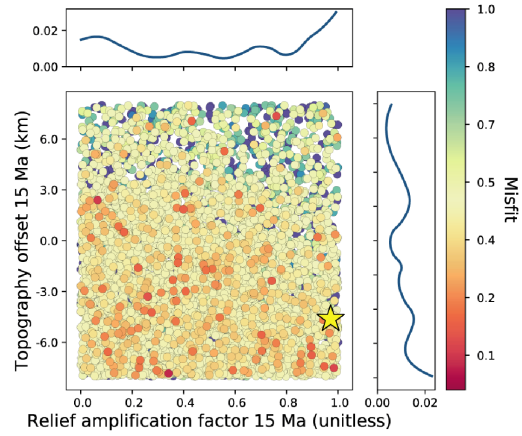


Figure S38. Parameters implemented and/or explored in Pecube through time. a) Example of the Eastern Cordillera crustal block (see Figure 2 for location). Red balls mark the location of the thermochronological data. Numbers and question marks refer to explored parameters. 1: Crustal block exhumation (km/Ma); 2: Fault velocity (km/Ma); 3: Timing of fault activation (Ma); 4: x fault (km), proxy for the fault geometry (fault dip). AFS: Apurimac fault system. b) Synthetic topographic profile presenting the topography-offset parameter evolution through time (5). c) Synthetic topographic profile presenting the relief amplification factor evolution through time (6).

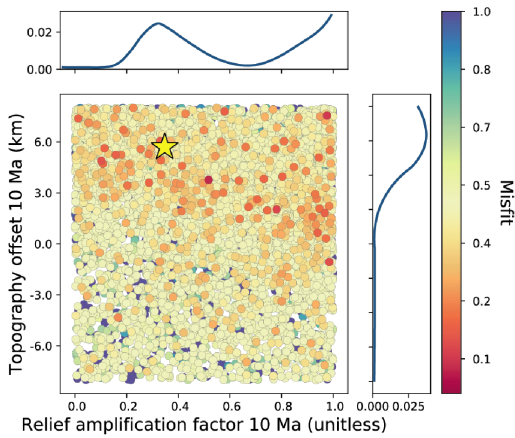
Altiplano 25 Ma



15 Ma



10 Ma



5 Ma

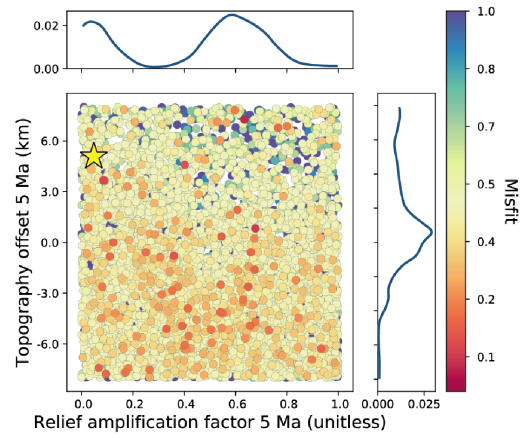
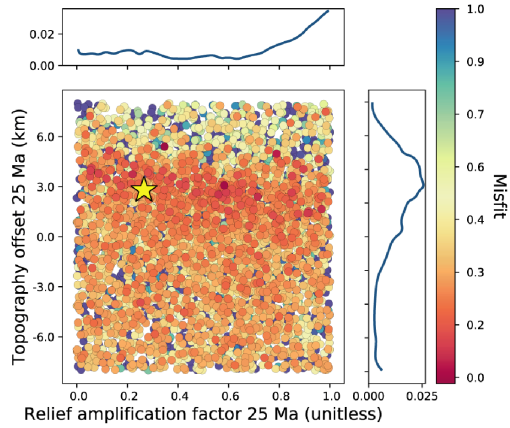
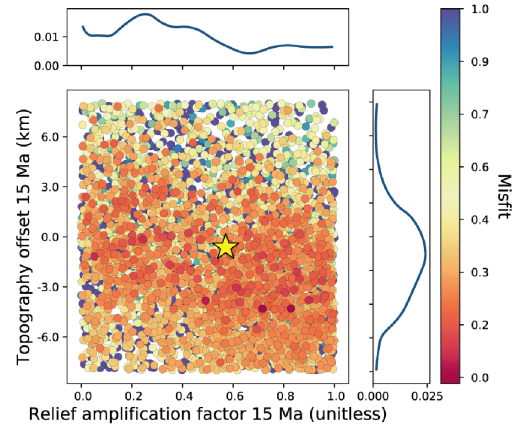


Figure S39. Pecube inversion results for landscape evolution parameters through time for the Altiplano block (performed using a 18°C/km geotherm). Y-axis is the topography-offset parameter; X-axis is the relief amplification factor. These outcomes correspond to a unique inversion with all the parameters free for each time period. These parameters do not converge toward a unique solution.

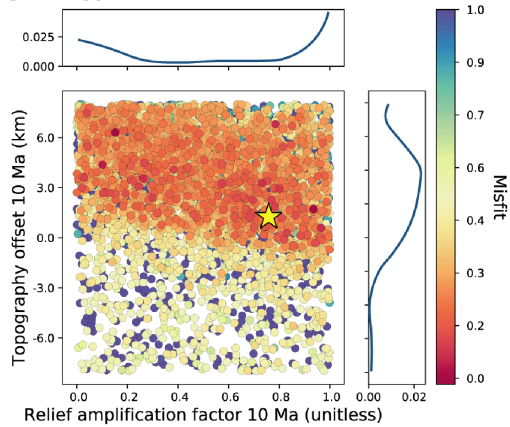
Eastern Cordillera 25 Ma



15 Ma



10 Ma



5 Ma

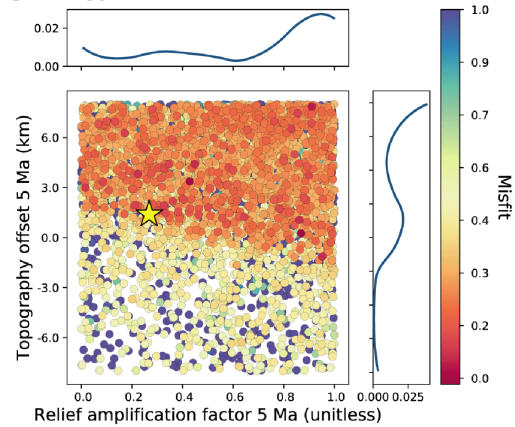


Figure S40. Pecube inversion results for landscape evolution parameters through time for the Eastern Cordillera block (performed using a 18°C/km geotherm). Y-axis is the topography-offset parameter; X-axis is the relief amplification factor. These outcomes correspond to a unique inversion with all the parameters free for each time period. These parameters do not clearly converge toward a unique solution.

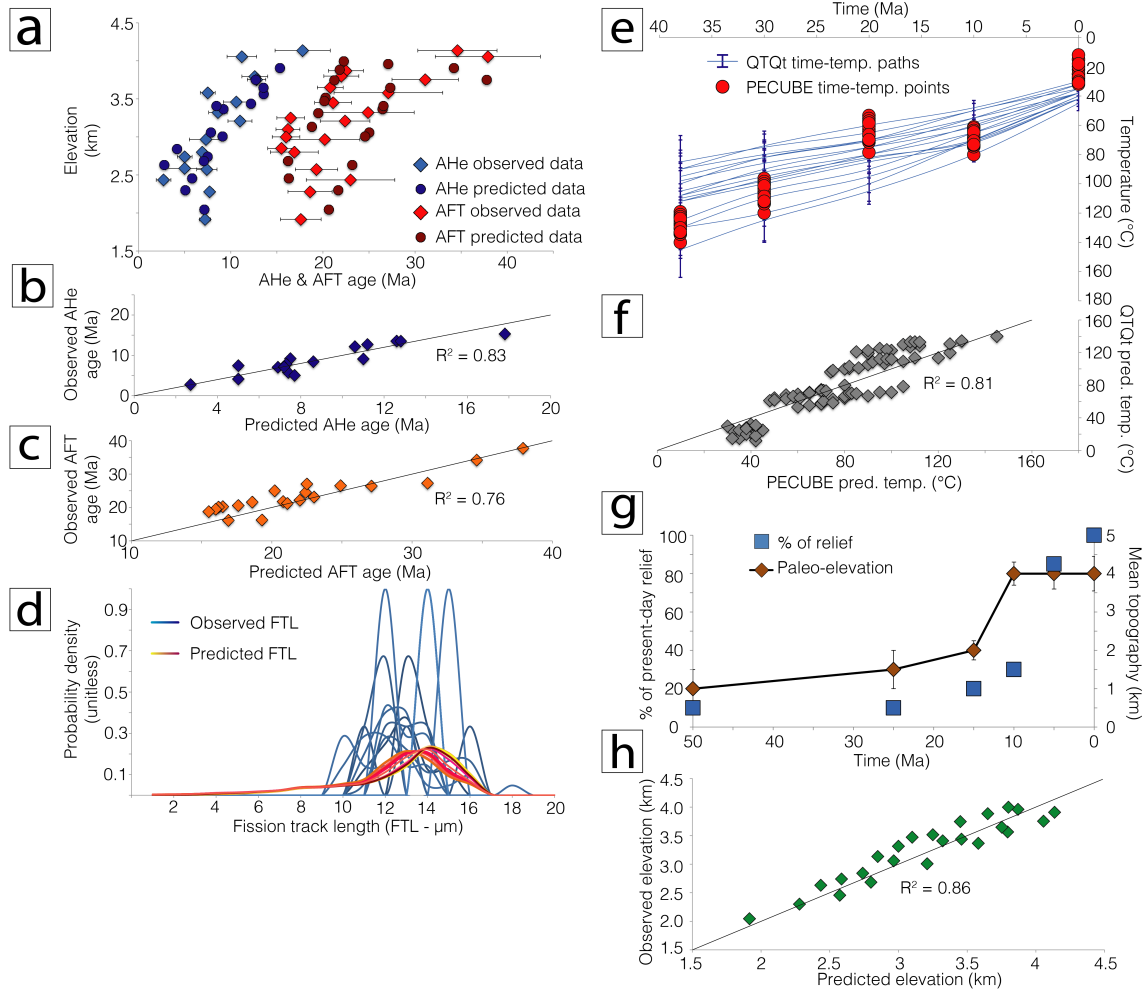


Figure S41. Observed data vs. predicted ones from Pecube best-fitting model for the Altiplano crustal block (performed using a 18°C/km geotherm). a) Age-elevation plot for observed AHe and AFT ages vs. predicted ones. b) Implemented AHe ages in function of predicted AHe ages. c) Implemented AFT ages in function of predicted AFT ages. d) Probability density function for implemented fission track length vs. predicted ones. e) Direct comparison of Time-temperature paths derived from QTQt modeling and T-t paths derived from Pecube. f) Implemented temperature (QTQt) in function of predicted ones computed with Pecube. g) Implemented modeled mean topography evolution (Sundell et al., 2019) and percentage of present-relief for forward modeling. h) Implemented topography (GTOPO30) in function of the predicted one by Pecube after landscape evolution computation. In any case, the data reproducibility is very satisfactory.

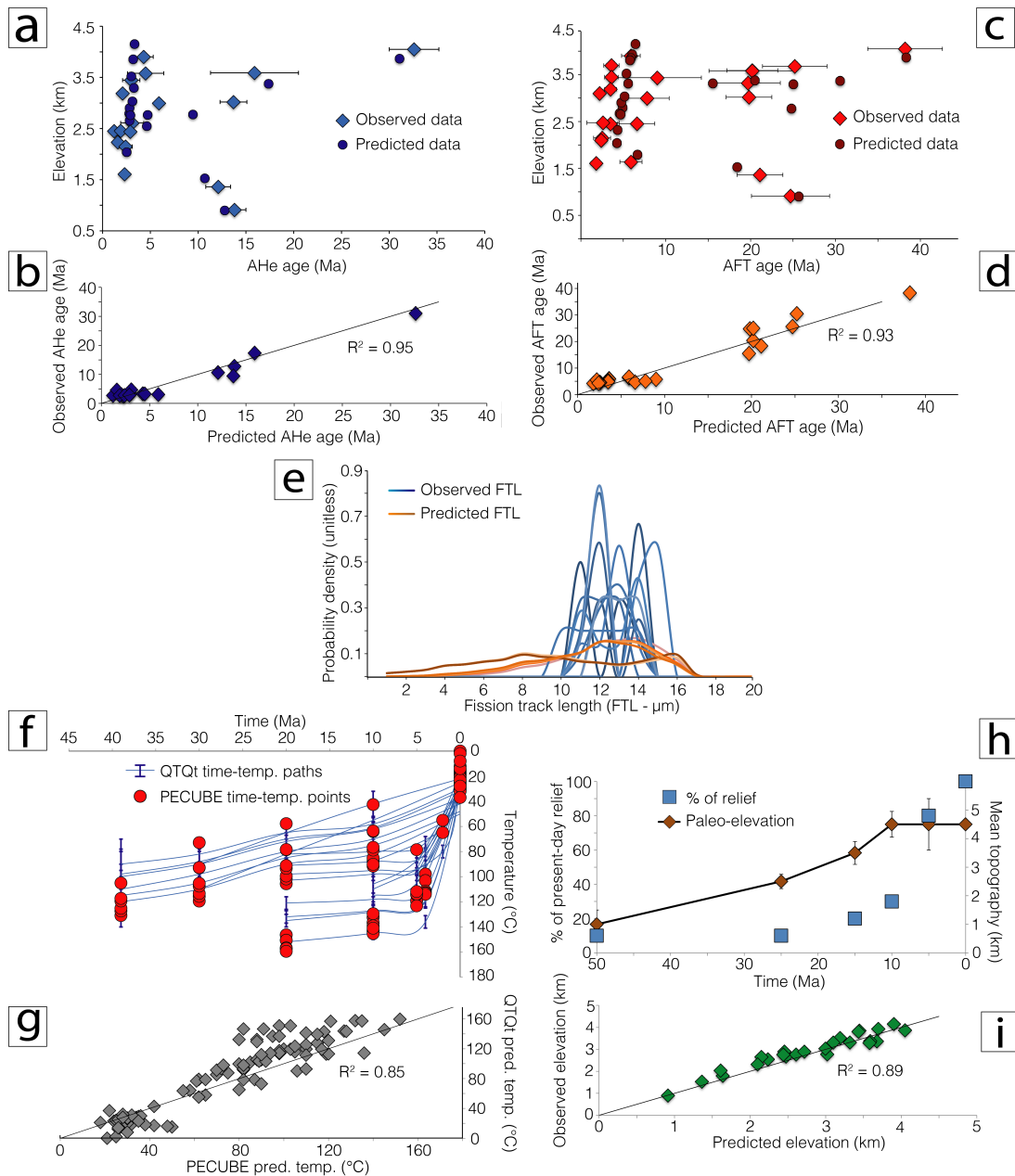


Figure S42. Observed data vs. predicted ones from Pecube best-fitting model for the Eastern Cordillera crustal block (performed using a 18°C/km geotherm). a) Age-elevation plot for observed AHe ages vs. predicted ones. b) Implemented AHe ages in function of predicted AHe ages. c) Age-elevation plot for observed AFT ages vs. predicted ones. d) Implemented AFT ages in function of predicted AFT ages. e) Probability density function for implemented fission track length vs. predicted ones. f) Direct comparison of Time-temperature paths derived from QTQt modeling and T-t paths derived from Pecube. g) Implemented temperature (QTQt) in function of predicted ones computed with Pecube. h) Implemented modeled mean topography evolution (Sundell et al., 2019) and percentage of present-relief for forward modeling. i) Implemented topography (GTOPO30) in function of the predicted one by Pecube after landscape evolution computation. In any case, the data reproducibility is very satisfactory.

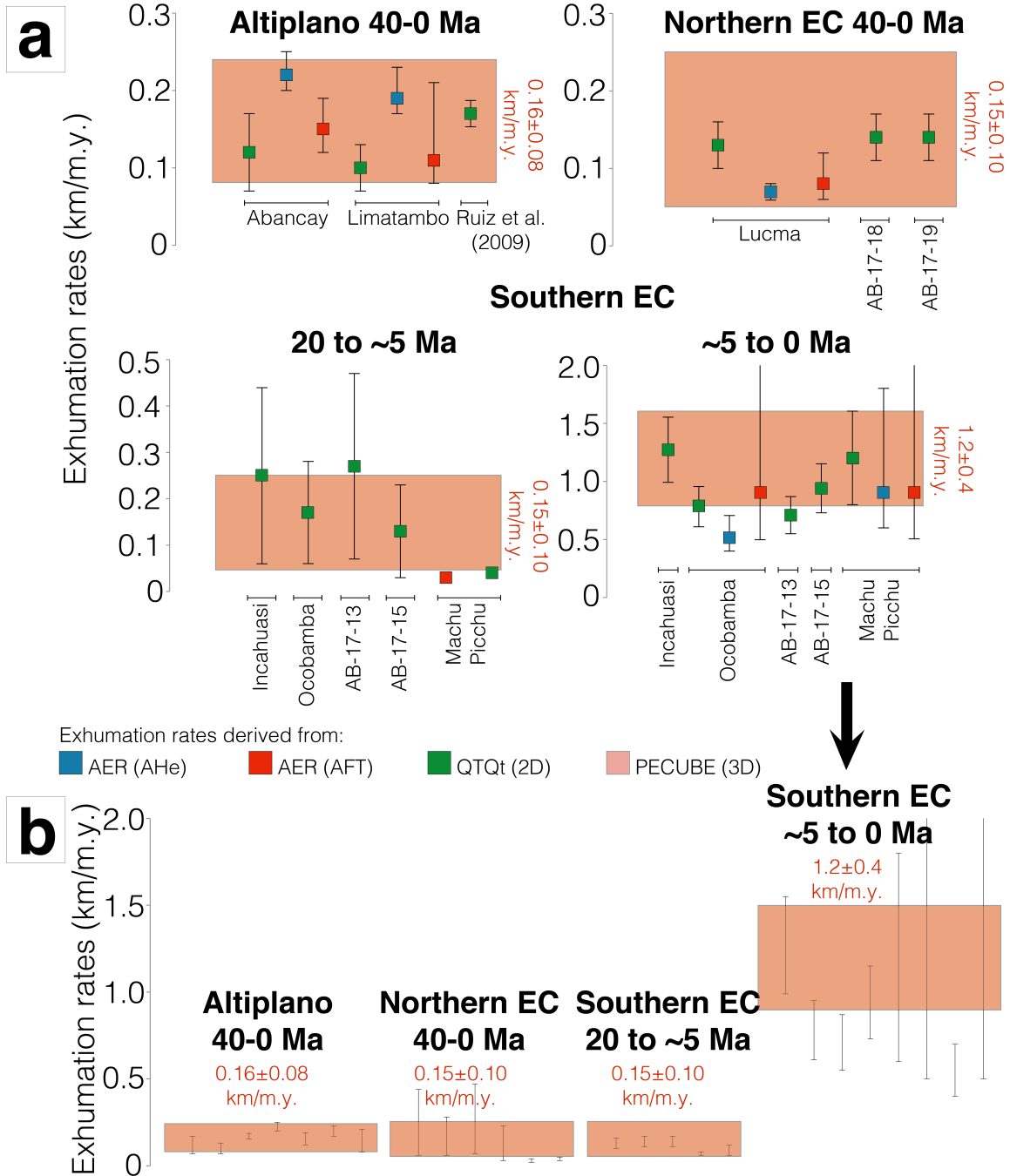


Figure S43. Exhumation rates derived from AER, QTQt and Pecube. a) Exhumation rate data per vertical profile and individual samples of the Abancay Deflection. b) Compilation of the data displayed in a.

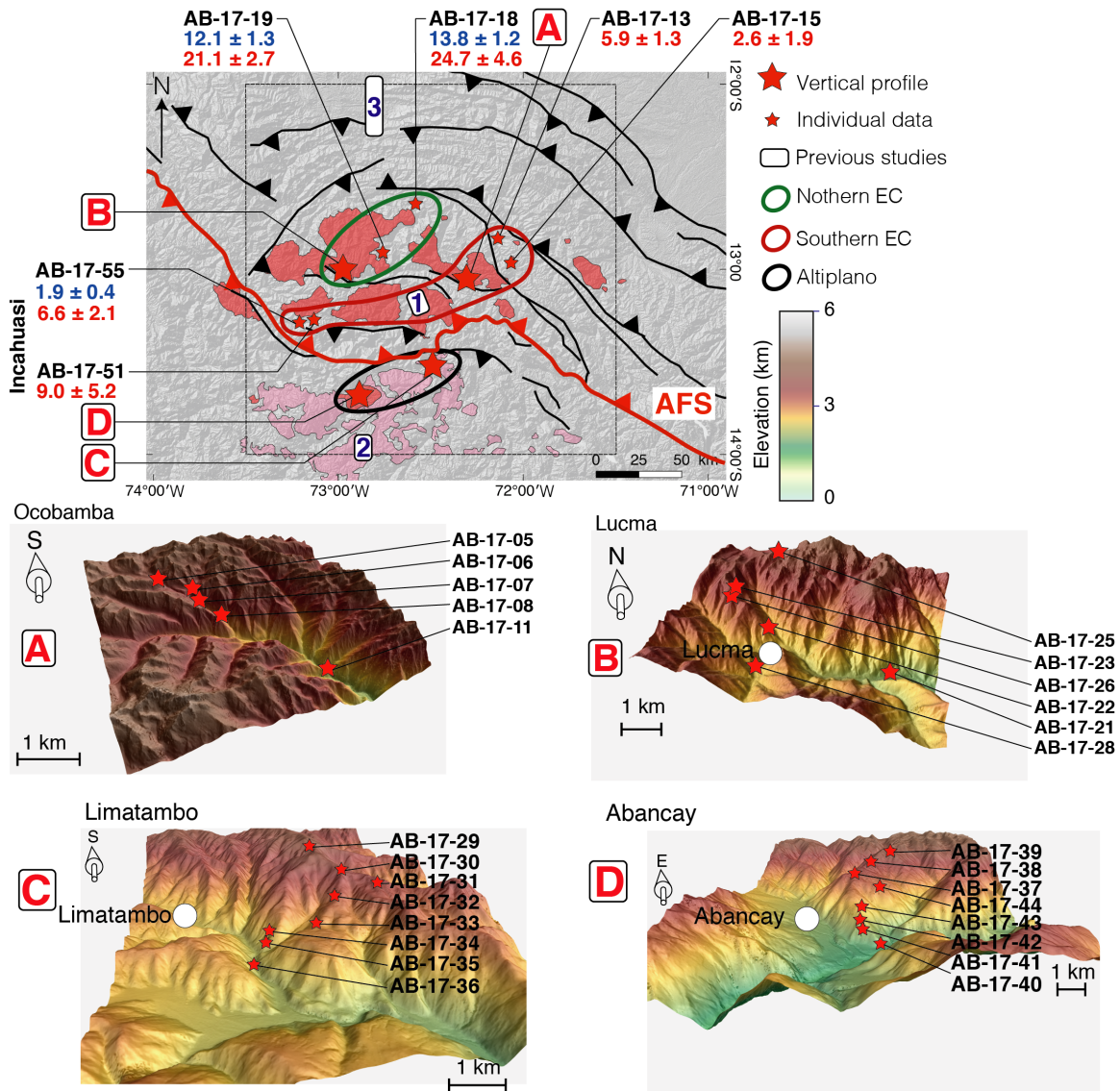


Figure S44. Sample locations within the Abancay Deflection. Red and pink polygons are respectively Permo-Triassic and Eocene plutons. Previous studies are: 1: Gérard et al. (in press) and Kennan (2008); 2: Ruiz et al. (2009); 3: Espurt et al. (2011) and Gautheron et al. (2013). Blue and red numbers below sample names refer to AHe mean ages and AFT central ages for individual samples and the two-sampled-point Incahuasi vertical profile. Red capital letters refer to the other sampled vertical profiles (A: Ocobamba profile; B: Lucma profile; C: Limatambo profile & D: Abancay profile). Green, red and black contours mark the latitudinal segmentation of the Abancay Deflection defining three areas according to thermal histories modeled with QTQt. The black dashed square frames the Abancay Deflection. AFT: Apurimac fault system; EC: Eastern Cordillera.

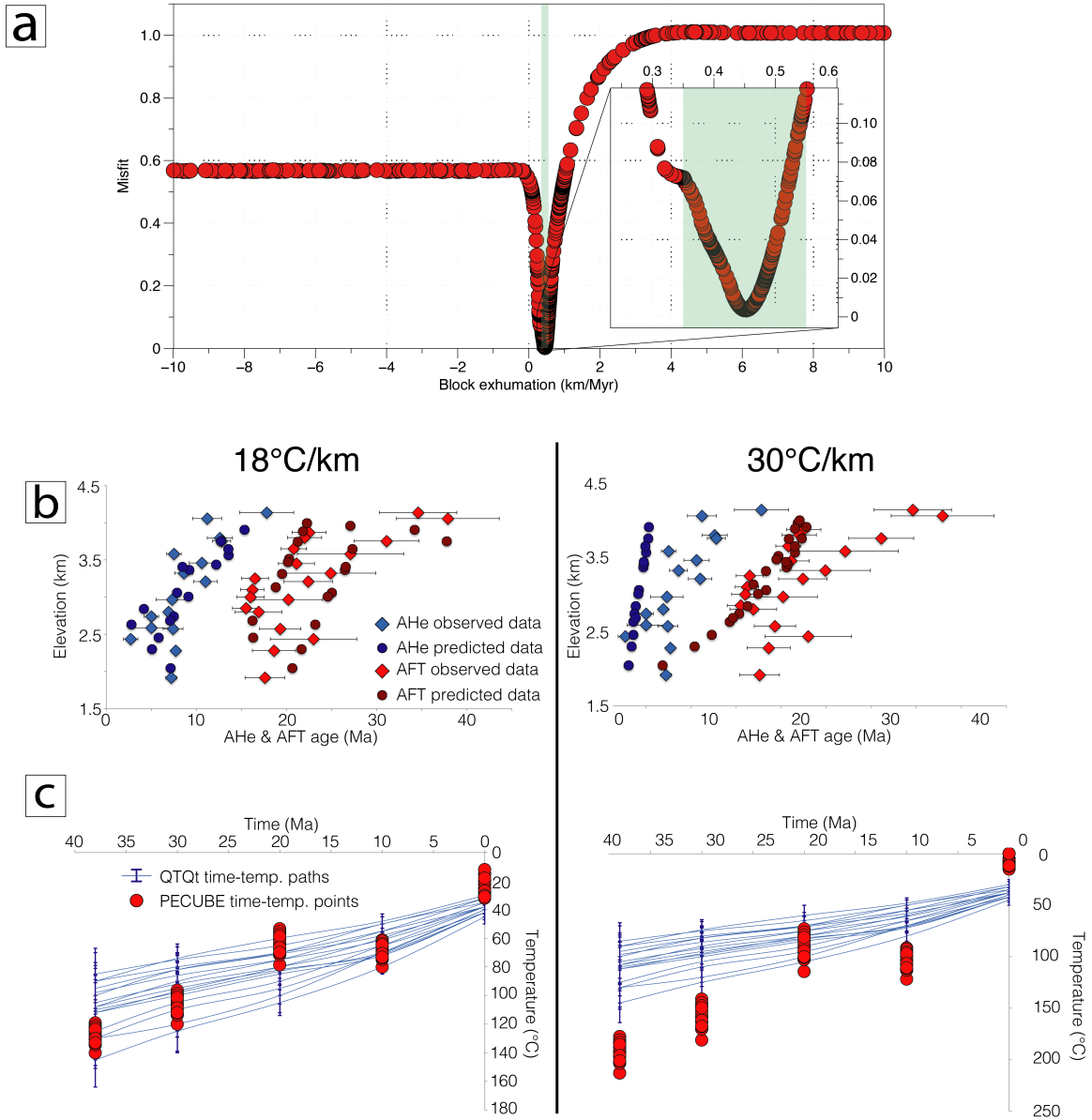


Figure S45. 3D Pecube inversion results for the Altiplano crustal block imposing a geothermal gradient of 30°C/km. The total sample size for inverse modeling is 1000. a) 1D parameter space and inversion results for crustal-block exhumation. Each point corresponds to one forward model. Lowest misfit value obtained corresponds to an exhumation rate of ~0.45 km/m.y. b and c) Observed data vs. predicted ones from Pecube best-fitting model for the Altiplano crustal block. A geothermal gradient of 18°C/km is imposed on left panels, while one of 30°C/km is implemented on right panels. b) Age-elevation plot for observed AHe and AFT ages vs. predicted ones. c) Direct comparison of time-temperature paths derived from QTQt and ones computed with Pecube best-fitting model. With a 30°C/km geothermal gradient, predicted ages are too young in most of cases for the Altiplano model.

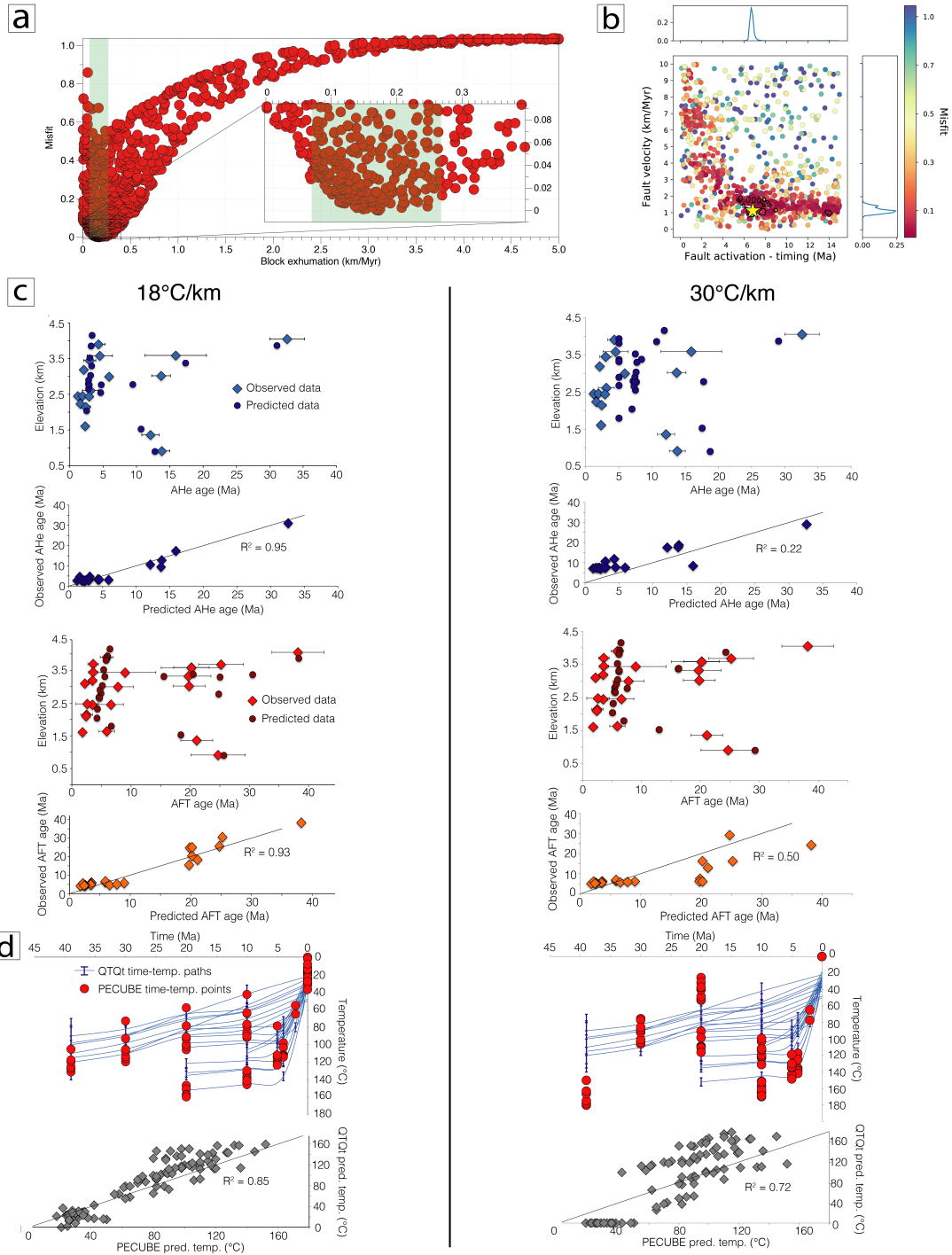


Figure S46. 3D Pecube inversion results for the Eastern Cordillera crustal block imposing a geothermal gradient of 30°C/km. The total sample size for inverse modeling is 1000. a) 1D parameter space and inversion results for crustal-block exhumation. Each point corresponds to one forward model. Lowest misfit value obtained corresponds to an exhumation rate of ~0.2 km/m.y. b) 2D parameter space and inversion results for the fault velocity vs. activation timing of the Apurimac fault system. Each colored point corresponds to one forward model. Blue curves (up and right subpanels) are the probability density for each parameter. The

yellow stars in panels a and b are the best-fitting model. Models converge for values of 7 ± 1 Ma for the fault activation timing and a fault velocity of 1.4 ± 0.4 km/m.y since that time. c and d) Observed data vs. predicted ones from Pecube best-fitting model for the Eastern Cordillera crustal block. A geothermal gradient of $18^\circ\text{C}/\text{km}$ is imposed on left panels, while one of $30^\circ\text{C}/\text{km}$ is implemented on right panels. c) Direct comparison of observed thermochronological data (AHe and AFT) with ones predicted with Pecube best-fitting model. d) Direct comparison of time-temperature paths derived from QTQt and ones computed with Pecube best-fitting model. With a $30^\circ\text{C}/\text{km}$ geothermal gradient, predicted ages are too old in most of cases for the Eastern Cordillera model.

Parameter	Value	Profile or individual data	Reference / Justification
Time explored (Ma)	0 - 20	Ocobamba	Time interval with the age range extended to twice the oldest thermochronological age obtained to avoid a modeling bias. Except for Limatambo; the time interval explored is framed by the batholith crystallization age (40 ± 2 Ma; Perello et al., 2003). For the Limatambo profile, we imposed in QTQt a temperature ranging from 400°C to 600°C (>> to the AHe and AFT closure temperature) between 42 and 38 m.y.
	0 - 30	AB-17-13	
	0 - 30	AB-17-15	
	0 - 50	AB-17-18	
	0 - 50	AB-17-19	
	0 - 80	Lucma	
	0 - 42	Limatambo	
	0 - 70	Abancay	
Explored temperature ($^\circ\text{C}$)	0 - 140	All except Limatambo	Closure temperature for AHe and AFT systems (Ault et al., 2019). For Limatambo: temperature for pluton emplacement.
	0 - 600	Limatambo	
Explored $\delta T/\delta t$ ($^\circ\text{C}/\text{My}$)	1000	All	Maximum exploration – no constrains
Geothermal gradient ($^\circ\text{C}/\text{km}$)	25 ± 15	All excepted individual data (AB-17-xx)	Geothermal exploration for common values in orogens. This range includes our computed gradient for the Abancay Deflection region ($18 \pm 4^\circ\text{C}/\text{km}$) and accepted values for the Eastern Cordillera further south in Bolivia ($26 \pm 8^\circ\text{C}/\text{km}$; Barnes et al., 2008).
Present-day temperature ($^\circ\text{C}$)	25 ± 10	All	N.A.*
Lapse rate ($^\circ\text{C}/\text{km}$)	6 ± 2	All	Estimated from Gonfiantini et al. (2001) and Klein et al. (1999).
Allow the geothermal gradient to vary over time	Yes	All	N.A.*
Reheating	No	All	No evidence for reheating (burial) of the samples.
Number of iteration	Prior = 100000 Post = 200000	All	N.A.*
Etchant	5.5 M	All	Analytical protocol
Annealing model (AFT)	N.A.*	All	Ketcham et al. (2007)
Radiation damage model (AHe)	N.A.*	All	Gautheron et al. (2009)

Note:

*N.A. = not applicable.

Table S1. QTQt parameters for thermochronological data modeling

Sample number	Arithmetic mean age (Ma)	Error - Standard deviation (Ma)
<u>Ocobamba profile</u>		
AB-17-05	4.3	1.0
AB-17-07	3.0	0.9
AB-17-08	2.1	0.4
AB-17-11	1.2	0.2
<u>Punctual data</u>		
AB-17-18	13.8	1.2
AB-17-19	12.1	1.3
<u>Lucma profile</u>		
AB-17-21	1.6	0.4
AB-17-22	13.7	1.4
AB-17-25	32.6	2.6
AB-17-26	15.9	4.6
AB-17-28	3.1	1.2
<u>Limatambo profile</u>		
AB-17-29	11.2	1.6
AB-17-30	12.6	1.4
AB-17-31	7.5	0.8
AB-17-32	8.6	1.0
AB-17-33	7.3	1.8
AB-17-34	5.0	0.8
AB-17-35	5.0	2.1
AB-17-36	2.7	0.8
<u>Abancay profile</u>		
AB-17-37	6.9	0.4
AB-17-38	7.4	1.1
AB-17-39	7.7	0.3
AB-17-40	7.2	0.6
AB-17-41	17.8	3.0
AB-17-42	12.8	1.0
AB-17-43	10.6	1.4
AB-17-44	11.0	1.3
<u>Incahuasi profile</u>		
AB-17-55	1.9	0.4

Table S2. Apatite (U-Th-Sm)/He data – Mean ages and errors for Pecube modeling

Parameter	Value	Reference
Crustal density (kg/m ³)	2721 ±65	Arndt et al. (1997) ; Waples and Waples (2004)
Mantle density (kg/m ³)	3095 ±147	Waples and Waples (2004)
Lapse rate (°C/km)	6 ±1	Klein et al. (1999) ; Gonfiantini et al. (2001)
Heat flow (mW/m ²)	57 ±5	Henry and Pollack (1988) ; Davies (2013)
Thermal conductivity (W/m/°C)	2.8 ±0.2	Henry and Pollack (1988)
Geothermal gradient (°C/km)	18 ±4	This study
Heat production (mean for the crust; μW/m ³)	0.9	Springer (1999)
Specific thermal capacity (J/kg/K)	900 ±200	Arndt et al. (1997); Waples and Waples (2004)
Thermal diffusivity (km ² /Ma)	40 ±11	Arndt et al. (1997); Whittington et al. (2009)
Heat production through time (°C/Ma)	6	This study
Base model temperature (°C)	560	This study
Crust thickness (Moho depth; km)	56 ±7	Mcglashan et al. (2008); Lloyd et al. (2010) Assumpção et al. (2013); Chulick et al. (2013); Ma and Clayton (2014); Bishop et al. (2017)
Elastic thickness (km)	17.5 ±2.5	Pérez-Gussinyé et al. (2008)
Young modulus (Pa)	1.10 ¹¹	Standard value
Poisson's coefficient (unitless)	0.25	Standard value

Note: Displayed results and errors were computed from the literature (Arithmetic mean and standard deviation). Pecube does not take into account these parameter values dispersion. Implemented values into Pecube are in bold.

Table S3. Thermal and rheological parameters for Pecube modeling.

Parameter	Range
<u>Altiplano model</u>	
Crustal block exhumation (km/m.y.)	0 – 5
Basal temperature - 56 km depth (°C)	400 – 800 (13°C/km – 26°C/km)
<u>Eastern Cordillera model</u>	
Crustal block exhumation (km/m.y.)	0 - 2
x fault – 25 km depth – proxy for fault dip (km)	-50 (26°) – 0 (vertical – 90°)
Fault velocity (km/m.y.)	0 – 5
Timing for fault activation (Ma)	0 – 10
<u>Common parameters explored for the Altiplano and the Eastern Cordillera</u>	
<u>Topography offset (km)</u>	
At 25 Ma	-6 – 6
At 15 Ma	-6 – 6
At 10 Ma	-6 – 6
At 5 Ma	-6 – 6
<u>Relief amplification factor (unitless)</u>	
At 25 Ma	0 – 1
At 15 Ma	0 – 1
At 10 Ma	0 – 1
At 5 Ma	0 – 1

Note: Pecube inversions were performed processing 12 successive iterations. The sample size for the first iteration is 984 and 480 for all other iterations. The number of resample cells is 288 (for n iteration) meaning a 60 % resampling of the previous best-fitting models (from n-1 iteration). The total sample size for inverse modeling is 6744 (Figures 8a, 9a and 9b).

Table S4. Explored parameters and ranges for thermochronological data inversion (Pec modeling)

References

- Arndt, J., Bartel, T., Scheuber, E., & Schilling, F. (1997). Thermal and rheological properties of granodioritic rocks from the Central Andes, North Chile. *Tectonophysics*, 271(1–2), 75–88. [https://doi.org/10.1016/S0040-1951\(96\)00218-1](https://doi.org/10.1016/S0040-1951(96)00218-1)
- Assumpção, M., Feng, M., Tassara, A., & Julià, J. (2013). Models of crustal thickness for South America from seismic refraction, receiver functions and surface wave tomography. *Tectonophysics*. Elsevier B.V. <https://doi.org/10.1016/j.tecto.2012.11.014>
- Ault, A. K., Gautheron, C., & King, G. E. (2019). Innovations in (U-Th)/He, fission-track, and trapped-charge thermochronometry with applications to earthquakes, weathering, surface-mantle connections, and the growth and decay of mountains. *Tectonics*. <https://doi.org/10.1029/2018tc005312>
- Barnes, J. B., Ehlers, T. A., McQuarrie, N., O'Sullivan, P. B., & Tawackoli, S. (2008). Thermochronometer record of central Andean Plateau growth, Bolivia (19.5°S). *Tectonics*, 27(3). <https://doi.org/10.1029/2007TC002174>
- Bishop, B. T., Beck, S. L., Zandt, G., Wagner, L., Long, M., Antonijevic, S. K., et al. (2017). Causes and consequences of flat-slab subduction in southern Peru. *Geosphere*, 13(5), 1392–1407. <https://doi.org/10.1130/GES01440.1>
- Braun, J. (2003). Pecube: A new finite-element code to solve the 3D heat transport equation including the effects of a time-varying, finite amplitude surface topography. *Computers and Geosciences*, 29(6), 787–794. [https://doi.org/10.1016/S0098-3004\(03\)00052-9](https://doi.org/10.1016/S0098-3004(03)00052-9)
- Braun, J., van der Beek, P., & Batt, G. (2006). *Quantitative Thermochronology: Numerical Methods for the Interpretation of Thermochronological Data*. Cambridge: Cambridge Univ. Press.
- Braun, J., van der Beek, P., Valla, P., Robert, X., Herman, F., Glotzbach, C., et al. (2012). Quantifying rates of landscape evolution and tectonic processes by thermochronology and numerical modeling of crustal heat transport using PECUBE. *Tectonophysics*, 524–525, 1–28. <https://doi.org/10.1016/j.tecto.2011.12.035>
- Chulick, G. S., Detweiler, S., & Mooney, W. D. (2013). Seismic structure of the crust and uppermost mantle of South America and surrounding oceanic basins. *Journal of South American Earth Sciences*. Elsevier Ltd. <https://doi.org/10.1016/j.jsames.2012.06.002>
- Davies, J. H. (2013). Global map of solid Earth surface heat flow. *Geochemistry, Geophysics, Geosystems*, 14(10), 4608–4622. <https://doi.org/10.1002/ggge.20271>
- Espurt, N., Barbarand, J., Roddaz, M., Brusset, S., Baby, P., Saillard, M., & Hermoza, W. (2011). A scenario for late Neogene Andean shortening transfer in the Camisea Subandean zone (Peru, 12°S): Implications for growth of the northern Andean Plateau. *Bulletin of the Geological Society of America*, 123(9–10), 2050–2068. <https://doi.org/10.1130/B30165.1>
- Gallagher, K. (2012). Transdimensional inverse thermal history modeling for quantitative thermochronology. *Journal of Geophysical Research: Solid Earth*, 117(2), 1–16. <https://doi.org/10.1029/2011JB008825>
- Gautheron, C., Tassan-Got, L., Barbarand, J., & Pagel, M. (2009). Effect of alpha-damage annealing on apatite (U-Th)/He thermochronology. *Chemical Geology*,

- 266(3–4), 166–179. <https://doi.org/10.1016/j.chemgeo.2009.06.001>
- Gautheron, C., Espurt, N., Barbarand, J., Roddaz, M., Baby, P., Brusset, S., et al. (2013). Direct dating of thick- and thin-skin thrusts in the Peruvian Subandean zone through apatite (U-Th)/He and fission track thermochronometry. *Basin Research*, 25(4), 419–435. <https://doi.org/10.1111/bre.12012>
- Gérard, B., Audin, L., Robert, X., Gautheron, C., van der Beek, P., Bernet, M., et al. (2021). Pliocene river capture and incision of the northern Altiplano: Machu Picchu, Peru. *Journal of the Geological Society*.
- Gonfiantini, R., Roche, M.-A., Olivry, J.-C., Fontes, J.-C., & Zuppi, G. M. (2001). The altitude effect on the isotopic composition of tropical rains. *Chemical Geology*, (181), 147–167.
- van Heiningen, P. S., Carlotto, V., Zuloaga, A. D., Romero, L., & Andriessen, P. A. M. (2005). Oligocene to Pleistocene exhumation patterns across the Apurimac River drainage basin, southern Peru. *6th International Symposium on Andean Geodynamics (ISAG 2005, Barcelona)*, 763–766.
- Henry, S. G., & Pollack, H. N. (1988). Terrestrial heat flow above the Andean Subduction Zone in Bolivia and Peru. *Journal of Geophysical Research: Solid Earth*, 93(B12), 15153–15162. <https://doi.org/10.1029/jb093ib12p15153>
- Kennan, L. (2008). Fission track ages and sedimentary provenance studies in Peru, and their implications for andean paleogeographic evolution, stratigraphy and hydrocarbon systems. In *VI INGEPET, 13–17 October 2008* (p. 13). Lima, Peru. Retrieved from <http://www.agu.org/pubs/crossref/1988/JB093iB12p15153.shtml>
- Ketcham, R. A., Carter, A., Donelick, R. A., Barbarand, J., & Hurford, A. J. (2007). Improved modeling of fission-track annealing in apatite. *American Mineralogist*, 92(5–6), 799–810. <https://doi.org/10.2138/am.2007.2281>
- Klein, A. G., Seltzer, G. O., & Isacks, B. L. (1999). Modern and last local glacial maximum snowlines in the Central Andes of Peru, Bolivia, and Northern Chile. *Quaternary Science Reviews*, 18(1), 63–84. [https://doi.org/10.1016/S0277-3791\(98\)00095-X](https://doi.org/10.1016/S0277-3791(98)00095-X)
- Lloyd, S., Van Der Lee, S., França, G. S., Assumpção, M., & Feng, M. (2010). Moho map of South America from receiver functions and surface waves. *Journal of Geophysical Research: Solid Earth*, 115(11), 1–12. <https://doi.org/10.1029/2009JB006829>
- Ma, Y., & Clayton, R. W. (2014). The crust and uppermost mantle structure of Southern Peru from ambient noise and earthquake surface wave analysis. *Earth and Planetary Science Letters*, 395, 61–70. <https://doi.org/10.1016/j.epsl.2014.03.013>
- Mcglashan, N., Brown, L., & Kay, S. (2008). Crustal thickness in the central Andes from teleseismically recorded depth phase precursors. *Geophysical Journal International*, 175(3), 1013–1022. <https://doi.org/10.1111/j.1365-246X.2008.03897.x>
- Perello, J., Carlotto, V., Zarate, A., Ramos, P., Posso, H., Neyra, C., et al. (2003). Porphyry-Style Alteration and Mineralization of the Middle Eocene to Early Oligocene Andahuaylas-Yauri Belt, Cuzco Region, Peru. *Economic Geology*, 98, 1575–1605.
- Pérez-Gussinyé, M., Lowry, A. R., Phipps Morgan, J., & Tassara, A. (2008). Effective elastic thickness variations along the andean margin and their relationship to subduction geometry. *Geochemistry, Geophysics, Geosystems*, 9(2).

- <https://doi.org/10.1029/2007GC001786>
- Reiners, P. W., & Brandon, M. T. (2006). Using Thermochronology To Understand Orogenic Erosion. *Annual Review of Earth and Planetary Sciences*, 34(1), 419–466. <https://doi.org/10.1146/annurev.earth.34.031405.125202>
- Ruiz, G. M. H., Carlotto, V., Van Heiningen, P. V., & Andriessen, P. A. M. (2009). Steady-state exhumation pattern in the Central Andes – SE Peru. *Geological Society, London, Special Publications*, 324(1), 307–316. <https://doi.org/10.1144/SP324.20>
- Sambridge, M. (1999). Geophysical inversion with a neighbourhood algorithm –II. Appraising the ensemble. *Geophys. J. Int.*, 138, 727–746.
- Sambridge, Malcolm. (1999). Geophysical inversion with a neighbourhood algorithm - I. Searching a parameter space. *Geophysical Journal International*, 138(2), 479–494. <https://doi.org/10.1046/j.1365-246X.1999.00876.x>
- Springer, M. (1999). Interpretation of heat-flow density in the Central Andes. In *Tectonophysics* (Vol. 306, pp. 377–395). [https://doi.org/10.1016/S0040-1951\(99\)00067-0](https://doi.org/10.1016/S0040-1951(99)00067-0)
- Sundell, K. E., Saylor, J. E., Lapen, T. J., & Horton, B. K. (2019). Implications of variable late Cenozoic surface uplift across the Peruvian central Andes. *Scientific Reports*, 9(1), 1–12. <https://doi.org/10.1038/s41598-019-41257-3>
- Waples, D. W., & Waples, J. S. (2004). A review and evaluation of specific heat capacities of rocks, minerals, and subsurface fluids. Part 2: Fluids and porous rocks. *Natural Resources Research*. <https://doi.org/10.1023/B:NARR.0000032648.15016.49>
- Whittington, A. G., Hofmeister, A. M., & Nabelek, P. I. (2009). Temperature-dependent thermal diffusivity of the Earth’s crust and implications for magmatism. *Nature*, 458(7236), 319–321. <https://doi.org/10.1038/nature07818>